

Zonal flow driven by convection and convection driven by internal heating

David Goluskin

Submitted in partial fulfillment of the
requirements for the degree of
Doctor of Philosophy
in the Graduate School of Arts and Sciences

COLUMBIA UNIVERSITY

2013

© 2013

David Goluskin

All rights reserved

ABSTRACT

Zonal flow driven by convection and convection driven by internal heating

David Goluskin

In the first part, Rayleigh-Bénard convection is studied in a two-dimensional, horizontally periodic domain with free-slip top and bottom boundaries. This configuration encourages mean horizontal flows of zero horizontal wavenumber, which we study as an idealization of zonal flows in tokamaks, planetary atmospheres, and annular cylindrical convection experiments. These systems often satisfy free-slip conditions on at least one boundary and are approximately two-dimensional.

Stable steady states with zonal flow are found for Prandtl numbers up to 0.3. Stable and unstable steady states with horizontal periods up to six times the layer height are computed for a Prandtl number of 0.1 and Rayleigh numbers, Ra , up to $2 \cdot 10^5$. Concurrently stable states with and without zonal flow are found where the state without zonal flow convects heat over 10 times faster. Steady zonal flow arises subcritically whenever the horizontal period is not forced to be narrow, contrary to most prior predictions by truncated models. Steady states and their bifurcations are studied in a truncated model that does predict subcriticality.

Direct numerical simulations are performed with a horizontal period twice the layer height, Prandtl numbers between 1 and 10, and Ra between $5 \cdot 10^5$ and $2 \cdot 10^8$. Zonal flow arises subcritically as Ra is raised but is seen in all quasi-steady states at large Ra . The fraction of the total kinetic energy comprised by zonal flow approaches unity as Ra grows. At a Prandtl number of 1, vertical convective heat transport occurs in temporal bursts, nearly vanishing in between, and is non-monotonic in Ra . At Prandtl numbers of 3 and 10, convective transport at no time nearly vanishes, and time-averaged Nusselt numbers scale as $Ra^{0.077}$ and $Ra^{0.19}$, respectively. Both growth rates are below the range accepted for Rayleigh-Bénard convection without zonal flow.

In the second part, two-dimensional direct numerical simulations are conducted for convection sustained by uniform internal heating in a horizontal fluid layer. Top and bottom boundary temperatures are fixed and equal. Prandtl numbers range from 0.01 to 100. A control parameter, R , that is similar to the usual Rayleigh number is varied up to $5 \cdot 10^5$ times its critical value at the onset of convection. The asymmetry between upward and downward heat fluxes is non-monotonic in R . In a broad high- R regime, dimensionless mean temperature scales as $R^{-1/5}$. We discuss the scaling of mean temperature and heat-flux-asymmetry, which we find to be better diagnostic quantities than the conventionally used top and bottom Nusselt numbers.

Contents

Acknowledgements	vii
1 Convection basics	1
1.1 The Boussinesq approximation	2
1.2 Rayleigh-Bénard convection	5
1.2.1 Kinematic boundary conditions	6
1.2.2 Thermal boundary conditions	7
1.2.3 Qualitative features of RB convection	10
1.2.4 Heat transport	12
1.2.5 The Nusselt number	13
I Zonal flow driven by Rayleigh-Bénard convection	17
2 Background	18
2.1 Introduction	18
2.2 The shearing mechanism	22
2.3 Physical applications	25
2.3.1 RB convection in an annular cylinder	26
2.3.2 Tokamaks	26

3 Steady states	30
3.1 Introduction	30
3.2 Visualizations of steady states	31
3.3 Effect of the horizontal period	36
3.3.1 Choice of the computational domain	36
3.3.2 TC branches	37
3.3.3 A more complete bifurcation diagram	39
3.4 Effect of the Prandtl number	41
3.5 Nusselt numbers	42
3.6 Conclusions	43
4 Reduced models and their bifurcation structures	46
4.1 Introduction	46
4.2 Stream function formulation	47
4.3 The HK6 and HK8 models	49
4.3.1 Governing equations	49
4.3.2 Properties of the HK8 truncation	51
4.3.3 Steady states of the HK6 model	53
4.4 Steady solutions and bifurcations of the HK8 model	55
4.4.1 Steady rolls	56
4.4.2 TC states and pitchfork bifurcations	57
4.4.3 Hopf bifurcations and stability	61
4.4.4 Minimum Rayleigh numbers at which TC exists	63
4.5 Conclusions	65
5 Chaotic and turbulent flows	67
5.1 Introduction	67

5.2	Sustained zonal flow with $\sigma = 10$	69
5.2.1	Existence of states with and without zonal flow	69
5.2.2	Structures in shearing convection	71
5.2.3	Velocity and temperature profiles in shearing convection	74
5.2.4	Time series of integral quantities in shearing convection	76
5.3	Bursting and relaxation oscillations at moderate σ	80
5.3.1	The physics of an oscillation	80
5.3.2	Dependence of oscillations on the Rayleigh number	83
5.3.3	Dependence of oscillations on the Prandtl number	84
5.3.4	Velocity and temperature profiles	85
5.3.5	Reduced models of oscillating zonal flow	87
5.4	Nusselt numbers in convection with zonal flow	88
5.5	Conclusions	91
II	Convection driven by internal heating	94
6	Convection driven by internal heating	95
6.1	Introduction	95
6.2	Governing equations	98
6.2.1	Boundary conditions	99
6.2.2	Conductive solution	100
6.3	Qualitative results	100
6.3.1	Steady rolls	101
6.3.2	Near-periodicity in time	101
6.3.3	Toward turbulence	103
6.3.4	Low Prandtl numbers	106

6.4	Integral quantities	106
6.4.1	Vertical heat fluxes	108
6.4.2	Mean temperature	110
6.4.3	Power integrals	111
6.4.4	Dimensionless numbers	111
6.5	Quantitative results	113
6.5.1	Temperature profiles	113
6.5.2	Convective heat flux	114
6.5.3	Temperature	117
6.5.4	Scaling arguments	119
6.6	Conclusions	123
References		126
A Appendix to Chapter 3		135
A.1	Numerical methods	135
A.2	L_1 and TC states with fixed-flux thermal boundary conditions	138
B Appendix to Chapter 4		141
B.1	Other truncated models	141
B.2	Linear stability matrices of HK8	143
B.3	Degenerate L_2 branch of HK6	145
B.4	Hopf bifurcations	146
B.4.1	HK8	146
B.4.2	HK6	149
B.5	Complete classification of local bifurcations of steady states	152
B.6	Limiting cases	158

B.6.1	Short wavelengths ($k \gg 1$)	158
B.6.2	Small Prandtl numbers ($\sigma \ll 1$)	162
B.6.3	Small- σ limit of the narrow-HK6 model	163
C	Appendix to Chapter 5: Computational methods	164
D	Appendix to Chapter 6	166
D.1	Integral bounds	166
D.1.1	Proof that $T > 0$ on the interior	166
D.1.2	Proof that $0 < \langle T \rangle \leq 1/12$	167
D.1.3	Proof that $0 \leq \langle wT \rangle \leq 1/2$	167
D.2	Computational methods	168

Acknowledgements

I am indebted, foremost, to my advisors, Ed Spiegel and David Keyes. In the years since he brought me to Columbia, David Keyes has given me much advice and autonomy, and I am grateful for both. Ed Spiegel has provided a great amount of guidance over the many hundreds of hours of his retirement on which I have encroached, and I aspire to the patience and high personal standards that he applied to our work together. He is, furthermore, a pleasure to collaborate with and an all-around mensch.

I am would like to also thank the remaining members of my thesis committee — Michael Weinstein, Michael Mauel, and Michael Shelley — for the time they took and the helpful feedback they gave me.

This thesis would have been impossible without the many emails I exchanged with Paul Fischer and Aleksandr Obabko, who instructed me in using their excellent fluid dynamics code, nek5000.

The work in this thesis has benefited from numerous helpful discussions. The people with whom I have discussed internally heated convection include Michael Weinstein, Charles Doering, Jared Whitehead, Francis Kulacki, and Antonello Provenzale. The people with whom I have discussed zonal flow driven by convection include Glenn Flierl, Hans Johnston, Charles Doering, Da Zhu, Jared Whitehead, Keith Julien, Edgar Knobloch, and Michael Mauel.

My fellowship in the Geophysical Fluid Dynamics program at the Woods Hole Oceanographic Institute in the summer of 2010 has undoubtedly contributed to my academic development during my PhD, both through the academic relationships I formed there and the discussions I have had there on subsequent visits. I benefited also from visiting the group of Annick Pouquet at NCAR in the summer of 2008; they patiently gave me my first exposure

to mathematical research. Most of the work in this thesis was supported financially by an NSF RTG fellowship.

More broadly, my thanks go to all the good teachers and professors I have had over the last twenty years, and to the friends who have provided encouragement and welcome diversions over the last six. Tricia Rubi, in particular, has been a major source of support and a minor source of proofreading.

Lastly, I would like to thank my parents for a lifetime of unconditional support, academic and otherwise.

Chapter 1

Convection basics

“Convection” refers herein to fluid motion driven by differential body forces. In many applications, these differential forces are created by variations in the fluid’s density in the presence of a gravitational potential. In the standard instance of thermal convection, temperature variations are responsible for creating the density variations. Nonuniform temperature alone does not guarantee thermal convection, however. Rather, hot (less dense) fluid must lie below cold (more dense) fluid, and the destabilizing effects of this adverse temperature gradient must overcome the viscous forces that damp fluid motion. We typically speak in terms of thermal convection in this thesis, but it should be kept in mind that other convective systems are governed by similar dynamics. In salt water, for instance, salinity can take the place of temperature. In electroconvection, electric charge takes the place of temperature, and the electric potential takes the place of the gravitational potential.

Throughout this thesis we focus on convection that is sustained, rather than transient. An inexhaustible source of energy is needed to sustain convection against viscous dissipation. If a parcel of hot fluid lies below a parcel of cold fluid, say, convective motion and thermal diffusion tend to equilibrate the temperature field. For thermal convection to be sustained, the fluid must be driven away from equilibrium by endlessly adding heat somewhere other

than the top of the domain or removing heat somewhere other than the bottom of the domain. This can be accomplished through the thermal boundary conditions, as when a pot of water is boiled on the stove, or it can be accomplished through internal heat sources or sinks, as when radioactive decay heats the Earth's mantle. The fluid motion that scalar fields induce affects, in turn, the transport of the scalars themselves. Fluid motion and scalar transport, inextricably entwined, are the twin foci of the study of convection.

The first section of this Chapter introduces the Boussinesq equations. The second section summarizes standard features of Rayleigh-Bénard convection and offers an argument on how best to define the Nusselt number. The particular convection problems studied in Parts I and II of this thesis are introduced in the opening sections of Chapters 2 and 6, respectively.

1.1 The Boussinesq approximation

Supposing that a fluid is described by the compressible Navier-Stokes equations, that its density is a known function of its temperature and pressure, and that it is subject to gravitational acceleration \mathbf{g} , then its motion will be governed by the equations

$$\partial_t \rho + \nabla \cdot (\rho \mathbf{u}) = 0 \quad (1.1)$$

$$\rho(\partial_t \mathbf{u} + \mathbf{u} \cdot \nabla \mathbf{u}) = -\nabla p + \rho \nu \nabla^2 \mathbf{u} + \rho \mathbf{g} \quad (1.2)$$

$$\partial_t T + \mathbf{u} \cdot \nabla T = \kappa \nabla^2 T + Q, \quad (1.3)$$

where $\mathbf{u} = (u, v, w)$ is the fluid's velocity, T its temperature, p its pressure, ρ its density, ν its dynamic viscosity, κ its thermal diffusivity, and the term Q contains any heat sources or sinks. Equations (1.1)-(1.3) describe convection accurately in a vast array of applications but can be overkill when the density does not deviate too strongly from its distribution in hydrostatic equilibrium. In pressure-driven fluid flows where the density varies weakly (that

is, where the Mach number is small), the density of the fluid may simply be taken as constant, and the compressible Navier-Stokes equations may be replaced by their incompressible counterparts. In buoyancy-driven flows, however, the situation is slightly more complicated. Density variations cannot be totally ignored because they create the buoyancy gradients needed to drive the flow. On the other hand, the full compressibility of the Navier-Stokes equations creates analytical and numerical difficulties that one would like to avoid. The solution is to use the Boussinesq approximation (sometimes called the Oberbeck-Boussinesq approximation).

The Boussinesq approximation involves two main assumptions. First, the fluid's density is assumed to be independent of pressure and to vary linearly with temperature about some hydrostatic reference state that we denote by ρ_* and T_* . That is,

$$\rho(T) = \rho_* [1 - \alpha(T - T_*)], \quad (1.4)$$

where α is the linear coefficient of thermal expansion. Second, the density variations are assumed to be sufficiently weak that they can be ignored in the enforcement of mass conservation, entering the equations of motion only through buoyancy forces. The velocity field is therefore solenoidal, and the fluid is typically called incompressible, though, physically speaking, the variations in buoyancy are indeed created by compression of the fluid. The Boussinesq approximation is expected to be accurate when “(a) the vertical dimension of the fluid is much less than any scale height, and (b) the motion-induced fluctuations in density and pressure do not exceed, in order of magnitude, the total static variations of these quantities” ([Spiegel and Veronis, 1960](#)). With constant molecular parameters, constant gravitational acceleration g acting in the $-\hat{\mathbf{z}}$ direction, and *without heat sources*, the Boussinesq

approximation yields the canonical *Boussinesq equations* (Spiegel and Veronis, 1960),

$$\nabla \cdot \mathbf{u} = 0 \quad (1.5)$$

$$\partial_t \mathbf{u} + \mathbf{u} \cdot \nabla \mathbf{u} = -\frac{1}{\rho_*} \nabla p + \nu \nabla^2 \mathbf{u} + g \alpha T \hat{\mathbf{z}} \quad (1.6)$$

$$\partial_t T + \mathbf{u} \cdot \nabla T = \kappa \nabla^2 T, \quad (1.7)$$

where the pressure has been redefined to absorb the constant terms of the buoyancy force.

To nondimensionalize the Boussinesq equations, the problem at hand must be fully defined, including the spatial domain and the boundary conditions. The domain can then be used to define a length scale, d , and the boundary conditions can be used to define a temperature scale, Δ . (If internal heat sources or sinks exist, these can also be used to define Δ , as done in Part II.) Time is most often nondimensionalized by the characteristic diffusive time, d^2/κ , in which case pressure is nondimensionalized by $\rho_* d^2/\kappa$. The resulting *dimensionless* Boussinesq equations are

$$\nabla \cdot \mathbf{u} = 0 \quad (1.8)$$

$$\partial_t \mathbf{u} + \mathbf{u} \cdot \nabla \mathbf{u} = -\nabla p + \sigma \nabla^2 \mathbf{u} + \sigma R T \hat{\mathbf{z}} \quad (1.9)$$

$$\partial_t T + \mathbf{u} \cdot \nabla T = \nabla^2 T. \quad (1.10)$$

The independent variables — x , y , z , and t — and the dependent variables — \mathbf{u} , T , and p — are henceforth dimensionless unless otherwise noted. The dimensionless parameters in equations (1.8)-(1.10) are the Rayleigh number, R , and Prandtl number, σ , defined by

$$R = \frac{g \alpha d^3 \Delta}{\kappa \nu} \quad (1.11)$$

$$\sigma = \frac{\nu}{\kappa}. \quad (1.12)$$

The Rayleigh number may be thought of as the ratio of inertial forces to viscous forces. When it is large, the fluid is driven strongly. We regard R as the primary control parameter since raising it typically makes the flow more complex. For R to indeed be a control parameter, the temperature scale, Δ , must be based on quantities that are known *a priori*, such as the boundary conditions. However, it is sometimes useful to define another Rayleigh number using a temperature scale that is determined dynamically by the flow. This sort of Rayleigh number cannot serve as a control parameter, but it can be a useful diagnostic quantity. In Part II, for instance, we employ both a *control* Rayleigh number, R , for which Δ is defined in terms of the rate of internal heating, and a *diagnostic* Rayleigh number, Ra , for which Δ is the dynamically determined mean temperature of the fluid.

The Prandtl number is the rate at which the fluid dissipates momentum, divided by the rate at which it dissipates heat. Unlike the Rayleigh number, it is a molecular property of the fluid and does not depend on the geometry or boundary conditions. The Prandtl number is large in fluids that damp motion strongly and conduct heat poorly. In the Earth's mantle, for instance, σ is effectively infinite. The Prandtl number is small in fluids that damp motion weakly and conduct heat well; examples include liquid metals and stellar plasmas.

1.2 Rayleigh-Bénard convection

Rayleigh-Bénard convection (henceforth RB convection) is the best-studied convection scenario, having become a favored model for investigating instabilities, bifurcations, pattern formation, and thermal turbulence (Getling, 1998; Siggia, 1994). The distinguishing feature of RB convection is that it occurs in a horizontally planar layer of fluid, though this layer may be two- or three-dimensional and may be of finite or infinite horizontal extent. Heat flows upward through the layer, transported both by conduction and by the convective flow that the thermal gradients drive. In this thesis, we further define RB convection as being gov-

erned by the Boussinesq equations (1.8)-(1.10). Some authors reserve the designation of RB convection for flows driven by keeping the bottom boundary fixed at a higher temperature than the top boundary, but we shall apply it regardless of the particular thermal boundary conditions driving the flow. The flows we study in Part I fall under our definition of RB convection, while the flows we study in Part II do not because they are heated internally.

To fully define a configuration of RB convection, one must specify the precise 2D or 3D planar geometry, as well as the various boundary conditions. The vertical thickness of the fluid layer typically defines the length scale, d , so the top and bottom boundaries lie (dimensionlessly) at $z = \pm 1/2$. At the very least, boundary conditions on \mathbf{u} and T are needed at the top and bottom boundaries. If the domain is periodic or infinite in the horizontal — in the one or two directions normal to gravity — then no further conditions are needed. If the domain has solid side walls, however, boundary conditions must be specified there as well.

1.2.1 Kinematic boundary conditions

Two simple boundary conditions on the velocity are common: *no-slip* and *free-slip*. At no-slip (a.k.a. rigid) boundaries, the fluid cannot move relative to the boundaries:

$$\mathbf{u} = 0. \quad (1.13)$$

If a box encloses a fluid on all sides, for instance, as is often the case in laboratory experiments, then all six boundaries would be modeled as no-slip according to (1.13). At free-slip (a.k.a. stress-free) boundaries, the fluid flows parallel to the boundary, and the boundary exerts no shear stress on the fluid:

$$\mathbf{u} \cdot \mathbf{n} = \mathbf{n} \cdot \nabla \mathbf{u} = 0, \quad (1.14)$$

where the vector \mathbf{n} is normal to the boundary. Free-slip conditions often apply when the fluid is not in contact with a solid wall, as occurs, say, on the surface of coffee cooling in a mug, or at the edge of a magnetically confined plasma.

Rayleigh's seminal stability analysis of the Boussinesq equations employed free-slip top and bottom boundaries for mathematical convenience ([Rayleigh, 1916](#)). Many subsequent authors have done the same, often for this same convenience in analytic studies, but a larger number of authors have instead imposed no-slip boundaries, particularly when solving the PDE numerically. No-slip boundaries let computations be compared to laboratory experiments in which the convecting fluids are enclosed in rigid vessels.

In this thesis, our top and bottom boundaries will be free-slip in Part I and no-slip in Part II. In Part I, we study the ability of convection to drive mean horizontal flow in the fluid. We choose free-slip boundaries because they can exert no horizontal shear forces on the fluid, thus allowing stronger horizontal flows to develop. In Part I, where we study convection driven by internal heating, we employ no-slip boundaries to make contact with laboratory experiments.

1.2.2 Thermal boundary conditions

There are many possible choices for the thermal boundary conditions, but for any such choice the bottom boundary must be kept hotter than the top one, on average, both in the static state and after the onset of convection. This is necessary to sustain upward heat transfer, which is in turn necessary to sustain the convection against viscous dissipation since the upward convective transport is proportional to the work that buoyancy forces perform on the fluid. For any such boundary conditions, the mean temperature decrease from the bottom boundary to the top one in the *static* state is easy to compute — at most, the Laplace equation must be solved. Typically, this static temperature difference is taken as the

temperature scale, Δ , that is used in defining R and nondimensionalizing the temperature. The dimensionless temperature difference between the boundaries will thus be unity in the static state and may or may not decrease as convection sets in, depending on the thermal boundary conditions.

Studies of RB convection most often impose *fixed-temperature* boundary conditions, where the bottom boundary is fixed at a higher temperature than the top one. Only in this case does the temperature difference between the boundaries remain unity after the onset of convection. While this temperature difference is dynamically significant, the absolute values of the temperature are not because the Boussinesq equations are invariant under translation in T . One convenient choice of boundary temperatures is $T_T = -1/2$ and $T_B = 1/2$, where the subscripts denote the top and bottom boundaries, respectively. As R is increased with fixed boundary temperatures, convection tends to strengthen, carrying ever more heat upward through the layer. We will, however, explore possible exceptions to this tendency in Part I.

It is equally simple, though a bit less common, to drive RB convection by imposing *fixed-flux* thermal boundary conditions. In this case, a dimensionful temperature gradient, Γ , can be specified at one or both of the top and bottom boundaries. (If both boundaries have fixed fluxes, the fluxes must be equal for quasi-steady convection to be possible.) Although the mean heat transport through the layer will be fixed, the fraction of this transport that is accomplished by convection, as opposed to conduction, can increase as the flow strengthens. The dimensionful temperature difference between the boundaries will be $d\Gamma$ in the static state, so this is the temperature scale used in defining R and nondimensionalizing temperature. The resulting dimensionless boundary conditions are $\partial_z T_T = \partial_z T_B = -1$. Fixed-flux RB convection differs significantly from fixed-temperature RB convection at the small Rayleigh numbers near the onset of motion ([Sparrow et al., 1963](#); [Hurle et al., 1967](#);

Chapman and Proctor, 1980), but the two cases become very similar as the flow becomes turbulent (Johnston and Doering, 2009).

Fixed-temperature and fixed-flux boundary conditions, and any combination thereof, are the simplest possible conditions in that they provide the temperature scale needed to nondimensionalize the problem and define the Rayleigh number, but they introduce no additional parameters. One obtains a sizable class of model problems simply by applying free-slip or no-slip kinematic conditions and fixed-temperature or fixed-flux thermal conditions in various combinations on the various boundaries. More complicated thermal boundary conditions are less attractive for defining model problems since they typically increase analytical difficulty and introduce additional parameters, but they can be more physically realistic. For instance, imperfectly insulating boundaries can be approximated by Robin boundary conditions, as in $\partial T / \partial \mathbf{n} = -a(T - T_\infty)$ (Sparrow et al., 1963), while black body radiation might be modeled by the nonlinear law $\partial T / \partial \mathbf{n} = -a(T - T_\infty)^4$, where a and T_∞ are constants. Each of these conditions contains two dimensionful constants, only one of which can be removed by nondimensionalization, so each would introduce an additional parameter beyond R and σ . Each new parameter makes it much harder to understand the entirety of parameter space, which is why fixed-temperature and fixed-flux conditions are appealing for constructing model problems. When the fluid also contains internal heat sources or sinks, which are omitted from (1.8)-(1.10), these too can be used to define the temperature scale, Δ . This is precisely what we will do in Part II when we study convection driven by internal heating.

In order to compare RB flows with different thermal boundary conditions, it is useful to define a diagnostic Rayleigh number, Ra . Whereas the control parameter R is defined using the temperature difference between the boundaries in the *static* state, which is normalized to one, the diagnostic Ra is defined using the temperature difference in the *developed* flow. That is,

$$Ra = \delta \bar{T} R, \quad (1.15)$$

where $\delta\bar{T}$ is the dimensionless mean temperature difference between the boundaries (cf. section 1.2.4). Relation (1.15) applies only to RB convection; we will use a similar but not identical relation when we study internally heated convection in Part II. The quantities R and Ra are equal for fixed-temperature boundary conditions, which is why the distinction is not always made, but the difference is crucial for any other boundary conditions — R is used to define the PDE, while Ra is used to compare flows with different thermal boundary conditions.

1.2.3 Qualitative features of RB convection

Several basic features of RB convection are shared by the various geometries and boundary conditions one might choose. At the smallest Rayleigh numbers, the only steady (or quasi-steady) solution to the Boussinesq equations is the static, purely conductive state, in which the vertical temperature profile is linear. As R is raised, a series of steady convective solution branches bifurcate from the static state. While the static state shares the full symmetry group of the PDE, the steady convective states that bifurcate from it must break some of these symmetries, and the particular symmetries that may be broken are constrained by the theorems of equivariant bifurcation theory (Golubitsky and Stewart, 2000). The simplest solution branches consist of steady, counter-rotating, two-dimensional rolls. The left-hand image in Figure 1.1 depicts such a roll solution, computed with no-slip, fixed-temperature conditions on both boundaries.

As R is increased further, there come into existence many other branches of solutions that share some, but not all, of the PDE's symmetries. Such solutions include, for instance, steady states, traveling waves, and periodic solutions. These new branches of invariant solutions can bifurcate from other branches or arise in saddle-node bifurcations. The details of the bifurcation structure depend strongly on the geometry, boundary conditions, and Prandtl

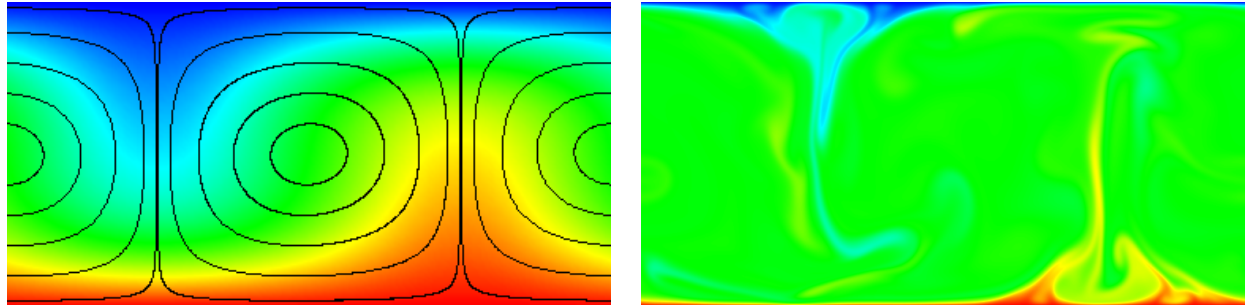


Figure 1.1: Two-dimensional RB convection in a domain with periodic sides and a width twice its height. The top and bottom boundaries are fixed-temperature and no-slip, and $\sigma = 1$. The temperature scale goes from $T = -1/2$ (blue) to $T = 1/2$ (red). The left-hand image depicts streamlines and the temperature field of a steady state at $R = 3000$. The right-hand image depicts an instantaneous temperature field from a chaotic flow at $R = 10^8$. Fluid in the middle of each image rotates counter-clockwise, while that toward the edges rotates clockwise.

number, but the number of invariant solutions reliably increases as R grows, eventually becoming infinite. Still, these solution branches are typically unstable in much, if not all, of parameter space. At intermediate R , it is common for a few invariant solutions to be stable simultaneously. When R grows large, however, each invariant solution eventually becomes unstable, after which only spatiotemporal chaos is physically realizable. Such chaotic flows are often called turbulent once they become sufficiently strong and complex, though there is no precise and universal definition for the onset of turbulence. The right-hand image of Figure 1.1 depicts the instantaneous temperature field of a chaotic 2D flow, computed under the same conditions as the left-hand image, except that R is much larger. Being constrained to 2D, the flow remains roll-like at large Rayleigh numbers, but this would not be so in 3D.

When the top and bottom boundary conditions are of the same type, as they often are, the governing equations are invariant under the negation of z and T . As a result, RB convection looks essentially the same when viewed upside down, except that the rising fluid is cold and the falling fluid is hot. This fact is particularly clear for steady state of Figure 1.1, which is itself invariant under the negation of z and T , up to translation in the periodic

direction. This symmetry has been broken in the turbulent state of Figure 1.1 and does not hold instantaneously, but it will still hold in a time-averaged sense. That is, the top and bottom boundary layers will typically have the same mean profiles and contribute equally to driving the flow by sending thermal plumes into the interior. This will not remain true when the up-down symmetry of the governing equations is lost, either through additional terms in the PDE or through differences between the top and bottom boundary conditions. In such cases, one of the two boundary layers will typically be more responsible (or solely responsible) for driving the flow. In the internally heated configuration that we study in Part II, for instance, the convection is driven entirely by the unstable top boundary layer.

1.2.4 Heat transport

Several integral quantities are useful in understanding how RB convection transports heat with various thermal boundary conditions. The integral quantities on which we focus in this thesis will be averaged over either horizontal surfaces or the entire volume, and they may or may not be averaged over time as well. We will denote average over a horizontal surface and infinite time by an overbar, as in \bar{f} , and averages over the entire volume and infinite time by angle brackets, as in $\langle f \rangle$. In a 2D planar domain with horizontal extent $0 \leq x \leq A$ and vertical extent $-1/2 \leq z \leq 1/2$,

$$\bar{f}(z) := \lim_{\tau \rightarrow \infty} \frac{1}{\tau} \int_0^\tau dt \frac{1}{A} \int_0^A dx f(x, z, t) \quad (1.16)$$

$$\langle f \rangle := \int_{-1/2}^{1/2} \bar{f}(z) dz. \quad (1.17)$$

We shall also have cause to look at the instantaneous analogs of (1.16) and (1.17), which we will denote as $\bar{f}^t(z, t)$ and $\langle f \rangle^t(t)$, respectively.

Writing the temperature equation (1.10) in the standard form of a conservation law, $\partial_t T + \nabla \cdot (\mathbf{u}T - \nabla T) = 0$, one sees that the (dimensionless) heat current at a point is composed of a conductive part, $-\nabla T$, and a convective part, $\mathbf{u}T$. The mean flux across a surface is simply the average of the normal current over that surface, so in the plane layer of RB convection, the time-averaged conductive flux across a horizontal surface is $-\partial_z \bar{T}(z)$, while the time-averaged convective flux is $\bar{wT}(z)$. Integrating these expressions over all constant- z surfaces yields the volume-averaged conductive and convective vertical heat fluxes: $\delta\bar{T}$ and $\langle wT \rangle$, respectively, where $\delta\bar{T} := \bar{T}_B - \bar{T}_T$ is the mean dimensionless temperature difference between the boundaries.

1.2.5 The Nusselt number

In the study of chaotic and turbulent fluid flows, much effort is devoted to understanding and predicting the dependence of integral quantities on the control parameters. This is partly because certain integral quantities are physically important and partly because few other tools exist for analyzing highly complicated flows. Out of the quantities one might examine in a convective flow, the most ink has been spilled over Nusselt numbers, dimensionless numbers that convey the relative amounts of heat transport achieved by convection and by conduction. The effect of fluid motion on scalar transport is, after all, one of the chief motives for studying scalar-driven flows in the first place. To define a Nusselt number, one must choose a surface or volume across which the heat flux is to be quantified. In RB convection, the most attention is paid to the *vertical* heat flux, either across a particular horizontal surface or averaged over the entire layer. This vertical component of the convective transport, unlike the horizontal components, must be nonzero in any sustained RB flow since it is solely through this component that buoyancy forces drive the fluid.

Having chosen a surface or volume across which the heat flux is to be studied, the Nusselt number of a flow is typically defined as the total heat transport, divided by the conductive heat transport. There is some ambiguity, however, over whether one divides by the conductive transport in the flowing fluid or in the static state. Defined in the former way, the Nusselt number conveys the (inverse) fraction of heat transport in a flow that is being accomplished by conduction. Defined in the latter way, it conveys the amplification of heat transport by the flow, relative to the static state. The two definitions agree in RB convection only when the top and bottom boundary temperatures are fixed since only then is the mean conductive flux unchanged by the onset of motion. Fixed-temperature boundaries dominate the literature, however, which is why many authors do not draw a distinction between the two ways of defining a Nusselt number (and likewise with the distinction between the control and diagnostic Rayleigh numbers, R and Ra). When the two definitions do not agree, we will define the Nusselt number in the former way: the total heat transport, divided by the conductive transport, both in the *flowing* fluid. In RB convection, the volume-averaged version of this definition is

$$N := \frac{\delta\bar{T} + \langle wT \rangle}{\delta\bar{T}}. \quad (1.18)$$

Our definition of N has been used in the past (e.g., by [Otero et al., 2002](#); [Johnston and Doering, 2009](#); [Wittenberg, 2010](#)), but it is perhaps less common than the other definition, in which the total heat flux is normalized by the heat flux in the *static* state, as in

$$\frac{\delta\bar{T} + \langle wT \rangle}{\delta\bar{T}_{static}}. \quad (1.19)$$

In the RB nondimensionalization we have described, $\delta\bar{T}_{static} = 1$ for all thermal boundary conditions. For *fixed-temperature* boundaries only, $\delta\bar{T} = 1$ in the flowing fluid also, so

expressions (1.18) and (1.19) both reduce to

$$N = 1 + \langle wT \rangle, \quad (1.20)$$

a quantity that is unity in the static state and grows as fluid motion sets in. To see why definition (1.18) is more useful than (1.19) as a generalization of (1.20), let us consider RB convection with *fixed-flux* thermal boundary conditions. In such flows, the dimensionless net heat flux is fixed at unity ($\delta\bar{T} + \langle wT \rangle \equiv 1$), but the relative contributions of conduction and convection ($\delta\bar{T}$ and $\langle wT \rangle$) can vary. A Nusselt number defined by (1.19) would remain equal to unity no matter how strong the flow becomes — not a useful diagnostic quantity. The Nusselt number we have defined in (1.18), on the other hand, reduces for fixed-flux boundaries to

$$N = \frac{1}{\delta\bar{T}} = \frac{1}{1 - \langle wT \rangle}. \quad (1.21)$$

This quantity behaves qualitatively like its fixed-temperature counterpart, being unity in the static state and growing as fluid motion sets in, and the same is true of N for any other boundary conditions that sustain RB convection.

Defining N as we do also reveals *quantitative* similarities between seemingly disparate convective flows, namely in the dependence of N on Ra , the diagnostic Rayleigh number defined by (1.15). Analytical bounds of the form $N < cRa^{1/2}$ have been proven for RB flows with a variety of thermal boundary conditions (Howard, 1972; Constantin and Doering, 1996; Otero et al., 2002; Wittenberg, 2010). Moreover, simulations of fixed-temperature and fixed-flux 2D RB convection under otherwise identical conditions have displayed scalings very close to $N \sim cRa^{2/7}$ for both sets of boundary conditions (Johnston and Doering, 2009). These similarities become apparent only when one defines N by (1.18) and Ra by (1.15), and they

are not limited to RB convection. By adapting our definitions of N and Ra to internally heated convection in Part II, we will find parallels to the more usual boundary-driven flows.

Part I

Zonal flow driven by Rayleigh-Bénard convection

Chapter 2

Background

2.1 Introduction

In Rayleigh-Bénard (RB) convection, buoyancy forces directly drive fluid motion in only the vertical direction, but the fluid must also move horizontally since the confining geometry forces it to recirculate. The governing equations give no preferential direction to this horizontal motion, yet large-scale mean horizontal flows may nonetheless arise. The strongest mean flows observed are uniform in the direction of motion, which is possible only in geometries that admit mean flows of wavenumber zero. Examples include azimuthal flow in an annulus or horizontal flow in a periodic cartesian domain. We will refer to both as *zonal flow*, the name given to the zero-wavenumber flows in planetary atmospheres and toroidal plasmas.

Zonal flow in an annular cylinder was seen in the convection experiments of [Krishnamurti and Howard \(1981\)](#). The vertically oriented cylinder was heated on its bottom and cooled on its top. At large Rayleigh numbers, thermal plumes emanating from the top and bottom boundaries drifted around the annulus in opposite directions, revealing a vertically sheared mean azimuthal flow. The relationship between this zonal flow and other large-scale mean

flows seen in RB convection is somewhat unclear. Krishnamurti and Howard (1981) report similar mean flows in a wide, square domain, again with plumes drifting in opposite directions along opposite boundaries, but this finding has not been reproduced, despite numerical efforts Hartlep et al. (2003, 2005). In narrower domains whose widths are comparable to the layer thickness, large-scale circulations, or “winds”, have been identified in many physical and numerical experiments, as surveyed by Ahlers et al. (2009). These winds are fairly weak, however, and their direction may drift or reverse, unlike the flows seen by Krishnamurti and Howard (1981). Whether or not such flows are fundamentally different from zonal flows, we aim to study the latter, which are distinguished by their greater strength and their ability to significantly suppress heat transport.

While strong mean flows are apparently rare for RB convection in horizontally isotropic 3D domains, having been reported only once, they are quite common in convective systems where anisotropy gives the mean flow a preferred orientation. One prominent example is a toroidal plasma confined in a tokamak (Wesson, 2011), where radial “interchange” motions occur because densities are unstably stratified relative to the centrifugal force. In the magnetohydrodynamic approximation, these motions are analogous to RB convection, though they are made more complicated by magnetic effects and toroidicity (Garcia et al., 2006a). Just as convection in an annulus can drive horizontal zonal flow that is vertically sheared, interchange motions in a plasma can drive poloidal zonal flow that is radially sheared. This analogy is described further in section 2.3.2.

Convection is also responsible for driving latitudinal zonal flow in planetary atmospheres (Busse, 1994; Heimpel and Aurnou, 2007), and the analogy with zonal flow in tokamaks has been discussed in the plasma physics literature (Diamond et al., 2005; Wagner, 2007). However, rotation is fundamentally important in such cases and can even create zonal jets without convective forces (Cho and Polvani, 1996). For instance, rotation gives the zonal flow a preferred direction, whereas the azimuthal flow in the annular cylinder of Krishnamurti

and Howard (1981) can be either positively or negatively sheared in the vertical direction, and the choice breaks a symmetry of the system. We restrict ourselves here to non-rotating convection.

The main reason zonal flows are common in tokamaks and planetary atmospheres, but not in horizontally isotropic RB convection, is that additional effects in the former applications render the flow approximately two-dimensional. In a rotating atmosphere, the Taylor-Proudman effect suppresses variations parallel to the axis of rotation; in a tokamak, the plasma equilibrates very quickly along magnetic field lines, which wind primarily in the toroidal direction. Fully 3D convection is less conducive to the development of strong mean flow because, if such a flow does develop, it will partially suppress the motions that sustain it but not the transverse motions that can destroy it, as illustrated by the truncated model of Matthews et al. (1996). Rather than adding anisotropy that is specific to one application or another, our approach is to simply impose two-dimensionality. By studying zonal flow in 2D RB convection, we can contrast our findings with the abundant literature on RB convection that lacks zonal flow. The relative simplicity of this system also makes it easier to explore how various control parameters affect physically important quantities like the convective transport or the relative strength of the zonal flow.

The particular configuration we study throughout this Part is 2D RB convection in a horizontally *periodic* cartesian domain with *free-slip* top and bottom boundaries. This configuration is especially conducive to the formation of strong mean horizontal velocities; the lack of side walls lets the fluid flow unimpeded in the horizontal direction, the free-slip top and bottom boundaries contribute no stresses to slow the zonal flow, and the two-dimensionality prevents the mean flow from being destroyed by fluctuations in the transverse horizontal direction. The development of zonal flow is not sensitive to the thermal boundary conditions used to drive the flow, so we employ the popular *fixed-temperature* top and bottom boundaries to facilitate comparison with other studies. The mean horizontal flows that develop will

always be vertically sheared, a consequence of the conservation of horizontal momentum. We thus often refer to convection with a zonal flow as an instance of “convection-driven shear” or say that such a flow is “shearing”, as opposed to non-shearing.

The use of horizontally periodic 2D domains to model the onset of zonal flows in convection seems to begin with the numerical study of [Thompson \(1970\)](#), though some conceptually similar works are discussed therein. Our same geometry and boundary conditions were first adopted by [Howard and Krishnamurti \(1986\)](#), who derived and studied a reduced ODE model. Many similar ODE models followed, as discussed in Chapter 4, but very few studies of zonal flows in our chosen configuration have employed the full Boussinesq equations. Exceptions include the bifurcation analysis of [Rucklidge and Matthews \(1996\)](#) and the simulations of [Garcia and Bian \(2003\)](#), though both studies are limited to narrow horizontal periods. For the chaotic and turbulent convection-driven shear that occurs at large Rayleigh numbers, the Ra - σ parameter plane has scarcely been explored, despite the fact that plasma physical and astrophysical applications fall in these regimes.

We study zonal flows in our chosen configuration along several fronts. We first examine steady flows with zonal components and the bifurcations through which they arise. This is done in the context of a reduced model in Chapter 4 and then for the full PDE (the Boussinesq equations) in Chapter 3. The reduced model we study is more successful than previously studied models at capturing the aspects of the PDE’s bifurcation structure responsible for the onset of zonal flow. Indeed, our classification of the model’s bifurcations proves useful in guiding our subsequent study of the PDE, for which a comprehensive exploration of parameter space is beyond reach. The reduced model cannot, however, predict stabilities and integral quantities accurately in the strongly nonlinear regime, so solution of the full PDE is necessary. In Chapter 5, we turn to convection-driven shear at large Rayleigh numbers, integrating the 2D Boussinesq equations by direct numerical simulation. The zonal flows that develop are dominant, resembling those seen in strongly driven RB ([Krishnamurti and](#)

Howard, 1981) and plasma (Diamond et al., 2005) experiments. We obtain systematic data on $N(Ra, \sigma)$ in shearing RB convection, and, by comparing these data to past findings on non-shearing RB convection, we are able to quantify the dramatic suppression of heat transport by zonal flow.

For concreteness, let us look ahead and visualize two solutions of the Boussinesq equations in which convection drives zonal flow. Figure 2.1 depicts a typical temperature field from one of the high- Ra shearing flows we study in Chapter 5. Symmetry has broken such that the zonal flow carries plumes rightward along the bottom boundary and leftward along the top one. Such flow resembles the experiments of Krishnamurti and Howard (1981) but is uninterrupted by side walls. By contrast, the roll-like motion of Figure 2.2 is typical of 2D RB convection without zonal flow. Figure 2.2 depicts one of the *steady* shearing flows we study in Chapter 3, as well as a more typical steady state without zonal flow.¹ Like the chaotic shearing flow of Figure 2.1, the shearing flow of Figure 2.2 carries hot fluid rightward along the bottom boundary and cold fluid leftward along the top one, sustained by a single counterclockwise convection roll. In Chapters 4 and 3, we will examine the bifurcations through which steady states *without* zonal flow (like the bottom image in Figure 2.2) can lose stability to steady states *with* zonal flow (like the top image).

2.2 The shearing mechanism

Zonal flow does not contribute to vertical heat transport and cannot be driven directly by buoyancy. Rather, the intermediate horizontal scales that are driven by buoyancy interact with the zonal flow via the nonlinear term in the momentum equation. This interaction usually transfers energy upscale, into the sheared zonal flow, so we call it the *shearing*

¹Throughout this thesis, the red-blue color scheme of Figure 2.1 represents temperature in flows computed by time integration with `nek5000` (Fisher et al., 2013), as described in Chapter 5, and the purple-blue color scheme of Figure 2.2 represents temperature in steady flows computed with our own steady solver, as described in Chapter 3.

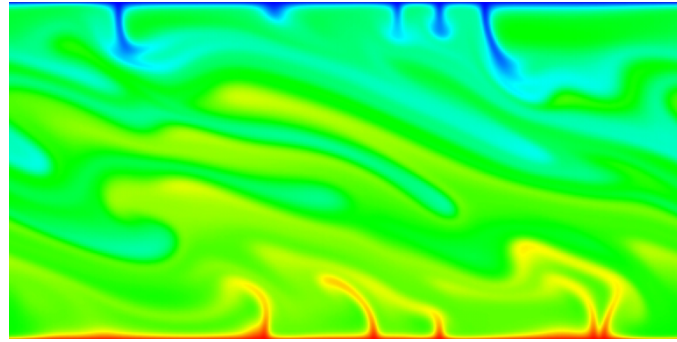


Figure 2.1: Instantaneous temperature field of chaotically convecting fluid with a strong zonal flow that moves rightward along the bottom boundary and leftward along the top one. The aspect ratio is $A = 2$, the Prandtl number is $\sigma = 10$, and the Rayleigh number is $Ra = 2 \cdot 10^7$. The hottest fluid (red) is one dimensionless degree warmer than the coldest fluid (blue). See Chapter 5 for details.

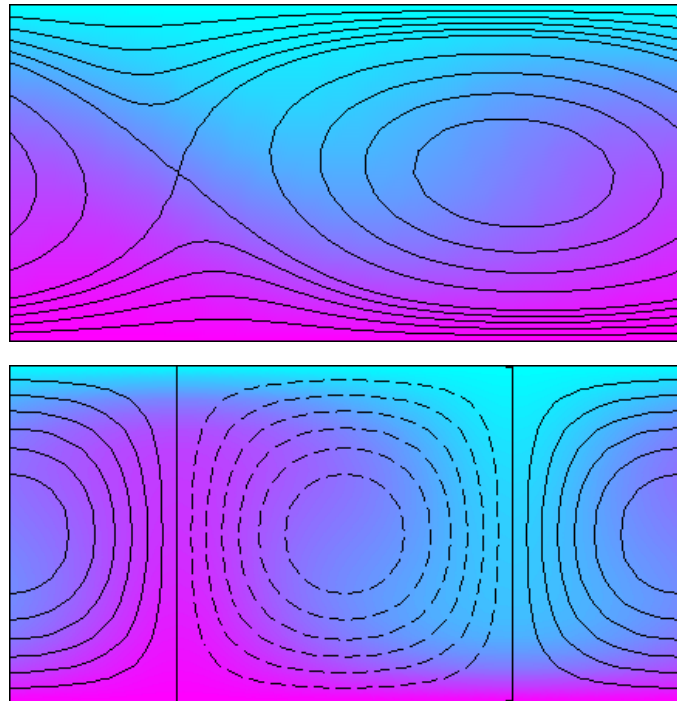


Figure 2.2: Steady convection with (top) and without (bottom) zonal flow. The parameters for both solutions are the same (aspect ratio $A = 2$, Prandtl number $\sigma = 0.1$, and Rayleigh number $Ra = 3000$), and both solutions are stable. Streamlines are dashed in regions of negative (i.e., clockwise) vorticity and solid otherwise. The hottest fluid (purple) is one dimensionless degree warmer than the coldest fluid (blue). See Chapter 3 for details.

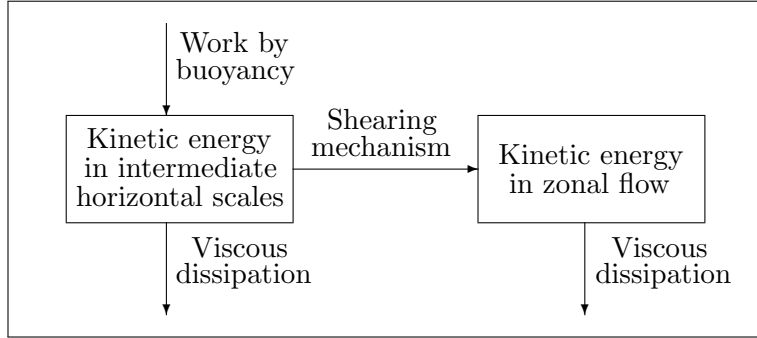


Figure 2.3: Energy fluxes in convection with zonal flow.

mechanism. Some authors have called it the tilting mechanism. The physics behind the shearing mechanism can be understood by considering the strongly shearing convection of Figure 2.1. As the hot plumes are accelerated upward by buoyancy forces, the sheared mean flow tilts them leftward. This causes them to eventually be diverted completely leftward as they approach the top boundary, feeding the zonal flow in the upper part of the domain. Cold plumes are likewise diverted rightward as they fall, feeding the zonal flow in the lower part of the domain. This same effect is at work in the steady shearing convection of Figure 2.1; the nascent hot plume tilts leftward, and the cold one tilts rightward. The zonal flows are thereby sustained against dissipation by off-diagonal Reynolds stresses that carry left-going momentum upward and right-going momentum downward, as discussed by [Thompson \(1970\)](#); [Busse \(1983\)](#); [Howard and Krishnamurti \(1986\)](#). These authors have explained the shearing mechanism conceptually by considering counter-rotating convective rolls like those in Figure 2.2, weakly perturbed by a zonal flow. The shearing mechanism is not, however, limited to flows dominated by large vortices, as the flow of Figure 2.1 demonstrates.

The mere existence of the shearing mechanism does not guarantee sustained zonal flow. The mechanism must also be strong enough to transfer energy into the zonal flow as quickly as the zonal flow dissipates energy viscously. The energy fluxes needed to sustain zonal flows are depicted in Figure 2.3; kinetic energy is injected at intermediate horizontal scales as buoyancy forces perform work on the fluid, and energy leaves these scales at an equal rate,

some of it being dissipated directly by viscosity, and the rest being transferred to the zonal flow by the shearing mechanism before being dissipated.

Since the shearing mechanism is not always strong enough to overcome dissipation, the question becomes: for what parameters can zonal flow be sustained? We will partially answer this question in Chapter 3 for a relatively simple regime in which the onset of zonal flow is controlled by bifurcations of steady states. Matters are more complicated when the onset of zonal flow is chaotic, but several qualitative trends are nonetheless clear: zonal flow is favored by *larger Rayleigh numbers, smaller Prandtl numbers, and narrower horizontal periods*. These trends have been predicted at small Ra by reduced models (Howard and Krishnamurti, 1986; Finn et al., 1992; Rucklidge and Matthews, 1996) and are confirmed at large Ra by our simulations. Our results also suggest that zonal flow can be sustained for any Prandtl number and horizontal period if the Rayleigh number is raised sufficiently.

The shearing mechanism is a generic hydrodynamical mechanism and can sustain zonal flow whenever roughly two-dimensional motions are being driven on intermediate horizontal scales, whether or not this driving is achieved by buoyancy forces. In the model of Finn et al. (1992), an intermediate horizontal mode is explicitly forced, and the shearing mechanism draws energy from this mode to sustain zonal flow. However, such explicit forcing omits a central feature of the buoyancy-driven case — the fact that the zonal flow partially suppresses the convective motions that drive it. Understanding this feedback loop is central to predicting the differences between convection with and without zonal flow.

2.3 Physical applications

The relative simplicity of our configuration — RB convection in a 2D periodic domain with free-slip top and bottom boundaries — makes it an attractive system in which to study convection-driven zonal flow, but it is not physically realizable. Each physical application

discussed in section 2.1 requires certain simplifying assumptions to yield our configuration. Here we describe the assumptions needed in two cases.

2.3.1 RB convection in an annular cylinder

To obtain our system from the annular cylinder of Krishnamurti and Howard (1981), we must approximate the boundaries as free-slip, assume the flow is radially uniform and azimuthally periodic, and ignore curvature over a single azimuthal period. Treating the boundaries as free-slip instead of no-slip in our study allows stronger zonal flows to form at smaller Rayleigh numbers, but it is not essential. Conducting preliminary simulations with our top and bottom boundaries changed to no-slip, we are still able to induce strong zonal flows, though the Rayleigh numbers needed are larger by several orders of magnitude. The assumption of radial uniformity will be more accurate when the gap between the inner and outer boundaries is narrower. Making the gap narrow thus suppresses three-dimensional effects that harm zonal flow, though it may also necessitate larger Rayleigh numbers to overcome wall drag. As for how large an azimuthal slice must be considered, the results of this Part suggest that a very narrow slice is not sufficient, but we cannot say whether the curvature of a wide slice would significantly alter our findings.

2.3.2 Tokamaks

We give here a brief, idealized description of a tokamak to illustrate the analogy between interchange motions of a plasma and 2D RB convection. This analogy and the approximations involved are discussed further by Garcia et al. (2006a), and there are many more general treatments of tokamaks (Wesson, 2011) and their zonal flows (Terry, 2000; Diamond et al., 2005).

The magnetic field lines that confine a toroidal plasma in a tokamak are helical, winding primarily in the toroidal direction with a moderate poloidal pitch. The plasma largely follows the field lines as it travels around the device. Since the plasma equilibrates very quickly along the field lines, and the field lines are nearly aligned with the toroidal direction, the plasma does not vary strongly in the toroidal direction. Certain plasma instabilities require consideration of the full 3D geometry, but interchange motions vary mainly in the radial-poloidal plane. These motions are so named because they interchange particles near the edge of the plasma with particles near the core, just as RB convection interchanges fluid between the top and bottom parts of a plane layer. Because the interchange motions are nearly two-dimensional, they often induce poloidal zonal flows — mean poloidal flows that are radially sheared.

Figure 2.4 depicts a piece of a torus and its cross-section in the radial-poloidal plane. Interchange motions in the absence of zonal flow are represented schematically, with blue and green circles representing vortices of opposite signs, respectively. In the analogy with RB convection, the plasma is treated as a magnetized fluid, interchange vortices take the place of convective rolls, and the centrifugal force takes the place of gravity, pointing outward from the torus' axis of symmetry. In the cross-section of Figure 2.4, the effective gravity acts rightward so the plasma is unstably stratified wherever its density decreased from left to right. Since the plasma is densest at its core, where new particles are added, the unstably stratified region will be roughly the right half of the cross-section shown in Figure 2.4, and it is in this region that the vortices are driven. Because the plasma equilibrates so quickly along field lines, each vortex is really part of a long vortex tube that wind helically around the plasma following field lines, thus creating interchange motions all around the edge of the plasma's cross-section. This is why interchange motions occur also in the stably stratified half of the cross-section, albeit more weakly than in the unstable half. In the cartoon of

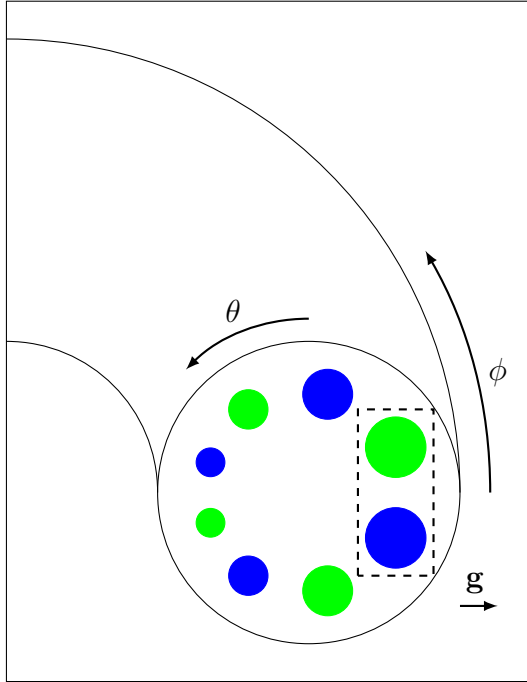


Figure 2.4: Schematic diagram representing interchange motions in a toroidal plasma. One quarter of the torus and its cross-section are shown. The toroidal (ϕ) and poloidal (θ) directions are indicated. The direction of the effective “gravitational” acceleration (g) in the plane of the cross-section is shown. Blue and green circles represent vortices of opposite signs, respectively, and larger circles indicate stronger vortices.

Figure 2.4, one might imagine there is only a single pair of counter-rotating vortex tubes, following field lines helically around the entire torus.

The argument behind replacing the cross-section of Figure 2.4 with a 2D cartesian domain has been stated elsewhere (Garcia et al., 2006b) and is as follows. Interchange motions occur primarily in the annular region near the edge of the plasma. We restrict our domain to the most unstably stratified slice of the annulus, assume periodicity in the poloidal direction, and approximate this slice as cartesian (see the dashed box in Figure 2.4). The assumption of poloidal periodicity, while not exact, is lent credence by the fact that vortices lying on the same vortex tube are indeed correlated. Finally, we arrive at our own 2D RB configuration by taking the inner and outer boundaries to be free-slip. Preliminary simulations suggest that

zonal flows still develop readily when only one boundary is free-slip, though at somewhat higher Rayleigh numbers.

The interchange motions we have described are highly undesirable. Heat is added along with particles at the core of the plasma, and the core must become very hot for fusion to occur. Interchange motions, driven by the density gradient, accelerate heat (and particle) loss. In the language of RB convection, they raise the Nusselt number. The onset of zonal flow in a tokamak improves matters because it partially suppresses interchange motions and thereby slows heat loss. This onset is association with the transition from the low-confinement mode (L-mode) to the high-confinement mode (H-mode) that has been observed in a number of experimental devices ([Wagner, 2007](#)). The analogous effect in RB convection is the lowering of the Nusselt number by zonal flow, which we quantify in Chapters [3](#) and [5](#).

Chapter 3

Steady states

3.1 Introduction

In this Chapter, we examine steady states of the 2D Boussinesq equations with and without zonal flow. We focus on small Prandtl numbers. In this regime, the first states to sustain zonal flow as Ra is raised are steady, so the onset of zonal flow can be understood by studying the system's steady states. These states and their stabilities are computed using a MATLAB code we have written for this purpose.

There are an infinite number of families of steady solutions to the Boussinesq equations, and it is neither possible nor necessary to explore every bifurcation structure these branches assume over the entire range of all three parameters (the Rayleigh number, Ra , the Prandtl number, σ , and the aspect ratio of the periodic domain, A). Our more manageable approach is to construct bifurcation diagrams for various fixed values of σ and A , taking Ra as the primary control parameter, and to focus particularly on two types of steady states that are often stable.

Bifurcations responsible for the onset of zonal flow have been studied both in the full Boussinesq equations ([Rucklidge and Matthews, 1996](#)) and in a number of modal truncations

(Howard and Krishnamurti, 1986; Hermiz et al., 1995; Horton et al., 1996; Rucklidge and Matthews, 1996; Aoyagi et al., 1997; Berning and Spatschek, 2000). Most of these studies are limited to solutions of narrow horizontal periods — that is, small A — despite the fact that the horizontal scales naturally selected in large domains are not narrow, as our results confirm. We instead focus on solutions with wider periods, which leads to the prediction that zonal flow will always set in subcritically as Ra is raised. The disappearance of the *linear* shearing instability at moderate periods is captured by certain reduced models (Hermiz et al., 1995; Berning and Spatschek, 2000). We demonstrate that the onset of zonal flow is still possible by way of a subcritical shearing instability.

In addition to examining the bifurcations responsible for the onset of zonal flow, we study the resultant steady states beyond onset. We determine their stabilities and Nusselt numbers, and we compare the latter to the Nusselt numbers of non-shearing states over ranges of Ra for fixed values of A and σ . This comparison reveals a dramatic suppression of heat transport by zonal flow, as we will also find in the unsteady flows of Chapter 5.

In section 3.2, we examine a particular bifurcation diagram in Ra and visualize the steady states represented therein. We then explore how steady states with zonal flow are affected by the horizontal periodicity and the Prandtl number in sections 3.3 and 3.4, respectively, and we discuss the Nusselt numbers of these steady states in section 3.5. Concluding remarks on the Chapter’s findings appear in section 3.6.

3.2 Visualizations of steady states

For concreteness, we first look in detail at steady states with a horizontal period of $A = 2$ and a Prandtl number of $\sigma = 0.1$. This computational domain is wide enough for the onset of zonal flow to be subcritical but not wide enough to suggest what horizontal period the flow might select in a very large domain. The only two branches of steady states that have

stable portions are shown in the bifurcation diagram of Figure 3.1. (The numerical methods used to compute all such results are fairly standard and are described in Appendix A.1.) The states comprising the branch we call TC have zonal flow, while the states comprising the branch we call L_1 do not. (This nomenclature is adapted from [Howard and Krishnamurti \(1986\)](#); the TC states take the form of *tilted cells* when the zonal flow is not very strong, while the L_1 states are modeled by the *Lorenz* equations and have a vertical mode number of 1.) Eight points are labelled on the bifurcation diagram of Figure 3.1, and the corresponding steady states are depicted in Figure 3.2. The first state shown lies on L_1 , the second state lies at the point where TC bifurcates from L_1 , and the remaining six states lie on TC , moving away from L_1 . Figures 3.1 and 3.2 apply to RB convection with *fixed-temperature* thermal boundary conditions. Analogous results for *fixed-flux* boundary conditions are quite similar, as shown in Appendix A.2.

Roll states The states we call L_1 are well known in the study of convection and consist of a pair of counter-rotating rolls that bifurcate from the static state. In fact, there are a countably infinite number of roll branches in any domain of finite period A ; for every pair of positive integers (m, n) , a branch of steady states bifurcates from the static state with m pairs of rolls in the horizontal and n rolls in the vertical. In our configuration, the (m, n) roll branch bifurcates at a Rayleigh number of $Ra_{mn} = \pi^4(k^2m^2 + n^2)^3/(k^2m^2)$, where $k := 2/A$ ([Rayleigh, 1916](#); [Chandrasekhar, 1981](#)). Few of these branches are ever stable, however. The steady rolls observed in wide domains all have vertical mode numbers of $n = 1$; these are the solution branches we call L_1 , and they exist with every horizontal period admitted by the domain. The L_1 branch of Figure 3.1 is the $(1, 1)$ roll branch; it has the same periodicity as the domain. For the present values of A and σ , this gravest L_1 branch is the only roll branch with a stable portion. As Ra is raised, the static state loses its stability when L_1 emerges stably at the critical Rayleigh number of $Ra_c = 8\pi^4$, and L_1 loses its linear stability when

the TC branch emerges subcritically at $Ra \approx 3.3 \cdot 10^4$. Beyond this Ra , the system may fall onto the TC branch, or it may transition to some unsteady state that we have not explored.

TC states Moving along TC from state 2 to state 8, the zonal flow becomes visibly more dominant. When the zonal flow is weak, as in states 3 and 4, the TC states take the form of tilted cells, betraying the origin of their name (Howard and Krishnamurti, 1986). When the zonal flow is very strong, as in states 7 and 8, the velocity field assumes a different topology: convection is performed by a single roll that has a stagnation point where its two sides meet, and which is buffered above and below by regions of roughly horizontal flow that do not contribute to vertical convection. (The intermediate states 5 and 6 each have distinct topologies as well.) Only strongly shearing TC states are stable. As the zonal flow strengthens, the operator governing the linear stability of TC loses one unstable eigenvalue in the saddle-node bifurcation at state 4 and then loses the remaining two in a subcritical Hopf bifurcation at state 7. The stability of TC persists over two decade of Ra before being lost in another Hopf bifurcation at state 8.

Symmetries The L_1 and TC branches in the bifurcation diagram of Figure 3.1 each represent larger families of steady states, though we speak of them as single branches. The solution set to which a particular L_1 state belongs can be generated by horizontal translation. Generating the full solution set of a TC state requires horizontal reflection along with translation since TC states have broken an additional symmetry of the PDE. If one breaks the translational symmetry by choosing a particular L_1 branch, TC then emerges from L_1 in a pitchfork bifurcation, where the two branches of the pitchfork are interchanged by negating the sign of the zonal flow, $\bar{u}(z)$. The L_1 and TC branches appear as single curves in Figure 3.1 because the schematic parameter, $N - 1$, is invariant under the symmetries of the PDE.

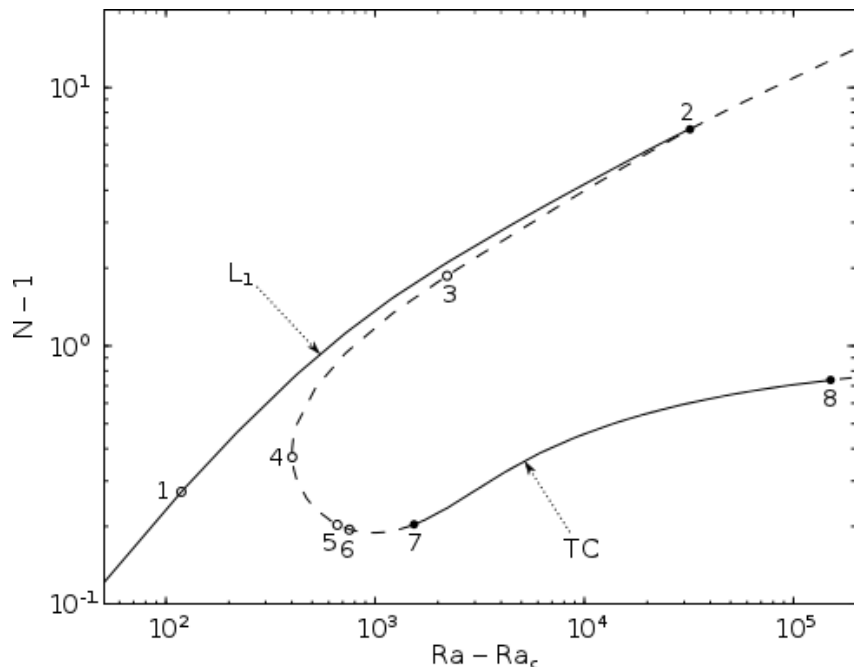


Figure 3.1: Bifurcation diagram depicting the L_1 and TC branches of steady states with a horizontal period of $A = 2$ for a fluid with $\sigma = 0.1$. Stable (—) and unstable (---) states are shown. Marginally stable states are indicated by dots (•), while certain generic states are indicated by circles (○). The states numbered 1 through 8 are shown in Figure 3.2. At the bifurcation of L_1 from the static state, the coordinates $Ra - Ra_c$ and $N - 1$ are both zero.

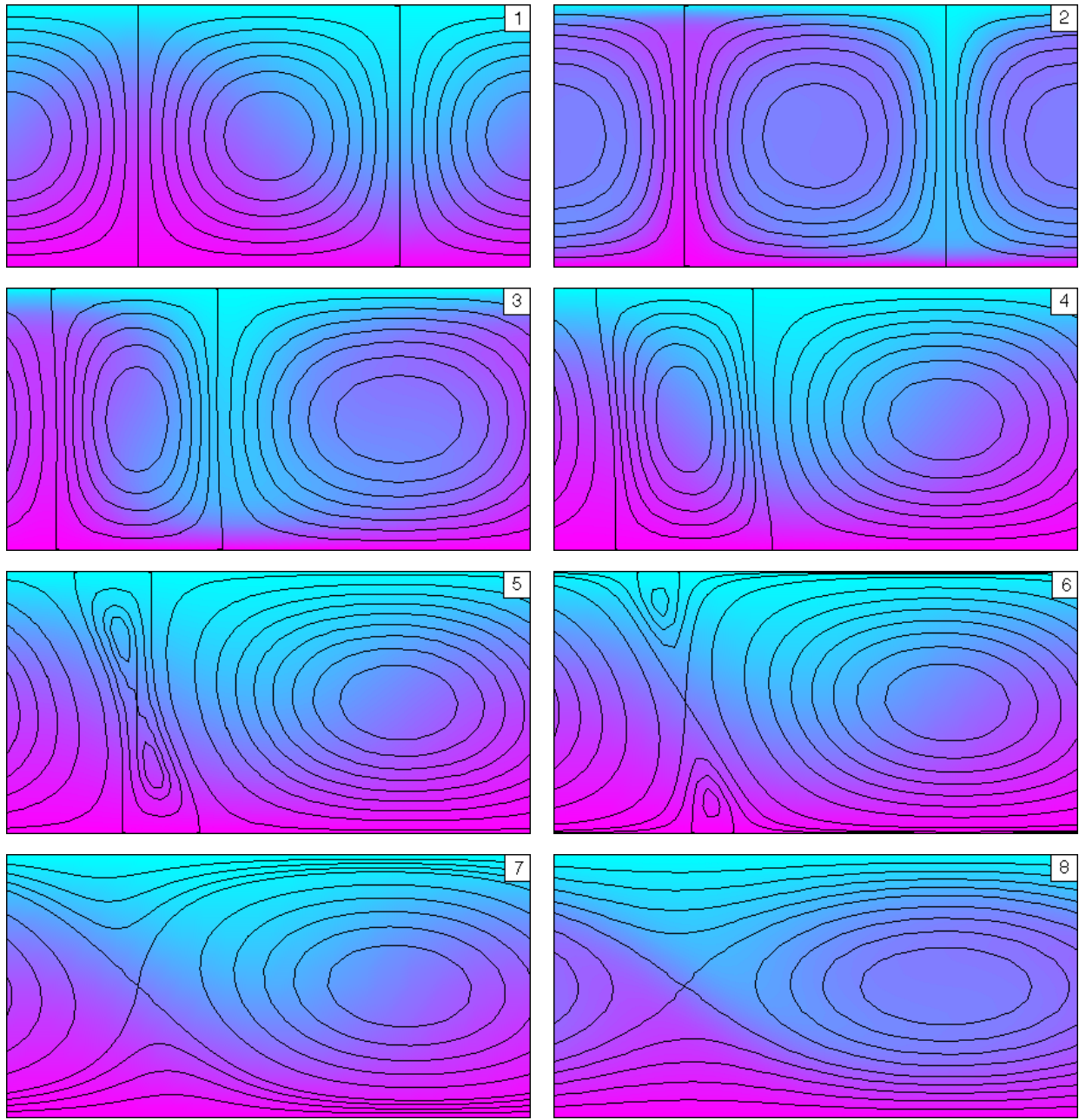


Figure 3.2: Examples of L_1 and TC steady states of the 2D Boussinesq equations with $\sigma = 0.1$ and $A = 2$. The numbers 1 through 8 correspond to points labeled on the bifurcation diagram of Figure 3.1. Solid lines are streamlines, and color represents temperature. The hottest fluid (purple) is one dimensionless degree warmer than the coldest fluid (blue). The stream function intervals between streamlines differ within and between each image. The central rolls in states 1 and 2 rotate clockwise; the dominant rolls in states 3 through 8 rotate counter-clockwise.

3.3 Effect of the horizontal period

We have observed steady shearing convection in the form of TC states with a fixed horizontal period of $A = 2$ and Prandtl number of $\sigma = 0.1$. We now clarify the relationship between the spatial period of a steady state and of its computational domain, after which we can explore how the horizontal period affects the shape and stability of the TC branch.

3.3.1 Choice of the computational domain

Steady states of period A satisfy the Boussinesq equations in any domain whose period is an integer multiple of A . However, a solution that is stable in a computational domain of period A may, in a wider domain, be unstable to perturbations by longer horizontal wavelengths. There is a danger in studying solutions with narrow periods, as previous authors have done, that the solutions will not arise in larger domains because their period is much narrower than what the flow dynamically selects. Simulating large domains would be preferable but is computationally expensive. A common compromise is to estimate the selected period in a large domain and then impose this period in further studies. However, it seems the onset of zonal flow can widen the selected period, so the computational domain needed depends on the features one wants to predict.

To predict the instability of steady rolls to perturbations of the zonal flow, it suffices to impose horizontal periodicity comparable to the selected wavelength of L_1 states. The selection of 2D rolls has been studied extensively, and periods within our range of $1.5 \leq A \leq 6$ are common ([Koschmieder, 1993](#)), so we expect that our findings will apply to the shearing instability in wider domains. To look beyond this instability and characterize the steady shearing convection that follows it, one must impose a horizontal period comparable to the selected wavelength of TC states, which has not been studied. In all of our computational domains, the only stable TC states we have found are the *gravest* such states admitted by

their respective domains. The period-2 TC states of Figure 3.1, for instance, are entirely unstable in domains of period $A = 4$ or 6 . The TC states that *are* stable in these wider domains look like states 7 and 8 of Figure 3.2, stretched to fill the domains at hand. We cannot say what the selected scale of TC states would be in very large domains, but our finding will at least show that it is much wider than the periods studied by past authors. Magnetic effects can narrow the selected scale of L_1 states (Rucklidge and Matthews, 1996), and annular geometry might do the same, but it is not known whether the selected scale of TC states is similarly affected.

3.3.2 TC branches

Bifurcation structures Figure 3.3 shows branches of TC states with $\sigma = 0.1$ and horizontal periods in the range $1.5 \leq A \leq 6$. The corresponding L_1 branches are not shown. These branches would appear similar to one another since roll states, regarded as functions of $Ra - Ra_c(A)$, vary only weakly with A and σ . The shapes the TC branches, on the other hand, vary strongly with both parameters. As A is raised from zero, the supercritical bifurcation of TC from L_1 unfolds from the primary bifurcation of L_1 from the static state (Rucklidge and Matthews, 1996). The bifurcation that begets TC continues to move outward along the L_1 branch as A is raised further, first becoming subcritical, as in the example of section 3.2 with $A = 2$, and then escaping to infinity as TC disconnects from L_1 . The TC branches in Figure 3.3 with $A \geq 3$ appear to be disconnected from their L_1 counterparts. In such cases, the *linear* shearing instability no longer exists, but zonal flow is still possible. The effect of A on the connection between L_1 and TC is qualitatively captured by the reduced model we present in the next Chapter.

Our findings of Figure 3.3 are at odds with the claim of Rucklidge and Matthews (1996) that the bifurcation of TC from L_1 occurs only for $A \lesssim 1/2$ since we have found this

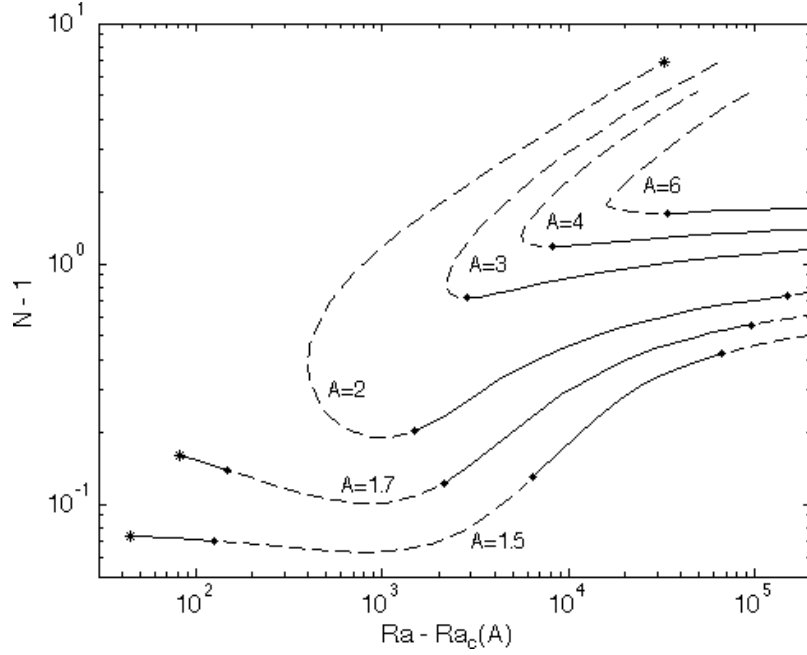


Figure 3.3: Branches of TC steady states for various A with $\sigma = 0.1$. Stable (—), unstable (---), and marginally stable (•) states are indicated, as are bifurcations in which the TC branches connect to their L_1 counterparts (*).

bifurcation at aspect ratios as large as $A = 2$ when $\sigma = 0.1$. At moderately large Ra , our linear stability computations required significantly more modes to converge than the 12 or 14 modes in each direction used by [Rucklidge and Matthews \(1996\)](#). Their computations may have still been well resolved, however, since they use a sine basis in the vertical, while we use a Chebyshev basis. The sine series is certainly better-suited to the problem at small Ra since the roll states are exactly sinusoidal at onset, but it is unclear whether a sine basis would converge faster at large Ra . We thus cannot explain the discrepancy with certainty.

Stabilities The stable windows of the TC branches shown in Figure 3.3 are computed in domains with the same horizontal period as the steady states. That is, longer-wavelength instabilities are ignored. In each domain, all shorter-period TC branches are entirely unstable. Thus, as we claimed in section 3.3.1, the horizontal periods selected in large domains will

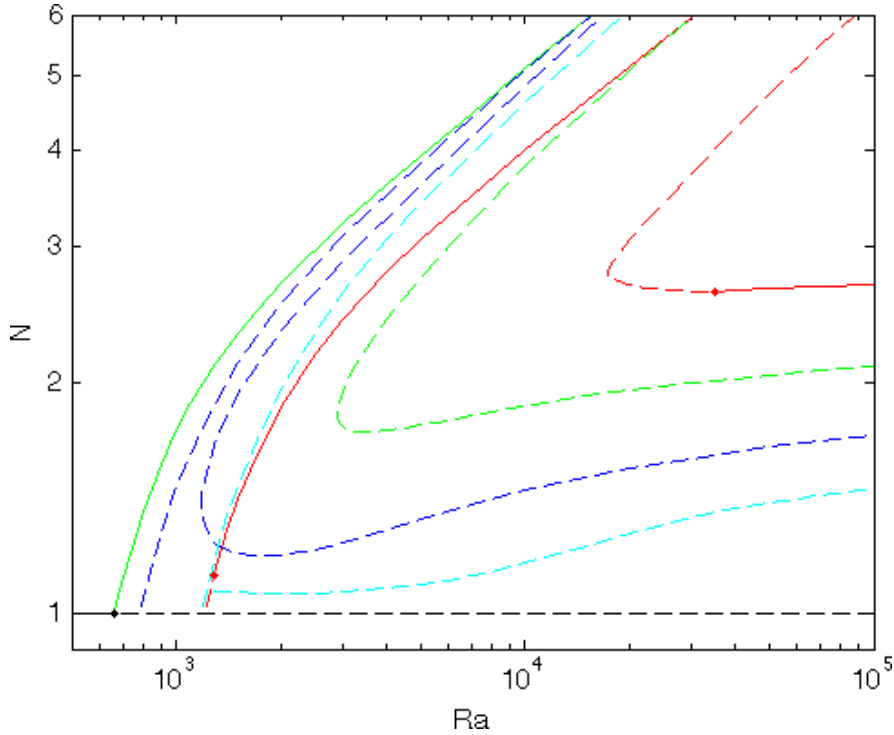


Figure 3.4: Bifurcation diagram depicting L_1 and TC branches with horizontal periods of 6 (— or ---), 3 (— or - - -), 2 (- - -), and 1.5 (- - -) with $\sigma = 0.1$ in domain period of $A = 6$. The static state is shown in black. Line style denotes where each solution branch is stable (—) or unstable (- - -), and dots (•) indicate marginally stable states.

not be narrow. We do not know whether the period-4 and period-6 TC curves are unstable to perturbations by longer wavelengths, but TC states with narrower periods are.

3.3.3 A more complete bifurcation diagram

We have discussed the fact that a domain of period A admits an L_1 branch for each horizontal mode number. The same appears to be true of TC branches. Let us illustrate concretely the coexistence of such branches. For a fluid with $\sigma = 0.1$ in a domain of period $A = 6$, the bifurcation diagram of Figure 3.4 contains the first four L_1 branches to bifurcate from the static state, along with their TC counterparts. The first solutions to bifurcate from the static state are, in order, the L_1 states with horizontal periods of 3, 2, 1.5, and 6 (that is, steady

states consisting of 4, 6, 8, and 2 convective rolls). These branches emerge at $Ra \approx 660.5$, 779.3, 1174.4, and 1202.6, respectively, and we have continued them in Ra up to at least 100 times their values at onset. The four TC branches are none other than the curves given in Figure 3.3 for these four horizontal periods, though all but the period-6 branch are unstable in this period-6 domain.

The horizontal periods the flow can select in this example are limited by the existence of stable solutions. Among steady states, there are only two possible periods: period-6 L_1 or TC states, or period-3 L_1 states. The initial stability of the period-3 L_1 branch is inevitable since it is the first to bifurcate from the static state; each branch of steady rolls inherits its stability from the static state, and the static state gains a new unstable direction each time it begets a branch of rolls. This means that the period-6 L_1 branch, which bifurcates fourth, inherits three unstable eigenvalues. Nonetheless, it quickly gains stability as Ra is increased. Such stabilization is due to subcritical bifurcations in which mixed roll branches emerge from the pure rolls branches, taking unstable eigenvalues with them ([Tuckerman and Barkley, 1990](#)). (Two horizontal modes dominate such “mixed” states, as opposed to only one in a “pure” roll state. Strictly speaking, both states contain small contributions from an infinite number of modes.) The other two L_1 states, despite bifurcating with fewer unstable eigenvalues, never gain stability for the chosen parameters. We cannot explain the stability of the period-6 TC branch in terms of eigenvalues inherited from another state because it does not intersect its corresponding L_1 branch. It may intersect some other branch of roll states at larger Ra , though we have confirmed that it does not intersect the period-6 L_2 branch — the analog of L_1 with *two* rolls in the vertical.

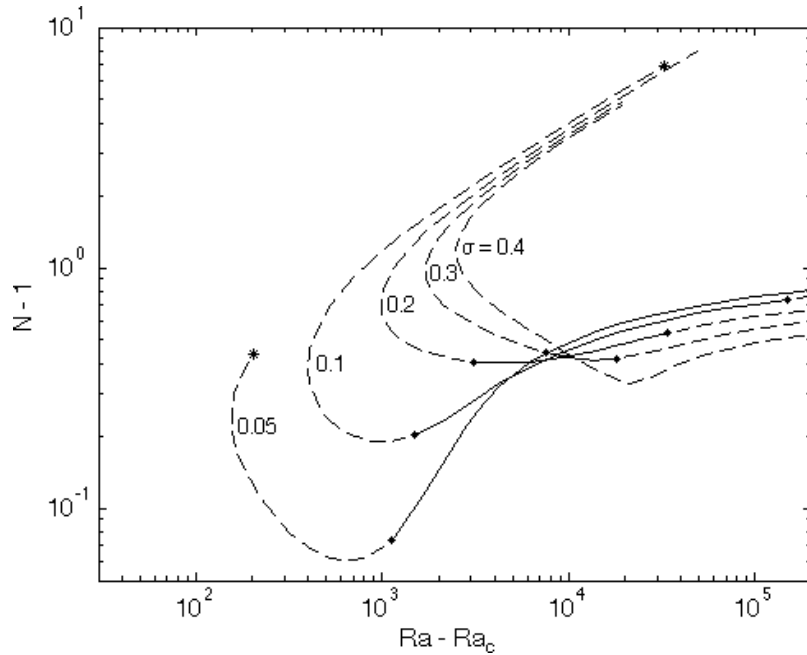


Figure 3.5: Branches of TC steady states for various small σ with $A = 2$. Stable (—), unstable (---), and marginally stable (•) states are indicated, as are bifurcations in which the TC branches connect to their L_1 counterparts (*).

3.4 Effect of the Prandtl number

Figure 3.5 shows period-2 TC branches for fluids with σ between 0.05 and 0.4. As in Figure 3.4, the stabilities indicated do not allow for longer-wavelength instabilities. When $\sigma \lesssim 0.45$, the shape of TC varies with σ much as it varies with A : the bifurcation of TC from L_1 is supercritical at very small σ (not shown), then moves outward along L_1 as σ is raised and becomes subcritical. We cannot tell whether L_1 and TC then disconnect, though they do in the next Chapter's reduced model. Once σ exceeds 0.45, TC assumes a more complicated structure as its bottom branch curves back leftward and ultimately halves its spatial period. We confine our study to the simpler TC branches that exist at small σ since this is the regime in which they are stable and hence most relevant to the onset of zonal flow.

The stability windows of the period-2 TC states in Figure 3.5 shrink with increasing σ and vanish somewhere between Prandtl numbers of 0.3 and 0.4. The stability trends of

Figures 3.3 and 3.5 together suggest that wide periods and small Prandtl numbers favor the stability of TC states. This raises the intriguing possibility that TC -like steady states could be found experimentally with a low- σ fluid in an annular domain, though it is far from certain that such states would survive in curved geometry and with experimental boundary conditions.

3.5 Nusselt numbers

The suppression of heat transport by zonal flow in steady convection is evident in every bifurcation diagram of this Chapter, all of which employ N (or $N - 1$) as the vertical coordinate. Not only do shearing states transport less heat than their non-shearing counterparts when both states coexist, but the growth *rate* of N with Ra is smaller. We will see in Chapter 5 that the same is true of unsteady shearing convection at large Rayleigh numbers.

On each of the lower TC branches shown in Figures 3.3 and 3.5, the growth of N with Ra slows as Ra increases, but we could not continue these branches far enough to confirm that N plateaus completely. Indeed, the fates of the TC branches themselves are unknown; they may continue to exist as $Ra \rightarrow \infty$, but they also may terminate on some yet-unkown solution branch or bend back leftward in saddle-node bifurcations. If any TC branches do persist for all Ra , there is an intriguing possibility that N may remain bounded on such branches as $Ra \rightarrow \infty$. For all other non-static solutions of the Boussinesq equations of which we are aware, stable or otherwise, and in the present configuration or others, N grows unboundedly with Ra .

The less pronounced heat-transporting structures in shearing convection are a clear manifestation of the suppressed heat transport. In the L_1 states, convective heat transport is accomplished primarily through the pronounced thermal plumes that align with the vertical streamlines. Since Ra is larger in state 2 of Figure 3.2 than in state 1, the rolls overturn

faster. This greatly increases the efficacy of the thermal plumes because fluid from the boundaries is carried much farther into the layer before equilibrating with its surroundings by heat diffusion. This trend is not shared by the lower-branch TC states 7 and 8 of Figure 3.2, wherein, relative to the L_1 states, the thermal plumes are much less pronounced and are not able to penetrate unimpeded along vertical streamlines; the hot and cold plumes get in one another's way. Though Ra is two orders of magnitude larger in state 8 than in state 7, the plumes are not much more pronounced.

Another way to understand why shearing flows must transport less heat than non-shearing flows is to consider the energy fluxes involved (cf. Figure 2.3). Convective transport is proportional to the work done on the fluid by buoyancy. In a quasi-steady shearing flow, this work is balanced by the viscous dissipation of the zonal and non-zonal modes. Suppose that the zonal flow were to vanish. The non-zonal modes alone will not dissipate energy as quickly as it is being injected by buoyancy, so the convection must respond by becoming more energetic. This strengthens both the dissipation by non-zonal modes and the driving by buoyancy (that is, the convective transport). The dissipation strengthens more quickly than the driving, however, so the two fluxes will find a new, higher-energy equilibrium. The quasi-steady, non-shearing flow that results must be more energetic than its shearing counterpart and, since it is more strongly driven, must transport more heat.

3.6 Conclusions

In this Chapter, we have studied steady states of the 2D Boussinesq equations with and without zonal flow. We have extended past studies by examining flows with fairly wide horizontal periods, comparable to the dynamically selected scales of convective rolls in large domains. For small- σ flow with such periods, we find that, as Ra is raised, zonal flows first become possible via a subcritical transition from a non-shearing steady state (L_1) to a

shearing steady state (TC). We have computed branches of L_1 and TC states over several decades of Ra for various horizontal periods in the range $1.5 \leq A \leq 6$ and Prandtl numbers in the range $0.05 \leq \sigma \leq 0.4$. From these branches, we have gleaned the effects of A and σ on the structures, stabilities, and Nusselt numbers of these steady states.

The connection between L_1 and TC is significantly affected by A and σ . When both parameters are small, zonal flow sets in supercritically when TC bifurcates from L_1 . As either parameter is raised, this bifurcation becomes subcritical and then disappears at infinity, after which L_1 and TC are not connected, though both branches continue to exist.

In each of our computational domains, only TC states with the same horizontal period as the domain were ever stable; TC states with narrower periods were invariably unstable to perturbations by longer horizontal wavelengths. It is unclear whether this would remain true in a very large domain, or if a horizontal period narrower than that of the domain would be selected. In either case, our findings show that the selected period would not be narrow, so studies of zonal flows in narrow domains cannot be extrapolated to large domains, except perhaps at much larger Rayleigh numbers. This fact casts doubt on the use of cartesian domains, such as our own, to study the onset of zonal flow in large, curved domains. If convective rolls in an annular domain are wide, for instance, curvature will not be negligible over their horizontal period. Above the range of σ we have studied, *steady* shearing convection is no longer stable, but we will see in Chapter 5 that unsteady shearing convection takes its place.

The suppression of heat transport by zonal flow is well known in a variety of applications (Terry, 2000; Diamond et al., 2005) but cannot generally be quantitatively predicted, so we seek to gain understanding by studying the Nusselt numbers of shearing RB convection. We have found instances in which the L_1 and TC states are both stable, and convective transport is over 10 times larger in the L_1 state. For all TC states we have computed, Nusselt numbers appear to plateau between $Ra = 10^5$ and 10^6 , though there is no guarantee that this trend

continues as $Ra \rightarrow \infty$, or even that the TC states continue to exist. Chini and Cox (2009) have shown that (unstable) steady rolls exist at large Ra and transport heat as $N \propto Ra^{1/3}$. Extending their asymptotic analysis to include zonal flow might illuminate the large- Ra fate of the TC branches and their Nusselt numbers.

The connection between L_1 and TC , or lack thereof, is captured well by the reduced model we present in the next Chapter. In the simpler context of this model, we are able to more fully explore the three-dimensional parameter space and partition it into various regimes based on the bifurcations of the steady states. It remains a future challenge to conduct a similar bifurcation study using the full Boussinesq equations, an effort that Rucklidge and Matthews (1996) have begun for solutions of narrow horizontal period.

Chapter 4

Reduced models and their bifurcation structures

4.1 Introduction

In the previous Chapter, we studied steady states of the 2D Boussinesq equations. The full bifurcation structure of its steady states is immensely complicated when considered over the entire range of the three control parameters (the Rayleigh number, Ra , the Prandtl number, σ , and the horizontal period of the domain, A). Our investigation was thus limited to small σ and moderate A and to two types of steady states — the usual convection rolls, which we call L_1 , and a state with zonal flow that we call TC . In the present Chapter, we study an eighth-order ODE model, derived from the Boussinesq equations by Galerkin truncation, that captures key features of these L_1 and TC states. Since this model is much simpler than the full PDE, we can classify all local bifurcations that steady states may undergo, and we can partition parameter space into different regimes accordingly. These findings are largely consistent with the solutions of the Boussinesq equations reported in the last Chapter.

Many ODE models have been derived by truncating a modal expansion of the 2D Boussinesq equations with our present boundary conditions. The first such models were those of Saltzman (1962) and the famous Lorenz equations (Lorenz, 1963). The sixth-order model of Howard and Krishnamurti (1986), which we call HK6, was the first to allow for zonal flow, but it was not the last (Hughes and Proctor, 1990; Hermiz et al., 1995; Thiffeault and Horton, 1996; Berning and Spatschek, 2000; Rucklidge and Matthews, 1996; Aoyagi et al., 1997; Gluhovsky et al., 2002). The eighth-order model we study here is derived by adding two modes to the HK6 truncation, so we call it HK8. The HK8 model has been described before (Gluhovsky et al., 2002), but its bifurcation structure has not been studied. We will see that it captures our findings of the last Chapter better than previously studied Galerkin models, particularly for solutions whose horizontal periods are not narrow.

The next section describes the stream function formulation of the Boussinesq equations, while section 4.3 introduces the HK6 and HK8 models. Our findings on the bifurcation structure of HK8 are summarized in section 4.4, and concluding remarks are offered in section 4.5. Further details on HK6, HK8, and other truncated models are given in Appendix B.

4.2 Stream function formulation

Equations governing 2D incompressible flow can always be reformulated in terms of a stream function, ψ , rather than the primitive velocity variables. Such a formulation is the basis of the HK8 model, as well as of the MATLAB code used to compute the last Chapter's results. (The `nek5000` code used for the next two Chapters' simulations employs primitive variables.) In addition to using the stream function in this Chapter, we will rescale the Boussinesq equations (1.8)-(1.10) in several ways to bring them into the form used by Howard and Krishnamurti (1986).

We let the stream function be defined with the sign convention $(u, w) := (\partial_z \psi, -\partial_x \psi)$, so it is related to the vorticity, ω , by $\nabla^2 \psi + \omega = 0$. We let θ represent the *negative* deviation of temperature from its linear, static profile, and we rescale the temperature by $\frac{1}{Ra}$, which moves the Rayleigh number from the momentum equation to the temperature equation. Finally, we rescale lengths such that the domain height is π , which will prove convenient when expanding in Fourier bases. The resulting equations are

$$\partial_t \nabla^2 \psi - \{\psi, \nabla^2 \psi\} = \sigma \nabla^4 \psi + \sigma \partial_x \theta \quad (4.1)$$

$$\partial_t \theta - \{\psi, \theta\} = \nabla^2 \theta + \mathcal{R} \partial_x \psi, \quad (4.2)$$

where $\{f, g\} := \partial_x f \partial_z g - \partial_z f \partial_x g$ is the Poisson bracket, $\mathcal{R} := Ra/\pi^4$ is the (scaled) Rayleigh number, and the domain is bounded by $0 \leq x \leq A\pi$ and $0 \leq z \leq \pi$. The *fixed-temperature* thermal boundary conditions require that θ vanish on the top and bottom, while the *free-slip* velocity boundary conditions require that ψ and ω vanish there. Horizontal periodicity is imposed.

In the nondimensionalization of (4.1)-(4.2), our volume-averaged definition of the Nusselt number (1.20) becomes

$$N = 1 + \frac{1}{\mathcal{R}} \langle \theta \partial_x \psi \rangle. \quad (4.3)$$

The same value of N can be obtained by considering the time-averaged heat flux across any single horizontal surface rather than over the entire volume:

$$N(z) = 1 + \frac{1}{\mathcal{R}} [\partial_z \bar{\theta}(z) + \overline{\theta \partial_x \psi}(z)], \quad (4.4)$$

The equality of (4.3) and (4.4) for all z is exact for quasi-steady solutions to the Boussinesq equations. Having this equivalence hold, in a truncated sense, for a reduced ODE model is one of the qualities that distinguishes a good truncation.

4.3 The HK6 and HK8 models

To derive an ODE model by Galerkin truncation, we must choose a finite set of orthogonal spatial basis functions and project the Boussinesq equations (4.1)-(4.2) onto them. No finite set of functions constitutes a complete basis for general solutions of the PDE, so in choosing which basis functions to include, we are selecting a particular truncation. The success of a truncation is judged relative to the features of the PDE it is meant to capture. We want to capture zonal flow, and both HK6 and HK8 do this to some extent, but we will see that HK8 is better in several ways.

4.3.1 Governing equations

The truncation of the Fourier basis used in deriving the HK8 model is

$$\boxed{\begin{aligned} \psi(x, z, t) &= \psi_{01}(t) \sin z + \psi_{11}(t) \sin kx \sin z + \psi_{12}(t) \cos kx \sin 2z + \psi_{03}(t) \sin 3z \\ \theta(x, z, t) &= \theta_{02}(t) \sin 2z + \theta_{11}(t) \cos kx \sin z + \theta_{12}(t) \sin kx \sin 2z + \theta_{04}(t) \sin 4z, \end{aligned}} \quad (4.5)$$

where $k := 2/A$ is the smallest nonzero horizontal wavenumber admitted by a domain of aspect ratio A . The dashed box encloses the HK6 truncation. Subscripts of the form $(\cdot)_{mn}$ denote the m^{th} horizontal mode number and n^{th} vertical mode number. By design, the HK8 truncation excludes the possibility of interactions between different finite horizontal mode numbers, retaining only modes with $m = 0$ or $m = 1$.

The vertical Fourier modes of truncation (4.5) contain only sine terms because the boundary conditions on ψ and θ are homogenous. On the other hand, the horizontal Fourier modes that are included in (4.5) reflect a modeling decision. The Fourier expansion of an arbitrary ψ that solves the PDE would generally include both $\sin kx \sin z$ and $\cos kx \sin z$ terms. By retaining only the $\sin kx \sin z$ term, we are fixing the boundary between the L_1 rolls at the center of the domain, as drawn in Figure 4.1, which removes the continuous translational symmetry of the PDE. This choice then determines whether sines or cosines are needed in the other terms to avoid exciting the $\cos kx \sin z$ component of ψ .

To obtain the HK8 model, one simply applies the ansatz (4.5) to the 2D Boussinesq equations (4.1)-(4.2), expands the nonlinear terms in Fourier series, and discards modes not included in the truncation. The result is an ODE governing the eight mode amplitudes (Gluhovsky et al., 2002),

$$\boxed{\begin{aligned}\dot{\psi}_{11} &= -\sigma(k^2 + 1)\psi_{11} + \sigma\frac{k}{k^2+1}\theta_{11} + \frac{k}{2}\frac{k^2+3}{k^2+1}\psi_{01}\psi_{12} & -\frac{3k}{2}\frac{k^2-5}{k^2+1}\psi_{12}\psi_{03} \\ \dot{\psi}_{01} &= -\sigma\psi_{01} - \frac{3k}{4}\psi_{11}\psi_{12} \\ \dot{\psi}_{12} &= -\sigma(k^2 + 4)\psi_{12} - \sigma\frac{k}{k^2+4}\theta_{12} - \frac{1}{2}\frac{k^3}{k^2+4}\psi_{11}\psi_{01} & +\frac{3k}{2}\frac{k^2-8}{k^2+4}\psi_{11}\psi_{03} \\ \dot{\theta}_{11} &= -(k^2 + 1)\theta_{11} + \mathcal{R}k\psi_{11} - k\psi_{11}\theta_{02} - \frac{k}{2}\psi_{01}\theta_{12} & +\frac{3k}{2}\theta_{12}\psi_{03} \\ \dot{\theta}_{02} &= -4\theta_{02} + \frac{k}{2}\psi_{11}\theta_{11} \\ \dot{\theta}_{12} &= -(k^2 + 4)\theta_{12} - \mathcal{R}k\psi_{12} + \frac{k}{2}\psi_{01}\theta_{11} & -\frac{3k}{2}\psi_{03}\theta_{11} + 2k\psi_{12}\theta_{04} \\ \dot{\psi}_{03} &= -9\sigma\psi_{03} + \frac{k}{4}\psi_{11}\psi_{12} \\ \dot{\theta}_{04} &= -16\theta_{04} - k\psi_{12}\theta_{12}.\end{aligned}} \quad (4.6)$$

The dashed box encloses the HK6 model. Many other truncated models that have been studied, including the Lorenz equations (Lorenz, 1963), are also subsets of the HK8 system.

4.3.2 Properties of the HK8 truncation

The HK8 model is the smallest truncated model to have three key virtues: it has solutions with sustained zonal flow, it is asymptotically accurate for weakly nonlinear flows, and it conserves the same quantities as the PDE in the dissipationless limit ([Gluhovsky et al., 2002](#)). We explain these properties in this section, and in section 4.4 we demonstrate a fourth virtue: the HK8 model surpasses smaller models in capturing the steady states of the Boussinesq equations that we described in the previous Chapter. We primarily contrast HK8 to HK6. The strengths and weaknesses of other previously studied truncations are discussed in Appendix B.1.

Zonal flow The modes of the HK8 model divide naturally into three groups. One group is the Lorenz triplet, $\{\psi_{11}, \theta_{11}, \theta_{02}\}$. These are the same three modes included in the Lorenz equations ([Lorenz, 1963](#)), which model a pair of counter-rotating convective rolls. We refer to steady states in this subspace as L_1 states; they are the counterparts of the L_1 states of the last Chapter that solve the steady Boussinesq equations exactly. The next group of modes is the second Lorenz triplet, $\{\psi_{12}, \theta_{12}, \theta_{04}\}$, which represent a two-by-two array of convective rolls. These are simply the Lorenz modes with their vertical mode numbers doubled ($n = 2$), and we refer to steady states in this subspace as L_2 states. In isolation, the second Lorenz triplet has the same dynamics as the first, only rescaled. When both triples are included, however, they can couple to one another and excite the final group of modes — the shear modes, $\{\psi_{01}, \psi_{03}\}$. (Neither triplet alone would couple to the shear modes, and no other shear modes would couple to the first two Lorenz triplets.) Shearing steady states in which all eight modes are nonzero correspond to the TC states studied in the last Chapter, and we refer to them as such.

Asymptotic accuracy The HK8 model captures the L_1 and L_2 steady states asymptotically well near their respective bifurcations from the static state. The Rayleigh number at which L_1 bifurcates from the static state is captured exactly because the solution to the PDE at bifurcation consists of only ψ_{11} and θ_{11} , up to horizontal translation. That is, the marginal eigenmode of the static state's linear stability operator is sinusoidal.) Furthermore, θ_{02} is the next mode to enter into amplitude expansions about this bifurcation, so including the entire Lorenz triplet makes HK8 asymptotically accurately nearby. The accuracy of HK8 near the bifurcation of L_2 is likewise due to the inclusion of the second Lorenz triplet. The onset of zonal flow is captured asymptotically well only when it takes place in the weakly nonlinear regime, which occurs only when $A \ll 1$ or $\sigma \ll 1$.

The asymptotic accuracy of HK8 in describing L_1 and L_2 relies on using the Fourier basis for the Galerkin expansion since this basis contains the eigenmodes of the static state's stability operator. When the boundaries are not free-slip, the eigenmodes are no longer sinusoidal ([Chandrasekhar, 1981](#)), so a more complicated basis would be needed. The convenience of sinusoidal eigenmodes has motivated the use of free-slip boundaries in a number of analytical studies, including Rayleigh's seminal stability analysis ([Rayleigh, 1916](#)), despite the fact that no-slip boundaries are more realistic for many physical systems. In the present study we employ free-slip boundaries because we are interested in the physics of the convection-driven shear that they admit; the sinusoidal eigenfunctions are simply good fortune.

Conserved quantities In the dissipationless limit where viscosity and thermal diffusivity vanish, the Boussinesq equations conserve the volume integrals of energy and vorticity. The HK8 model conserves the same quantities in this limit, provided the definitions of energy and vorticity are truncated accordingly ([Gluhovsky et al., 2002](#)). The HK6 model conserves neither quantity; Energy conservation fails because θ_{04} is missing ([Thiffeault, 1995](#); Thiffeault

and Horton, 1996), and vorticity conservation fails because ψ_{03} (Finn et al., 1992; Drake et al., 1992) is missing.

The Boussinesq equations also conserve heat in the sense that a quasi-steady flow must have the same time-averaged heat flux across any horizontal surface, meaning (4.3) must equal (4.4). This will also be true in any truncation that conserves energy, such as HK8 (Thiffeault, 1995; Thiffeault and Horton, 1996). Projected onto the HK8 truncation, the volume-averaged definition of the Nusselt number (4.3) becomes

$$N = 1 + \frac{1}{4\mathcal{R}} (\psi_{11}\theta_{11} - \psi_{12}\theta_{12}), \quad (4.7)$$

while the surface-averaged definition (4.4) evaluated at the top or bottom boundary becomes

$$N = 1 + \frac{1}{\mathcal{R}} (2\theta_{02} + 4\theta_{04}). \quad (4.8)$$

When governed by HK8, time-averages of expressions (4.7) and (4.8) are equivalent (Thiffeault, 1995; Thiffeault and Horton, 1996). This is not true of HK6 since the L_2 modes ψ_{12} and θ_{12} can contribute to (4.7) without θ_{04} effecting corresponding changes in (4.8).

4.3.3 Steady states of the HK6 model

Before examining steady states of HK8, which can connect in different ways for different σ and k^2 , let us describe the simpler steady states of HK6. Like HK8, the HK6 model captures the L_1 , L_2 , and TC steady states to some extent, but these states are less similar to their counterparts in the Boussinesq equations. A schematic bifurcation diagram of the HK6 system's steady states appears in Figure 4.1, along with a representative solution from each branch. In this model, the branches of steady states always connect as shown. The L_1 and L_2 branches bifurcate from the static state and are connected by the TC branch.

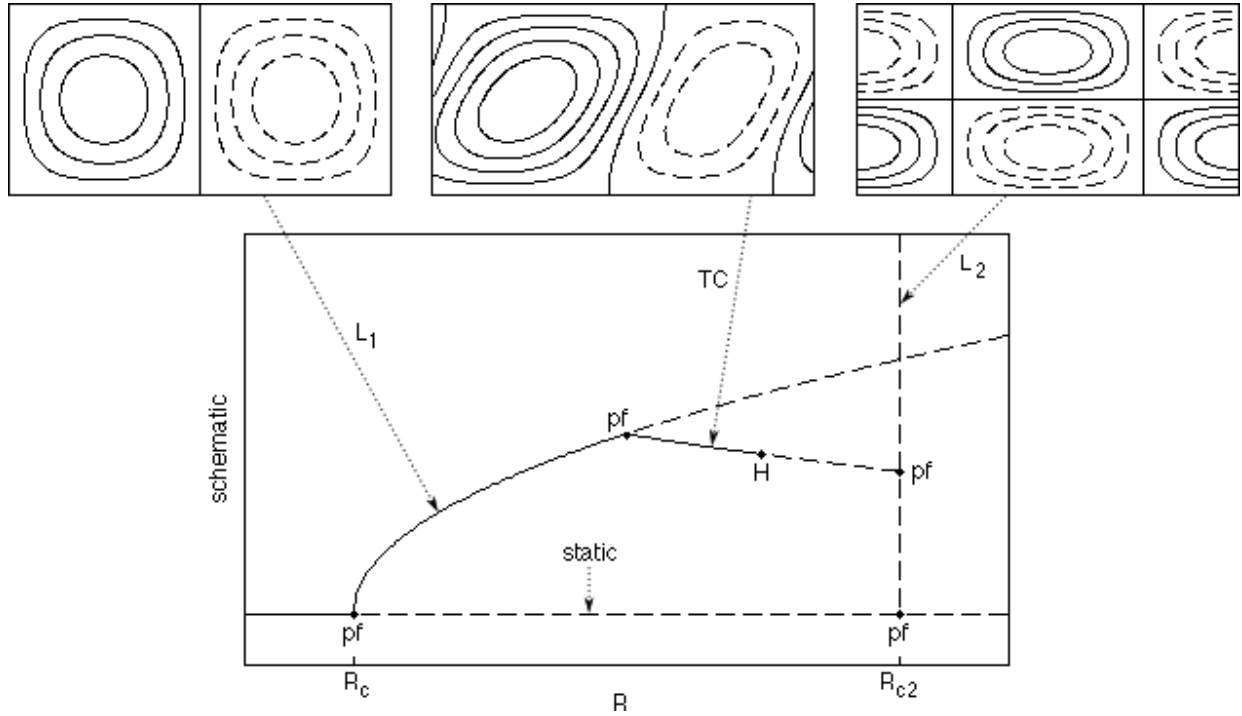


Figure 4.1: Bifurcation structure of the HK6 model, showing stable (—) and unstable (---) steady states, along with pitchfork (pf) and Hopf (H) bifurcations. Different structures of Hopf bifurcations can occur, which may alter stabilities, but the steady states always connect in pitchfork bifurcations as shown. Symmetry-related solution branches arising from pitchfork bifurcations are represented by single curves (see text). Examples of L_1 (left), TC (center), and L_2 (right) states are also shown, in which streamlines are dashed in regions of positive vorticity and solid otherwise. The L_1 and L_2 branches do not intersect.

However, the absence of θ_{02} from the second Lorenz triplet renders the L_2 branch *degenerate* in the sense that the entire branch lies at a single value of \mathcal{R} . Steady L_2 states of any amplitude are marginally stable at this \mathcal{R} , and unbounded growth occurs at larger \mathcal{R} . The HK6 structure shown in Figure 4.1 is described in [Howard and Krishnamurti \(1986\)](#), some details are clarified in Appendix B.3. Hopf bifurcations of TC and L_2 in the HK6 model are classified in Appendix B.4.

As in the bifurcation diagrams of the last Chapter, symmetry-related branches are drawn as single curves in Figure 4.1, the way they would appear if the schematic parameter were, say, the Nusselt number. The families of solutions are smaller than in the full PDE since the

HK8 model lacks translational symmetry. In both HK6 and HK8, *two* symmetry-related L_1 branches emerge from the static state in a pitchfork bifurcation at \mathcal{R}_c . These branches may be transformed into one another by reversing the directions in which the rolls rotates (that is, by negating ψ_{11} and θ_{11}). The L_2 curve also represents two symmetry-related branches, created by a pitchfork at \mathcal{R}_{c2} . There are *four* TC states that emerge from the various L_1 and L_2 branches in pitchfork bifurcations. An additional order-two symmetry is broken in these states by the way in which the zonal flow is sheared (that is, by the sign of ψ_{01}). The multiplicity of solutions could be avoided by restricting to particular signs of ψ_{11} and ψ_{01} , but this would remove interesting behaviors, such as the partial restoration of broken symmetries through global bifurcations ([Rucklidge and Matthews, 1996](#)).

The great success of the HK6 model is the existence of TC states, in which there is zonal flow, and the model has certainly provided insight into the ability of convection to drive zonal flow. However, the model's TC branch always connects to the other steady states as shown in Figure 4.1, emerging supercritically from L_1 and terminating at L_2 . We have not seen this structure in solutions to the Boussinesq equations, except when the flow is forced to have a narrow horizontal period. Thus, we must turn to the HK8 model.

4.4 Steady solutions and bifurcations of the HK8 model

In this section we classify the various ways in which the HK8 model's branches of steady states may connect, as well as the Hopf bifurcations that can occur along these branches. We give analytical results when possible and otherwise give numerical results computed with the bifurcation analysis software MATCONT ([Dooge et al., 2003](#)).

4.4.1 Steady rolls

The L_2 and TC states of the HK8 model differ substantially from their HK6 counterparts. The L_2 branch is no longer degenerate in the HK8 model, and the TC branch is no longer constrained to a single connection structure. The L_1 states of both models are simply the nontrivial fixed points of the Lorenz equations, which exist when \mathcal{R} exceeds $\mathcal{R}_c := (k^2+1)^3/k^2$ and are defined by

$$\psi_{11} = \pm 2\sqrt{2}(k^2+1)^{-1}\sqrt{\mathcal{R} - \mathcal{R}_c}, \quad \theta_{11} = \pm 2\sqrt{2}\frac{k^2+1}{k}\sqrt{\mathcal{R} - \mathcal{R}_c}, \quad \theta_{02} = \mathcal{R} - \mathcal{R}_c. \quad (4.9)$$

In HK8, where the L_2 branch is not degenerate, L_2 states exist when \mathcal{R} exceeds $\mathcal{R}_{c2} := (k^2 + 4)^3/k^2$ and are defined by

$$\psi_{12} = \pm 2\sqrt{2}(k^2+4)^{-1}\sqrt{\mathcal{R} - \mathcal{R}_{c2}}, \quad \theta_{12} = \mp 2\sqrt{2}\frac{k^2+4}{k}\sqrt{\mathcal{R} - \mathcal{R}_{c2}}, \quad \theta_{04} = \frac{1}{2}(\mathcal{R} - \mathcal{R}_{c2}). \quad (4.10)$$

The L_1 states occupy what we will call the L_1 subspace, which is spanned by the first Lorenz triplet, $\{\psi_{11}, \theta_{11}, \theta_{02}\}$. The L_2 subspace is likewise spanned by the second Lorenz triplet, $\{\psi_{12}, \theta_{12}, \theta_{04}\}$. Both the L_1 and L_2 states are independent of σ . The Prandtl number affects steady rolls in the PDE, but not dramatically. It has a much stronger effect on secondary bifurcations, such as transverse instabilities in 3D convection ([Busse and Whitehead, 1974](#)) or the shearing instabilities on we presently focus.

The Nusselt numbers of L_1 and L_2 in the HK8 model are accurate only in the weakly nonlinear regime. More generally, we know of no truncated model that accurately predicts integral quantities at large Rayleigh numbers. The Nusselt number of L_1 and L_2 in the model are $3 - 2\mathcal{R}_c/\mathcal{R}$ and $3 - 2\mathcal{R}_{c2}/\mathcal{R}$, respectively. Both expressions approach upper bounds of 3 as \mathcal{R} goes to infinity, whereas, N grows unboundedly like $Ra^{1/3}$ for steady roll state of the

Boussinesq equations (Chini and Cox, 2009). Some TC states in the model also have larger Nusselt numbers than their L_1 counterparts, which we have never seen in the PDE.

4.4.2 TC states and pitchfork bifurcations

The TC branches are defined by those steady states of the HK8 system in which all modes are nonzero. For *all* values of σ and k , TC states exist over some range of \mathcal{R} . Rather than writing down the coordinates of the TC states explicitly, which would be messy, we can infer their ubiquity by studying the linear stability of L_1 and L_2 . We find for all σ and k that at least one of the two roll branches undergoes a pitchfork bifurcation that begets the TC branch. By also considering whether these pitchforks are sub- or supercritical, we find five possible connection structures of TC in HK8, as opposed to only one in HK6.

Pitchfork bifurcations of L_1 and L_2 Since L_1 states lie in a three-dimensional subspace, the operator governing linearized perturbations to L_1 consists of two uncoupled parts: a three-dimensional matrix governing in-subspace perturbations, and a five-dimensional matrix governing out-of-subspace perturbations. The linear stability operator of L_2 similarly decomposes into matrices governing perturbations in and out of its subspace. All four matrices are given in Appendix B.2, along with further details on stability calculations for L_1 and L_2 in the HK8 model.

The only stationary bifurcations L_1 and L_2 may undergo are pitchfork bifurcations in their respective out-of-subspace directions. When these bifurcations exist, they beget TC . The L_1 pitchfork occurs at \mathcal{R}_* , where

$$\frac{\mathcal{R}_*}{\mathcal{R}_c} - 1 = \frac{27\sigma^2}{k^2 + 1} \frac{k^4 + 5k^2 + 7}{(3\sigma^2 + 10\sigma)(k^2 + 1)^2 + 2(k^2 + 4)(5k^2 - 4)}, \quad (4.11)$$

in those parts of the σ - k^2 plane where the denominator is positive. (This result is unchanged in the model of [Hermiz et al., 1995](#), that omits the θ_{04} mode.) The L_2 pitchfork occurs at \mathcal{R}_{*2} , where

$$\frac{\mathcal{R}_{*2}}{\mathcal{R}_{c2}} - 1 = \frac{27\sigma^2}{k^2 + 4} \frac{k^4 + 5k^2 + 7}{(10\sigma - 3\sigma^2)(k^2 + 4)^2 + 2(k^2 + 1)(5k^2 + 11)}, \quad (4.12)$$

when the denominator is positive. The TC branch undergoes no stationary bifurcations beyond its possible connections to L_1 and L_2 .

As in the last Chapter, our strategy for understanding TC is to draw bifurcation diagrams with \mathcal{R} as the control parameter. We computed such diagrams with the full Boussinesq equations for various fixed Prandtl numbers and spatial periods. The simplicity of HK8 allows for stronger results; we can partition the entire σ - k^2 parameter plane into regimes between which these bifurcation diagrams differ. We begin this classification with the pitchforks at \mathcal{R}_* and \mathcal{R}_{*2} , which suffice to determine how TC connects to L_1 , L_2 , or both.

Connection structures of TC The curves in the σ - k^2 plane along which the denominators of (4.11) and (4.12) vanish divide regimes in which TC does or does not connect to L_1 and L_2 , respectively. Regimes are further divided based on whether the pitchforks that exist are subcritical or supercritical. Such boundary curves are defined by cusp bifurcations, which we locate numerically using MATCONT. Here, a cusp is a codimension-two bifurcations in which a pitchfork and saddle-node collide. In a system that lacks the symmetries of HK8, a transcritical bifurcation take the place of the pitchfork.

The classification of pitchforks divides the σ - k^2 plane into the five regimes shown in Figure 4.2. The different connection structures of TC in each regime are represented schematically in Figure 4.3. Of these five structures, the HK6 model's TC branch, shown in Figure 4.1, assumes only the structure of regime 4.

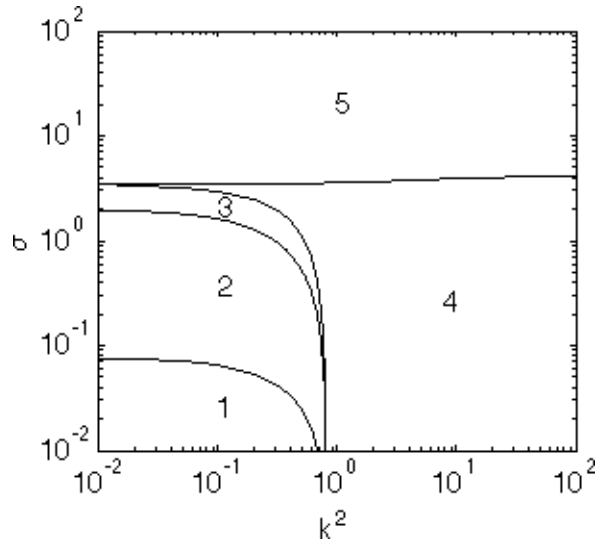


Figure 4.2: Parameter regimes characterized by the way in which TC connects to the other steady branches in the HK8 model. The five possible connection structures are depicted schematically in Figure 4.3.

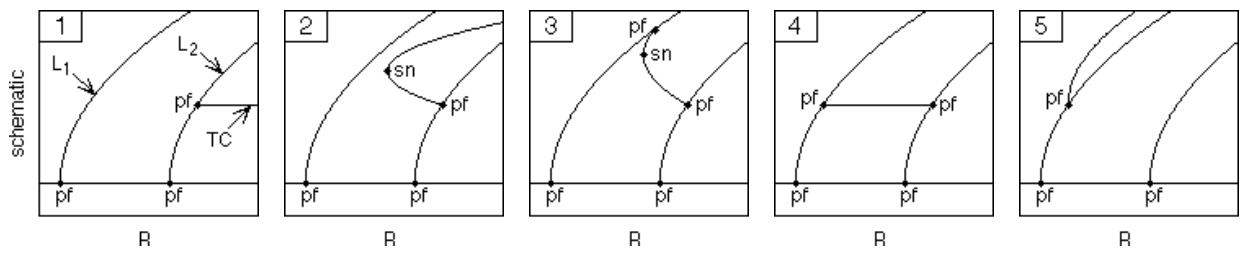


Figure 4.3: Schematic bifurcation diagrams showing the five ways in which TC may connect to L_1 and L_2 in the HK8 model. The numbering of the structures corresponds to the σ - k^2 parameter regimes of Figure 4.2. Stabilities of the steady states are not indicated because there are multiple possibilities in all five regimes, depending on the Hopf bifurcations present. Pitchfork (pf) and saddle-node (sn) bifurcations are labeled.

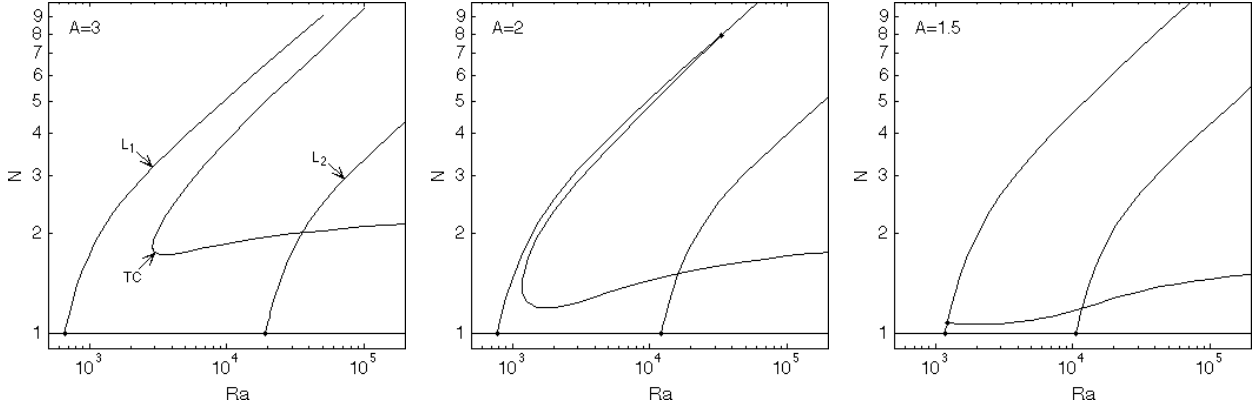


Figure 4.4: Bifurcation diagrams depicting branches of L_1 , L_2 , and TC solutions to the Boussinesq equations for $\sigma = 0.1$ and three horizontal periods: $A = 3$, 2, and 1.5 (that is, $k^2 = 4/9$, 1, and $16/9$). The bifurcations structures are similar to, respectively, the HK8 structures 2, 3, and 4 represented in Figure 4.3. The L_1 and TC branches in this Figure appear also in Figure 3.4.

Figures 4.2 and 4.3 confirm that the TC branch exists in HK8 for every combination of σ and k^2 , and that it always connects to L_1 , L_2 , or both. Steady states with zonal flow thus always exist for some range of \mathcal{R} , though they need not be stable. The stabilities of the various solution branches are not indicated in Figure 4.3 because there are multiple possibilities in each regime. We have determined each possibility by further subdividing the σ - k^2 plane according to the Hopf bifurcations present, as summarized in section 4.4.3. All possible stabilities of TC are shown in Appendix B.5.

Among the TC branches we have computed using the full Boussinesq equations, the connections to L_1 resemble either regime 2, 3, or 4 of the HK8 model. Examples of each PDE structure are shown in Figure 4.4 and can be compared to their HK8 counterparts in Figure 4.3. The primary similarity is that, at least at small σ , zonal flow sets in subcritically when the horizontal period is not narrow (that is, when k^2 is not large). Any reduced model used to study the onset of zonal flow should capture this subcriticality at moderate or wide periods since, as we saw in the last Chapter, the horizontal periods selected by the flow are indeed not narrow. The escape of the L_1 pitchfork to infinity occurs also in some

other truncated models and has been correctly identified as the disappearance of the *linear* shearing instability ([Hermiz et al., 1995](#); [Berning and Spatschek, 2000](#)), though the continued existence of *TC* states and the *nonlinear* shearing instability has not been discussed.

The primary difference between the *TC* branches of the PDE shown in Figure 4.4 and those of the HK8 model shown in Figure 4.3 is that none of the PDE’s *TC* branches terminate on their respective L_2 branches. There are an infinite number of branches on which *TC* can terminate in the PDE, if it terminates at all, whereas L_2 is the only one of these branches present in the HK8 model. The L_1 modes must couple with some higher vertical modes to drive zonal flow in the PDE, but this role need not be filled by the L_2 modes in particular.

4.4.3 Hopf bifurcations and stability

To complete our classification of local bifurcations of the HK8 steady states, we have determined the Hopf bifurcations that can occur along L_1 , L_2 , and *TC*. These bifurcations tells us where in parameter space the steady states are stable, and they beget branches of time-periodic solutions that can themselves be studied. We are especially interested in the Hopf bifurcations of *TC* because of their direct relevance to zonal flow. Time-periodic shearing solutions that emerge from *TC* in reduced models are reported by [Howard and Krishnamurti \(1986\)](#) and clarified by [Rucklidge and Matthews \(1996\)](#).

We have not systematically studied the Hopf bifurcations of *TC* in the full Boussinesq equations, so we cannot evaluate how well they are captured by the HK8 model. Moreover, even if HK8 captures these bifurcations well, it cannot fully predict the stabilities of PDE solutions since it neglects the interaction of different horizontal modes. We describe our findings on Hopf bifurcations only briefly here since we do not yet know how well they apply to the full PDE. The complete classification of local bifurcations is detailed in Appendices B.4 and B.5.

Hopf bifurcations of steady rolls The L_1 and L_2 branches may each undergo one Hopf bifurcation. In each case, the resulting time-periodic solutions remain in the respective Lorenz subspace, so zonal flow is not excited. Locating the TC Hopf bifurcations analytically is nearly intractable, but we can sometimes infer their existence or non-existence based on whether the roll branches undergo Hopf bifurcations before or after connecting to TC , and these latter Hopf bifurcations are not hard to find analytically. The way in which the L_1 and L_2 Hopf bifurcations correlate to those of TC is explained in Appendix B.4; here we give only their locations.

The stability of L_1 to in-subspace perturbations is precisely the stability of the nontrivial fixed points of the Lorenz equations; when $\sigma < 1 + 4/(k^2 + 1)$, an in-subspace Hopf bifurcation exists at \mathcal{R}_H , where

$$\frac{\mathcal{R}_H}{\mathcal{R}_c} - 1 = (\sigma + 1) \frac{\sigma(k^2 + 1) + (k^2 + 5)}{\sigma(k^2 + 1) - (k^2 + 5)}. \quad (4.13)$$

For the canonical parameter values study by Lorenz (1963), no steady or periodic solutions are stable beyond the Hopf bifurcation of L_1 , so raising \mathcal{R} past \mathcal{R}_H leads immediately to chaos. Because the larger HK8 model accommodates other solutions that may be stable, such as the TC states, parameter values that produce chaos in the Lorenz equations will not necessarily do so here.

Expression (4.13) is arranged differently than usual (Lorenz, 1963; Howard and Krishnamurti, 1986) to reveal its parallels to the L_2 Hopf bifurcation. When $\sigma < 1 + 16/(k^2 + 4)$, L_2 undergoes an in-subspace Hopf bifurcation at \mathcal{R}_{H2} , where

$$\frac{\mathcal{R}_{H2}}{\mathcal{R}_{c2}} - 1 = (\sigma + 1) \frac{\sigma(k^2 + 4) + (k^2 + 20)}{\sigma(k^2 + 4) - (k^2 + 20)}. \quad (4.14)$$

This bifurcation is absent from the HK6 model due to the omission of the θ_{04} mode. A different Hopf bifurcation occurs on L_2 in HK6, but, as discussed in Appendix B.4, we expect it is an artifact of the non-conservative truncation.

Hopf bifurcations of TC The possible structures of Hopf bifurcations along TC divide the σ - k^2 parameter plane into six regimes, as described in Appendix B.4. The only boundaries that can be found analytically are those that coincide with the crossing of pitchfork and Hopf bifurcations on the roll branches — that is, the boundaries defined by $\mathcal{R}_* = \mathcal{R}_H$ and $\mathcal{R}_{*2} = \mathcal{R}_{H2}$. Other boundaries are found by numerical continuation of various codimension-two bifurcations.

The five ways in which TC can connect to the roll branches and the six ways in which Hopf bifurcations can fall on TC define, together, twelve regimes in the σ - k^2 plane. The local bifurcations of TC are uniquely determined in each regime, and all twelve possibilities are shown in Appendix B.4. Briefly, we find that between zero and two Hopf bifurcations may occur along TC , and that TC may have a stable section but is never entirely stable. Further study of the Boussinesq equations is needed to determine whether this glut of regimes is accurate and useful.

4.4.4 Minimum Rayleigh numbers at which TC exists

Most studies of shearing convection in truncated models have focused on the linear shearing instability of L_1 at \mathcal{R}_* . This locates the onset of zonal flow when TC bifurcates supercritically from L_1 , but we have seen that TC does *not* bifurcate supercritically unless the flow is forced to have a narrow horizontal period. A useful quantity to consider is the minimum Rayleigh number at which TC exists. This value agrees with \mathcal{R}_* when the onset of zonal flow is supercritical, but it remains meaningful when this onset is subcritical.

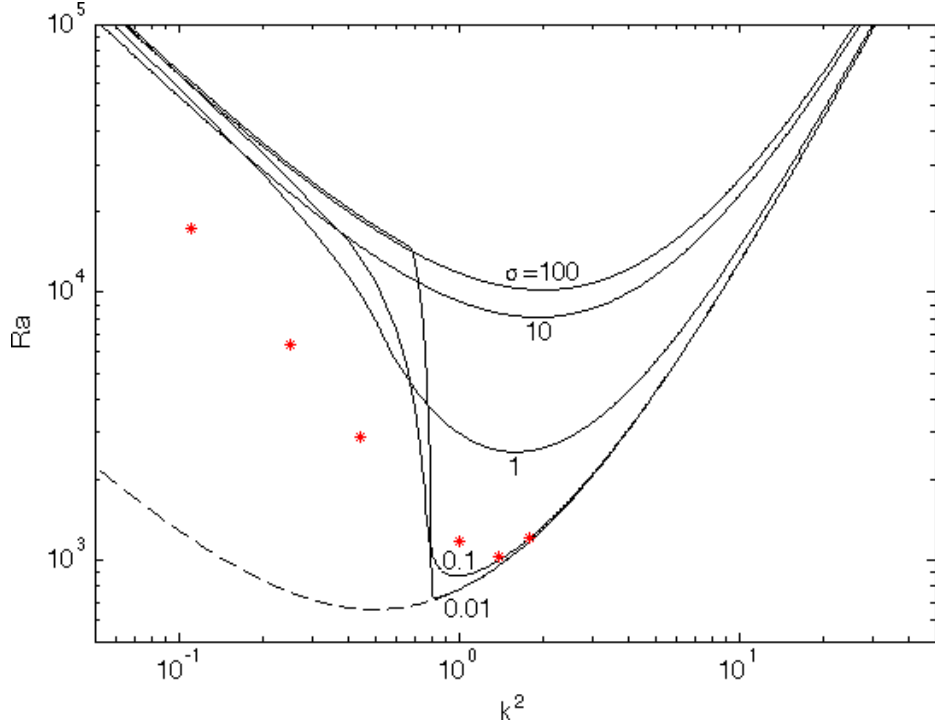


Figure 4.5: The minimum Ra at which TC states exist, Ra_{TC} , in the HK8 model (—) and Boussinesq equations (*), plotted against k^2 for various σ . Recall that $Ra := \pi^4 \mathcal{R}$ and $k^2 := 4/A^2$. Also shown is the critical Rayleigh number, Ra_c (---), above which sustained motion of any kind first becomes possible in both HK8 and the Boussinesq equations.

At the Rayleigh number where it first appears, TC is often unstable in both the Boussinesq equations (cf. Chapter 3) and the HK8 model (cf. Appendix B.5). Nonetheless, this Rayleigh numbers has physical meaning; it is the minimum Rayleigh number at which the shearing mechanism is sufficiently strong to pump energy into the zonal flow as quickly as the zonal flow dissipates it. So, even if *steady* shearing convection is unstable, *unsteady* shearing convection can often be found, both in the Boussinesq equations and the HK8 model.

Minimum Rayleigh numbers at which TC states exist, Ra_{TC} , are shown Figure 4.5 as a function of k^2 . (Recall that $Ra := \pi^4 \mathcal{R}$.) Curves predicted by HK8 are shown for various values of σ , along with Ra_{TC} for the full Boussinesq equations at six different k^2 with $\sigma = 0.1$. The critical Rayleigh number, Ra_c , is also shown. As Ra is increased from zero, sustained

motion begins at Ra_c in the form of steady rolls, and we speculate that sustained shear, steady or unsteady, can set in at or near Ra_{TC} if the flow is properly perturbed.

When a very narrow horizontal period is imposed, zonal flow sets in supercritically just after the primary convective rolls. This fact been noted repeatedly ([Howard and Krishna-murti, 1986](#); [Rucklidge and Matthews, 1996](#), e.g., by) and is reflected by the small difference between Ra_{TC} and Ra_c at large k^2 in Figure 4.5. As the horizontal period is widened (that is, as k^2 is decreased), the HK8 curves of Figure 4.5 predict behavior not captured by smaller reduced models. At very small k^2 , Ra_{TC} is much larger than Ra_c . The effect of σ is felt primarily in the transition between the small- k^2 or large- k^2 regimes, which becomes much more sudden as σ is lowered. Comparing the Ra_{TC} curve predicted by the HK8 model for $\sigma = 0.1$ to the values obtained from the Boussinesq equations, we find that HK8 captures this transition better than smaller reduced models but still over-estimates its sharpness. Further study of the Boussinesq equations is needed to test the prediction that the transition is very sharp when σ is very small

The HK8 model captures the onset of zonal flow more faithfully when Ra_{TC} is closer to Ra_c . These values approach one another when $k^2 \rightarrow \infty$ or, provided $k^2 > 4/5$, when $\sigma \rightarrow 0$. Both limits are discussed at length in Appendix B.6. The narrow-period (i.e., large- k^2) limit has received the most past attention because it is mathematically convenient, despite the fact that it is generally unrealistic in large domains.

4.5 Conclusions

In the last Chapter, we examined steady states of the 2D Boussinesq equations and focused particularly on a family of states with nonzero zonal flow — the TC states. We would like to understand the TC states since they play a central role in the onset of zonal flow, at least at small Prandtl number. In the present Chapter, we have turned to an eight-dimensional ODE,

the HK8 model, that is derived from the 2D Boussinesq equations by Galerkin truncation. The simplicity of this model let us classify the local bifurcations of TC states over the entire parameter space.

Several truncated models studied in the past, such as those of [Howard and Krishnamurti \(1986\)](#); [Rucklidge and Matthews \(1996\)](#), also admit TC states of some kind. However, we find that the HK8 model better captures our findings, reported in the last Chapter, on how TC states bifurcate from roll states. In particular, it captures the fact that zonal flow sets in subcritically when the imposed horizontal period is not narrow. A number of other features of the HK8 model, which we have described throughout section 4.4, remain to be verified by further solution of the Boussinesq equations. If these features are indeed faithful to the PDE, one might undertake further bifurcation analysis of the HK8 model, delving into periodic solutions, global bifurcations, and chaotic behavior. Studying reduced models is not a substitute for numerically analyzing the bifurcations of the Boussinesq equations, but solving the full PDE is computationally expensive and can be done more efficiently if some results can be anticipated based on reduced models.

Chapter 5

Chaotic and turbulent flows

5.1 Introduction

As the Rayleigh number is increased in RB convection, convective motion initially sets in without zonal flow. As the Rayleigh number is raised further, however, the onset of zonal flow appears to be inevitable, at least in the two-dimensional configuration we study. When this onset occurs at fairly small Rayleigh numbers, it manifests as transitions between steady states, which we have studied in the last two Chapters. When zonal flow sets in at larger Rayleigh numbers, the transition is more complicated because the flows before and after the transition are unsteady. Moreover, whether or not zonal flows are steady at onset, they are chaotic at sufficiently large Rayleigh numbers. In the present Chapter, we employ direct numerical simulations to study zonal flows in time-dependent convection at moderate and large Rayleigh numbers.

Motivated by plasma physics, [Garcia and Bian \(2003\)](#); [Garcia et al. \(2006a\)](#) simulated our present configuration at a single point in parameter space: $A = 1$, $\sigma = 1$, and $Ra = 10^6$. The strong zonal flows they observed undergo pronounced relaxation oscillations, as do similar plasma-motived convection models simulated by [Garcia et al. \(2003\)](#); [Bian et al. \(2003\)](#), both

also with $\sigma = 1$. Our findings at the same Prandtl number are similar, but at larger Prandtl numbers we find that convection can drive zonal flow that remains strong at all times and thus bears more resemblance to the high-confinement mode of a tokamak (cf. section 2.3.2).

Previous studies of our configuration (and similar ones) have focused on fairly narrow spatial domains. The domains employed in the simulations of Garcia, Bian, and their collaborators, and in the bifurcation study of Rucklidge and Matthews (1996), have widths no greater than their heights. The widest convection rolls that can form in such domains are still narrower than the rolls that are dynamically selected in wide domains, so, although the selected rolls may be narrowed by magnetic effects (Rucklidge and Matthews, 1996) or curved geometry, there is ample reason to look beyond narrow domains. All simulations described in this Chapter employ a domain whose width is twice its height ($A = 2$). This places us outside the narrow-domain regime in the sense that there can be hysteresis between shearing and non-shearing convection, as is typically observed between the low- and high-confinement modes in tokamaks (Wagner, 2007).

In section 5.2, we describe convection, both with and without sustained zonal flow, of a fluid with a large Prandtl number ($\sigma = 10$). In section 5.3, we describe convection with dramatic relaxation oscillations of zonal flow in a fluid with a moderate Prandtl number ($\sigma = 1$), and we observe the damping of these oscillations as the Prandtl number is raised. Section 5.4 presents mean Nusselt numbers of shearing convection with Prandtl numbers of 1, 3, and 10 and Rayleigh numbers as large as 10^9 . These data let us discuss the degree to which zonal flows suppress heat transport, relative to RB convection without zonal flow. Section 5.5 offers remarks to conclude the Chapter and the Part. We have used the nek5000 spectral element code to simulate the Boussinesq equations, and our computational methods are summarized in Appendix C.

5.2 Sustained zonal flow with $\sigma = 10$

In this section we report on simulations of a fluid with a Prandtl number of $\sigma = 10$, driven by Rayleigh numbers in the range $10^5 \leq Ra \leq 2 \cdot 10^8$. Because zonal flow sets in subcritically with finite amplitude, there is no challenge in distinguishing between shearing and non-shearing convection. The dichotomy is clear, for instance, in Figure 5.1, which depicts mean Nusselt numbers and kinetic energies for a number of quasi-steady states.

5.2.1 Existence of states with and without zonal flow

Convection *without* zonal flow sets in when Ra exceeds $8\pi^4$ (for our chosen aspect ratio of 2; see [Rayleigh, 1916](#)) and remains possible until Ra exceeds roughly $1.7 \cdot 10^7$, the last data point for non-shearing flow (✉) in Figure 5.1. When we increase Ra further, even very slowly, zonal flow invariably sets in, and it shows no sign of abating as $Ra \rightarrow \infty$. On the other hand, solutions *with* zonal flow were not found for Ra smaller than $2 \cdot 10^6$, the first shearing data point (*) of Figure 5.1. Since zonal flow occurs only at large Rayleigh numbers, raising the Rayleigh number from zero will first cause the system to transition between a number of non-shearing states, leading to the chaotic, periodic, and quasi-periodic flows represented in Figure 5.1. Rather than trying to unravel these transitions, we simply observe that zonal flow is always present above $Ra \approx 1.7 \cdot 10^7$ and can set in at somewhat smaller Ra if non-shearing convection is subject to an appropriate finite-amplitude perturbation.

The suppression of heat transport — that is, the reduction of the Nusselt number — by zonal flow was reported for steady states in Chapter 3, and it is clear from Figure 5.1 that this suppression persists for unsteady flows at large Rayleigh numbers. We postpone a full discussion of Nusselt numbers in shearing convection until [5.4](#), after we have described the flows themselves. For now, let us merely note from Figure 5.1 that, over the range of Ra where convection with and without zonal flow coexists, the shearing flows have significantly

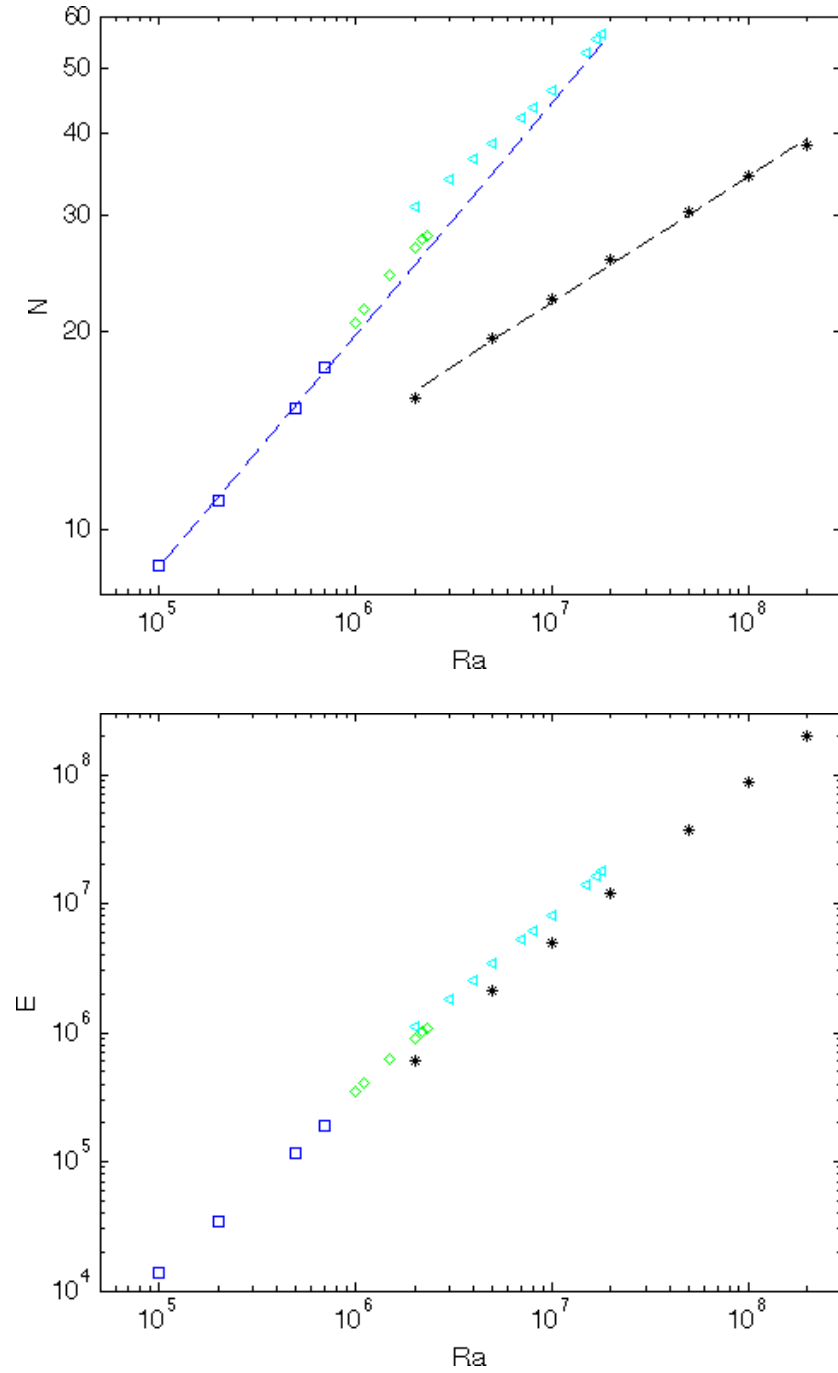


Figure 5.1: Mean Nusselt numbers (top) and kinetic energies (bottom) of quasi-steady convection with (*) and without zonal flow at various Rayleigh numbers for $\sigma = 10$ and $A = 2$. The solutions without zonal flow may be chaotic (\square), periodic (\diamond), or quasiperiodic (\triangleleft). The solutions with zonal flow are all chaotic, and three such flows are visualized in Figure 5.3. In the top plot, dashed lines show algebraic fits to the Nusselt numbers of *chaotic* solutions with (*) and without (\square) zonal flow — $N \sim 1.0 Ra^{0.19}$ and $N \sim 0.15 Ra^{0.35}$, respectively.

smaller Nusselt numbers. Moreover, though the onset of zonal flow scarcely alters the rate at which the kinetic energy, E , grows with Ra , it greatly suppresses the rate at which N grows; the shearing states of Figure 5.1 are fit well by the growth rate $N \propto Ra^{0.19}$, while the *chaotic* non-shearing states are fit well by the growth rate $N \propto Ra^{0.35}$.

In the remainder of this section, we examine in detail three of the shearing flows represented in Figure 5.1 — those with Rayleigh numbers of $2 \cdot 10^6$, $2 \cdot 10^7$, and $2 \cdot 10^8$. The smallest of these Rayleigh numbers is quite near the onset of zonal flow, while the largest is simply the largest we simulated for $\sigma = 10$. These three flows are visualized in section 5.2.2, profiles of their mean temperatures and horizontal velocities are examined in section 5.2.3, and time series of several integral quantities are examined in section 5.2.4. Many analogous results are given in section 5.3 for simulations with $\sigma = 1$.

5.2.2 Structures in shearing convection

Before the onset of zonal flow, two-dimensional convection remains visibly roll-like, as in the instantaneous temperature field of Figure 5.2, which is taken from the lowest- Ra flow represented in Figure 5.1. The thermal plumes in this chaotic flow oscillate aperiodically but have no mean drift to the left or right. Shearing convection, meanwhile, is so dominated by the horizontal zonal flow, at least at large Rayleigh numbers, that counter-rotating vortices cannot exist. Time sequences of temperature fields, taken from our three examples of shearing flows, are depicted in Figure 5.3. In all three time sequences, the mean zonal flow moves leftward along the top boundary and rightward along the bottom one, as can be gleaned from the advection of the thermal plumes. That is, the mean horizontal velocity is vertically sheared such that $\partial_z \bar{u}(z) < 0$. Symmetry could equally well break in the opposite way, in which case the sign of $\bar{u}(z)$ would be reversed.

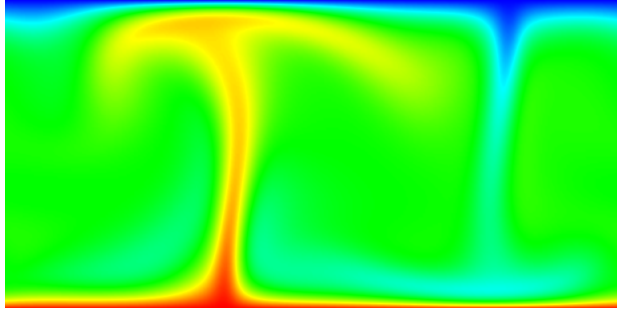


Figure 5.2: Instantaneous temperature field in chaotic convection *without* zonal flow at $Ra = 2 \cdot 10^5$, with $\sigma = 10$ and $A = 2$. The hottest fluid (red) is one dimensionless degree warmer than the coldest fluid (blue). The time-averaged Nusselt number of this flow is given in Figure 5.1, along with those of other flows with the same σ and A .

The structures in the three flows of Figure 5.3 change visibly in two main ways as Ra is increased: the thermal plumes become smaller and more numerous, and they become more strongly sheared by the mean zonal flow. As in non-shearing RB convection, the plumes shrink because the thermal boundary layers are thinning, which, in turn, means that more heat is being conducted upward across the boundary layers. That is, the Nusselt number is increasing, though not as fast as it would in the absence of zonal flow (cf. Figure 5.1). In typical RB convection, the shrinking of thermal plumes is offset by their increasing tendency to coalesce into larger composite plumes that often can penetrate all the way to the opposite boundary layer. In contrast, plumes in the shearing flows of Figure 5.3 lose coherence before reaching the opposite boundary layers. This is because the zonal flow effectively increases molecular diffusion — a phenomenon known as Taylor shear dispersion (Taylor, 1953) — thereby accelerating the dissipation of coherent structures such as plumes. Unlike the *a priori* imposed shear in basic instances of Taylor dispersion, however, convection-driven shear is driven dynamically by the very same structures it partially destroys.

In convection with zonal flow, the thermal plumes essentially modulate their own strength via the zonal flow. It is the plumes through which buoyancy forces do work on the fluid, at least at large Rayleigh numbers, so they are the source of the momentum that feeds

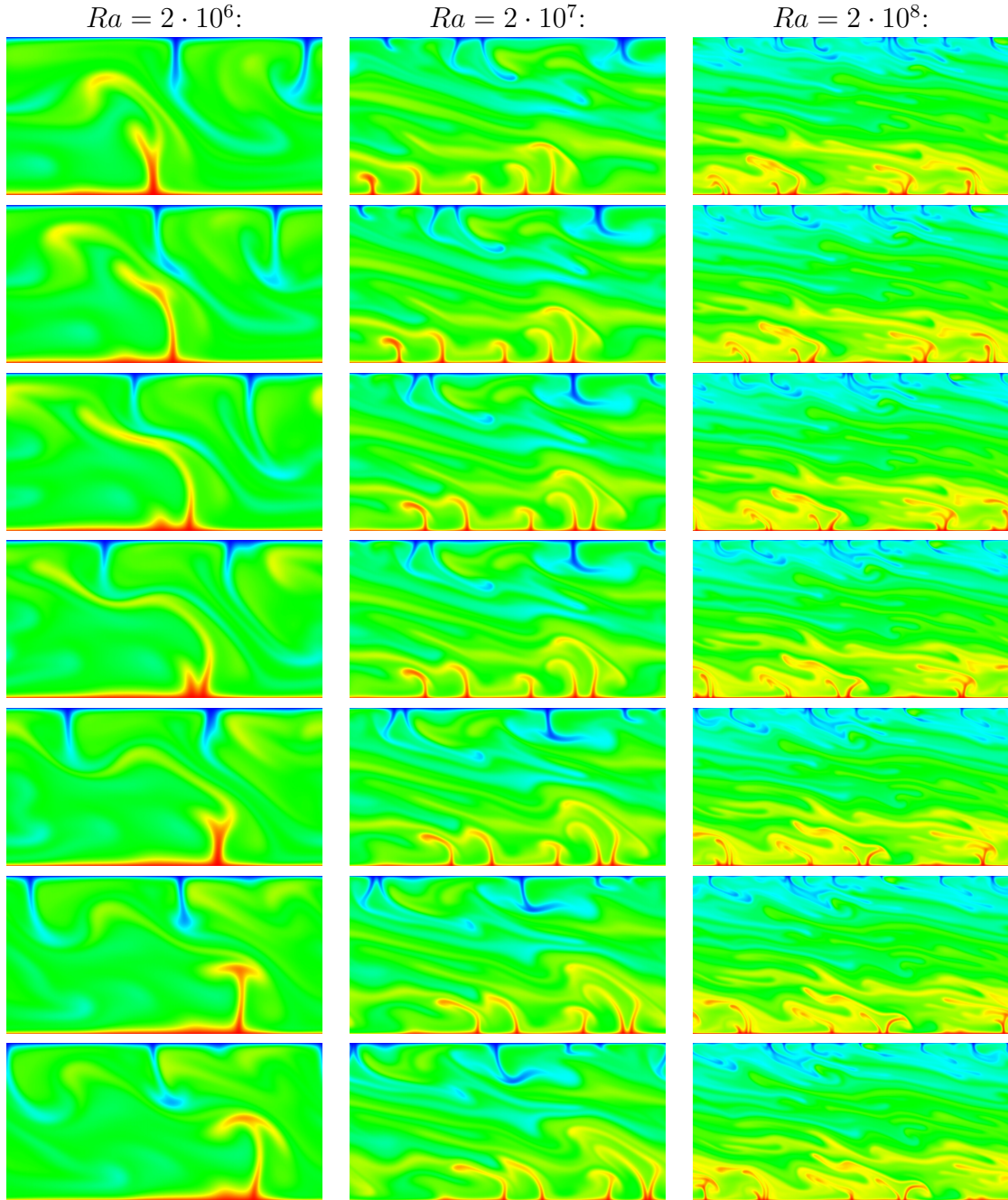


Figure 5.3: Examples of evolving temperature fields in convection with zonal flow at three different Rayleigh numbers — $2 \cdot 10^6$ (left column), $2 \cdot 10^7$ (center column), and $2 \cdot 10^8$ (right column) — with $\sigma = 10$ and $A = 2$. Within each column, time moves forward from top to bottom with time steps of $2.4 \cdot 10^{-4}$, $2.4 \cdot 10^{-5}$, and $4 \cdot 10^{-6}$, respectively. The hottest fluid (red) is one dimensionless degree warmer than the coldest fluid (blue). In all three cases, fluid moves leftward along the top boundary and rightward along the bottom boundary. Other data for these same flows are given in Figures 5.1, 5.4, and 5.5.

the zonal flow. When the plumes exceed their equilibrium strength, the zonal flow will strengthen and further disperse the plumes. Likewise, when the plumes fall below their equilibrium strength, the zonal flow will weaken and let the plumes grow. Understanding the quasi-steady equilibrium between the strength of the plumes and of the zonal flow is likely the key to predicting the strength of the zonal flow, along with the degree to which it suppresses the Nusselt number. We are yet unable to construct scaling arguments based on this equilibrium, though we give some further discussion in section 5.4.

5.2.3 Velocity and temperature profiles in shearing convection

For the three examples of shearing flows visualized in Figure 5.3, mean vertical profiles of (normalized) horizontal velocity, $\bar{u}(z)/\bar{u}_{max}$, and temperature, $\bar{T}(z)$, are shown in Figure 5.4. (Such well converged time averages are obtained by simulating over time spans thousands of times longer than those visualized in Figure 5.3.) All three velocity profiles are roughly linear in the interior, meaning the shearing of the zonal flow is roughly constant in z . This interior region is surrounded by kinetic boundary layers in which the shear stresses vanish, as is required by the free-slip boundary conditions. These boundary layers shrink as Ra is increased, and $\bar{u}(z)$ becomes ever closer to linear in the interior. The mean velocity profile thus approaches that of laminar Couette flow, though the kinetic boundary layers can never vanish entirely.

Temperature profiles in the presence of zonal flow are more complicated than their counterparts in typical non-shearing RB convection. Of the three temperature profiles shown in Figure 5.4, only the $Ra = 2 \cdot 10^6$ one resembles the profiles of non-shearing convection. That is, there are two thermal boundary layers in which heat is transported almost solely by conduction, and there is a nearly isothermal interior in which heat is transported almost solely by convection, via thermal plumes that penetrate the whole interior. The zonal flow is

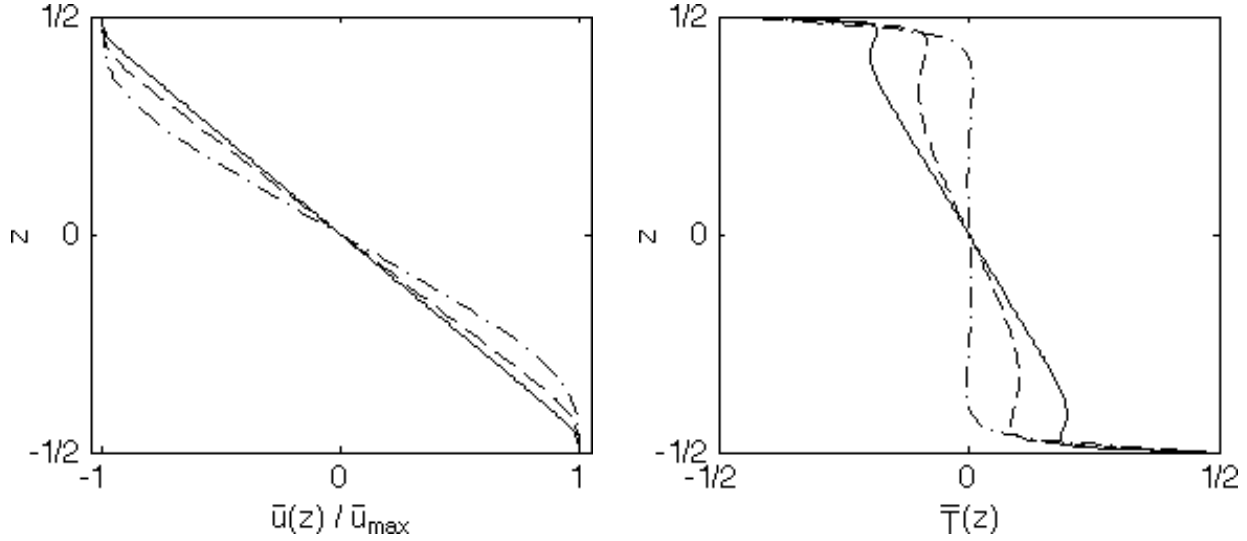


Figure 5.4: Mean vertical profiles of zonal flow (left) and temperature (right) for Rayleigh numbers of $2 \cdot 10^6$ (---), $2 \cdot 10^7$ (—), and $2 \cdot 10^8$ (—) with $\sigma = 10$ and $A = 2$. To allow comparison of the three zonal flow profiles, each is normalized by its maximum value. The zonal flows move leftward along the top boundary and rightward along the bottom boundary, as in Figure 5.3; negating $\bar{u}(z)$ yields the profile that arises when symmetry is broken in the opposite way. Other data for these same flows are given in Figures 5.1, 5.3, and 5.5, and analogous vertical profiles for $\sigma = 1$ are shown in Figure 5.8.

apparently not yet strong enough to significantly alter the $Ra = 2 \cdot 10^6$ temperature profile of Figure 5.4, but it does clearly alter the $Ra = 2 \cdot 10^7$ and $2 \cdot 10^8$ profiles. (We will verify in the next subsection that the relative strength of the zonal flow increases with increasing Ra .) In the $Ra = 2 \cdot 10^7$ and $2 \cdot 10^8$ temperature profiles, we can identify five distinct regions that are delimited by alternating signs of $\partial_z \bar{T}(z)$: two conductive thermal boundary layers, two mixing layers, and the interior region.

The different parts of the $Ra = 2 \cdot 10^7$ and $2 \cdot 10^8$ temperature profiles in Figure 5.4 can be understood in terms of the flows visualized in Figure 5.3. We must keep in mind that the mean upward heat flux is the same across any horizontal plane, but the relative contributions of convective and conductive transport vary with height. In the boundary layers, the upward heat transport is almost totally conductive since there is little vertical motion of the fluid. In the mixing layers, meanwhile, conduction actually carries heat downward, but this is

compensated for by the especially strong upward convection achieved by the thermal plumes. Beyond the mixing layers, in the interior, shear dispersion renders the plumes less coherent and less effective at transporting heat. Convection and conduction thus both contribute significantly to heat transport across the interior.

The onset of zonal flow makes temperature profiles more complicated, both because mixing layers emerge and because conductive and convective transport are both non-negligible in the interior and the mixing layers. (Recall that, in non-shearing RB convection at large Ra , mean conductive transport is negligible outside the boundary layers.) These complications show no sign of disappearing as Ra is raised; the opposite is true. Conductive flux across the interior increases as Ra is raised, as indicated by the widening temperature difference. This is necessarily accompanied by increasingly *negative* conductive transport in the mixing layers since the net conduction transport over the entire layer cannot change, being fixed by the temperature difference between the boundaries. The more complicated structure of $\bar{T}(z)$ makes it more difficult to construct scaling arguments for $N(Ra)$ in the presence of zonal flow.

5.2.4 Time series of integral quantities in shearing convection

We now turn to time series of three instantaneous integral quantities for each of our three examples of shearing flows. The first quantity we consider is the instantaneous kinetic energy, normalized by its time-averaged value, $E(t)/\bar{E}$. Normalizing $E(t)$ lets us compare flows of different Rayleigh numbers, at the expense of conveying the growth of E with Ra . However, we already know from Figure 5.1 that the growth rate of E with Ra is hardly affected by the onset of zonal flow. The second quantity we consider is the fraction of kinetic energy

due to the vertical velocity component,

$$f_w(t) := \frac{\langle w^2 \rangle^t(t)}{\langle u^2 \rangle^t(t) + \langle w^2 \rangle^t(t)}. \quad (5.1)$$

This fraction is on the order of 1/2 in non-shearing convection but becomes much smaller when zonal flow sets in. The third quantity we consider is the instantaneous Nusselt number, $N(t)$. The time series we next examine will prove particularly useful in section 5.3 when we contrast them to analogous time series for strongly oscillatory zonal flows.

Normalized kinetic energy The first row of Figure 5.5 depicts typical times series of normalized kinetic energies for our three examples of flows — $Ra = 2 \cdot 10^6$, $2 \cdot 10^7$, and $2 \cdot 10^8$. The implication of these data is that, as Ra is increased, $E(t)$ varies ever less strongly relative to its own magnitude. (The plotting ranges of Figure 5.5 are chosen to match the analogous time series in Figure 5.6 for shearing flows with $\sigma = 1$.) The normalized kinetic energy will have more to tell us when we examine strongly oscillating flows in section 5.3.

Vertical fraction of kinetic energy The second row of Figure 5.5 depicts time series of the fraction of kinetic energy due to vertical motion, $f_w(t)$, on a logarithmic scale. The closer this fraction is to zero, the more dominant the zonal flow. The zonal flow is already quite strong when it sets in at $Ra = 2 \cdot 10^6$, with $f_w(t)$ very rarely exceeding 0.2, and it becomes ever more dominant as Ra is raised; each order-of-magnitude increase in Ra creates a nearly order-of-magnitude decrease in $f_w(t)$. (The vertical kinetic energy, $\frac{1}{2}\langle w^2 \rangle$, still increases as Ra is raised, but the total kinetic energy increases more quickly, hence f_w decreases.) Like the normalized kinetic energy, $f_w(t)$ also varies less strongly relative to its own magnitude at larger Ra . It is because $f_w(t)$ remains small at all times in shearing flows that we say the zonal flow is *sustained* when $\sigma = 10$, and we liken these flows to the H-mode of a tokamak. This will not be so for the lower- σ flows examined in section 5.3.

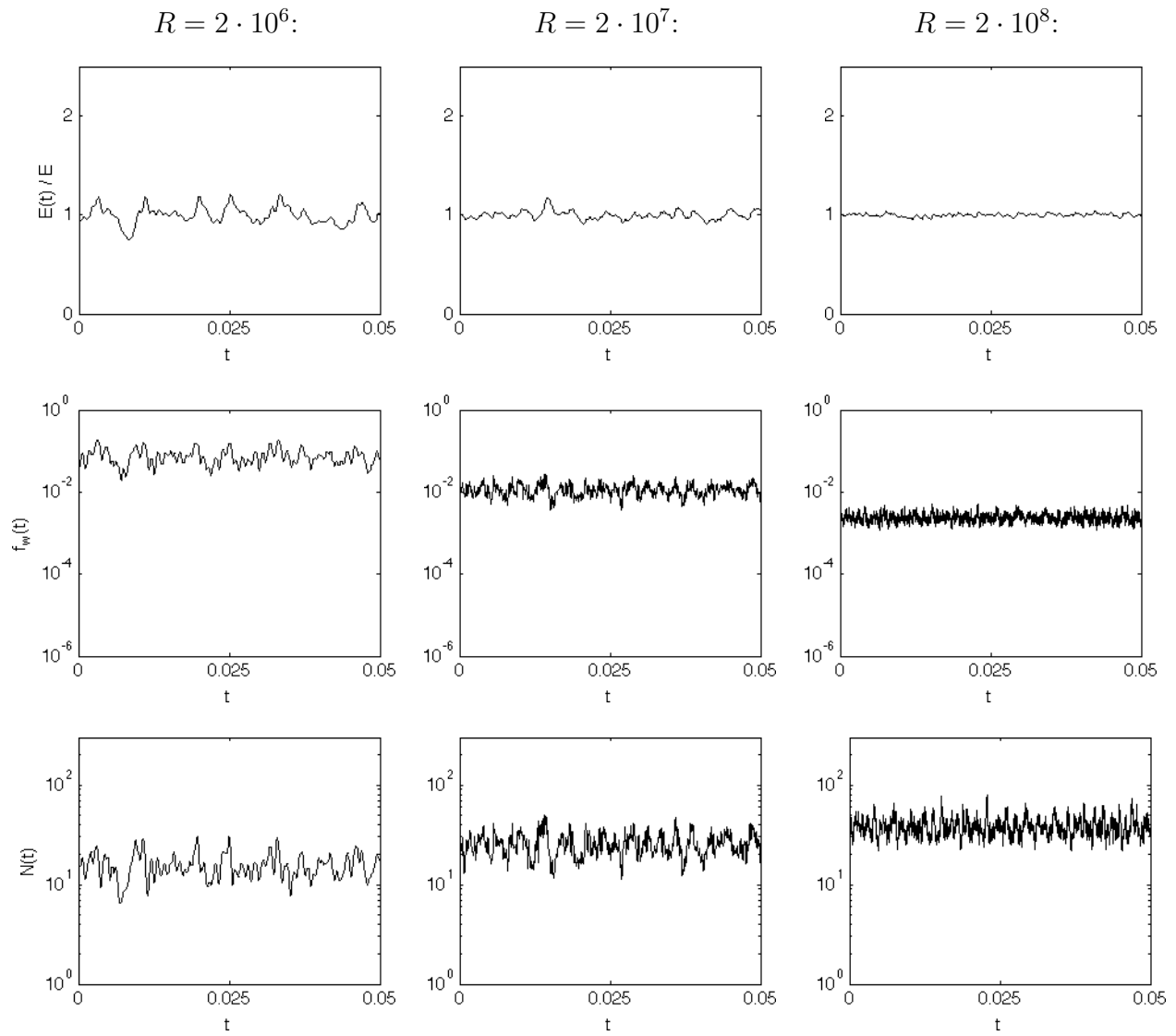


Figure 5.5: Example time series of the normalized kinetic energy (top row), the fraction of kinetic energy due to vertical velocities (center row), and the Nusselt number (bottom row) for three Rayleigh numbers — $2 \cdot 10^6$ (left column), $2 \cdot 10^7$ (center column), and $2 \cdot 10^8$ (right column) — with $\sigma = 10$ and $A = 2$. Other data for these same flows are given in Figures 5.1, 5.3, and 5.4. The large plotting ranges are chosen to match Figure 5.6, where analogous time series are shown for $\sigma = 1$.

The ever-increasing dominance of the zonal flow as Ra is raised explains our counterintuitive finding that zonal flows slow the growth of the Nusselt number but do not slow the growth of the kinetic energy (cf. Figure 5.1). One might expect that suppression of N would necessitate suppression of E since the work by buoyancy that drives the fluid is proportional to $\langle wT \rangle$ (that is, to $N - 1$). The reason this is not the case is that, as Ra is raised, an ever larger fraction of E resides in the zonal flow, which dissipates energy more slowly than smaller scales do. Said another way, the onset of zonal flow does not affect the kinetic energy strongly because it simultaneously decreases the driving of the flow and the flow's need to be driven.

In studying the role of zonal flow, the most natural decomposition of the instantaneous kinetic energy is into its instantaneous zonal part, $U(t)$, and its fluctuations, $K(t)$, defined by

$$U(t) := \frac{1}{2} \langle \bar{u}^t(z, t)^2 \rangle \quad (5.2)$$

$$K(t) := \frac{1}{2} \langle |\mathbf{u}(x, z, t) - \bar{u}^t(z, t)|^2 \rangle. \quad (5.3)$$

The quantity $f_w(t)$, on the other hand, conveys the simpler decomposition of instantaneous kinetic energy into its horizontal and vertical components. The energy in the vertical velocities, $f_w(t)E(t)$, is smaller than the fluctuation energy, $K(t)$, since it omits the horizontal fluctuations, but the two quantities scale very similarly since the horizontal and vertical fluctuations remain commensurate. It thus suffices for our purposes to examine $f_w(t)$. Some prior authors have instead taken the K - U decomposition, along with closure assumptions, in constructing ODE models that govern the evolution of select integral quantities. We discuss these models in section 5.3.5.

Nusselt number Time-averaged Nusselt numbers increase as Ra is raised in shearing convection with $\sigma = 10$; this much was already conveyed by Figure 5.1. The third row of Figure 5.5 depicts time series of $N(t)$ on a logarithmic scale for our three examples of shearing flows. The variations of $N(t)$ relative to its own magnitude, unlike those of $E(t)$ and $f_w(t)$, do not become appreciably weaker with increasing Ra . Neither do these variations become stronger, as they do in the oscillatory shearing convection to which we now turn.

5.3 Bursting and relaxation oscillations at moderate σ

The zonal flows described in section 5.2 are all *sustained* in the sense that, though they vary chaotically, they are at no instant weak; a lull in the zonal flow would cause both $f_w(t)$ and $N(t)$ to spike, and such spikes are absent from Figure 5.5. This, we will see, is a consequence of the large Prandtl number ($\sigma = 10$) of these flows. In this section, we turn to convection-driven shear at moderate Prandtl numbers, and in doing so we find zonal flows that are not nearly so sustained, instead undergoing dramatic relaxation oscillations. We will argue, however, that there is no clear dichotomy between these zonal flows and their more sustained counterparts. Rather, the oscillations become increasingly pronounced as the Prandtl number is lowered. Before demonstrating this fact, however, we will look in detail at the strongly oscillating zonal flows found in fluids with $\sigma = 1$.

5.3.1 The physics of an oscillation

Figure 5.6 depicts time series of $E(t)/E$, $f_w(t)$, and $N(t)$ in shearing convection with $\sigma = 1$ and Rayleigh numbers of $Ra = 2 \cdot 10^6$, $2 \cdot 10^7$, and $2 \cdot 10^8$. These same quantities were shown in Figure 5.5 for flows with a Prandtl number of 10 instead of 1 (and a different time span), but unlike those time series, each time series in Figure 5.6 displays pronounced nonlinear oscillations. More precisely, the kinetic energy undergoes relaxation oscillations,

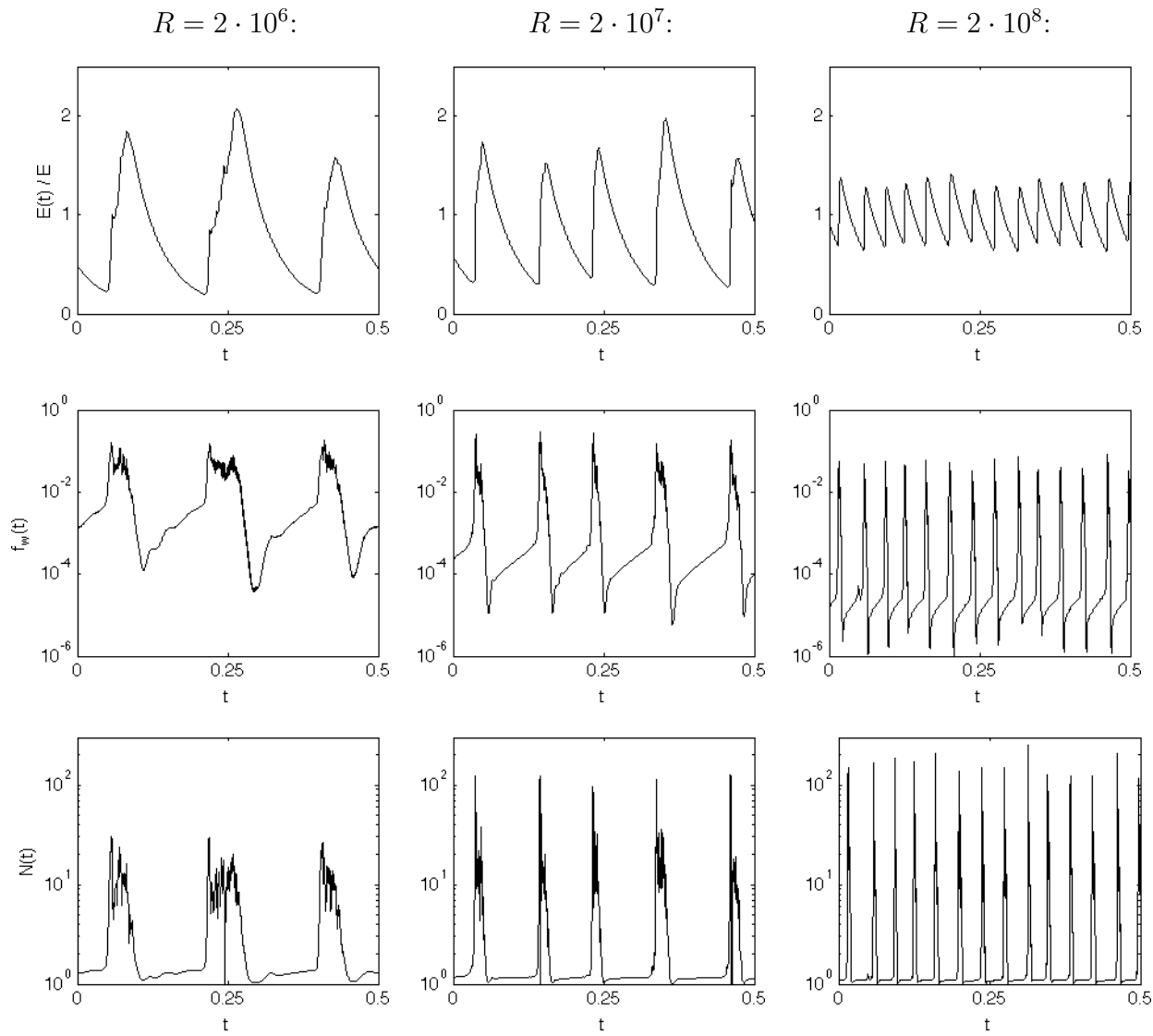


Figure 5.6: Example time series of the normalized kinetic energy (top row), the fraction of kinetic energy due to vertical velocities (center row), and the instantaneous Nusselt number (bottom row) for three Rayleigh numbers — $2 \cdot 10^6$ (left column), $2 \cdot 10^7$ (center column), and $2 \cdot 10^8$ (right column) — with $\sigma = 1$ and $A = 2$. Other data for these same parameters are given in Figures 5.8 and 5.9, and analogous time series for $\sigma = 10$ are shown in Figure 5.5.

while $f_w(t)$ and $N(t)$ undergo bursting that is synchronized with the relaxation oscillations. We refer to shearing convection with such pronounced bursting as “oscillating”, as opposed to “sustained”. In the sustained shearing flows of the last section, integral quantities do still oscillate chaotically, but these oscillations lack the distinction between slow and fast phases that is so clear in Figure 5.6.

The basic physical processes at work in the course of a shearing oscillation have been explained in the past (for instance, by Leboeuf and Charlton, 1993; Garcia et al., 2006a), and these processes can be understood by considering simultaneously the three integral quantities depicted in Figure 5.6 for, say, $Ra = 2 \cdot 10^6$. During the slow phase of an oscillation, $f_w(t)$ and $N(t)$ are small but growing slowly. The small values of $f_w(t)$ mean that zonal flow dominates, and there is very little vertical motion. Likewise, the fact that $N(t)$ is not much above unity means that very little heat is being transported convectively, so the flow is barely being driven. In the absence of appreciable driving, the flow decays viscously, so $E(t)$, which consists mostly of energy in the zonal flow, relaxes exponentially toward zero. Toward the end of a relaxation phase, all structures have been largely dispersed, and the flow is quite horizontally uniform — much more so than in the sustained shearing flows visualized in Figure 5.3. If the flow were perfectly parallel, with no vertical motion at all, this viscous decay would continue for all time as the solution approached the static state, the horizontal momentum dissipating according to the heat equation $\partial_t u(z, t) = \sigma \partial_z^2 u(z, t)$. In actuality, the relaxation of $E(t)$ is cut short as the oscillation enters its fast phase.

The fast phase begins when the zonal flow is no longer strong enough for its dispersive effects to overcome the usual mechanism of thermal instability that excites w and θ . At this point, $N(t)$ quickly grows, and $f_w(t)$ along with it. The flow is once again being energized by buoyancy forces, and strong thermal plumes and circulatory motion are created. However, the shearing mechanism quickly transfers this newfound energy into the zonal flow, as reflected by $f_w(t)$ becoming small again, and this shear then destroys the structures through

which buoyancy do work on the fluid, as reflected by $N(t)$ becoming small again. The zonal flow thus shuts off its own source of momentum and begins to decay as the flow enters the slow phase of a new oscillation.

5.3.2 Dependence of oscillations on the Rayleigh number

The shearing oscillations depicted in Figure 5.6 change in several ways as Ra is increased. The bursts become more frequent relative to the timescale of thermal diffusion, by which we nondimensionalized. The kinetic energy oscillates less strongly relative to its own magnitude, as also occurred in the $\sigma = 10$ flows depicted in Figure 5.5. The bursts of $N(t)$ and $f_w(t)$ in Figure 5.6 become more extreme as Ra is raised, contrary to the temporal variations of these quantities when $\sigma = 10$. This is another way in which a shearing flow that is firmly in the oscillating regime is clearly distinguishable from a flow that is firmly in the sustained regime, despite the fact that the boundary between the two regimes is fuzzy.

The increasing extremity of the oscillations of $f_w(t)$ and $N(t)$ manifests during both the bursting phase and the quiescent phase. At larger Rayleigh numbers, $N(t)$ grows more steeply during a burst and reaches a larger maximum value. On the other hand, the shearing mechanism is stronger, so zonal flow develops more quickly and more strongly. The bursts are thus shorter-lived, as zonal flow shuts off the convection faster, sending $N(t)$ and $f_w(t)$ back into the quiescent phase. The increasing dominance of the zonal flow is reflected in the quiescent phase by very small values of $f_w(t)$. Since raising Ra makes the Nusselt number bursts stronger but also shorter and more frequent, it is not obvious whether the time-averaged Nusselt number, N , will increase or decrease. In fact, N does not change much, as we will see in section 5.4.

5.3.3 Dependence of oscillations on the Prandtl number

As the Prandtl number is lowered from 10 to 1, the sustained zonal flow of Figure 5.5 gradually becomes the oscillating zonal flow of Figure 5.6. This transition is best understood by examining the effects of σ on $N(t)$. Time series of $N(t)$ appear in Figure 5.7 for six flows with Prandtl numbers between 1 and 10, all with $Ra = 2 \cdot 10^6$. The quasi-steady flows from which these time series are taken can be reached either by raising σ from 1 or by lowering σ from 10; we have seen no hysteresis. As the Prandtl number is lowered, the oscillations of $N(t)$ in Figure 5.7 become more extreme, and one begins to discern two different oscillation phases. Essentially, the oscillations become pronounced enough that, during the part of the oscillation where $N(t)$ is small, $N(t)$ begins to “bottom out” near unity. This is the emergence of the quiescent phase. Though the transition does not occur at a precise value of σ , it can be located approximately. Lowering σ from 10 to 3 creates visibly larger oscillations of $N(t)$, but $N(t)$ still has no quiescent phase when $\sigma = 3$, so this is clearly sustained zonal flow. The quiescent phase is hinted at in the stronger oscillations of the $\sigma = 2$ time series, a brief quiescent phase occurs during each oscillation of the $\sigma = 1.5$ time series, and the distinction between bursting and quiescence is quite pronounced when $\sigma = 1$. Thus, we can reasonably say that the transition between oscillating and sustained zonal flow occurs gradually between $\sigma = 1.5$ and $\sigma = 2$.

Since the flows represented in Figure 5.7 all have the same Rayleigh number, it is natural to ask whether the approximate Prandtl number dividing sustained zonal flow from oscillating zonal flow would be much different at a larger Rayleigh number. We expect that it would not. We saw in section 5.2 that raising Ra places convection with $\sigma = 10$ even more firmly in the sustained regime since integral quantities vary even less strongly, and we have found the same to be true when $\sigma = 3$. Likewise, raising Ra places convection with $\sigma = 1$ even more firmly in the oscillating regime since integral quantities vary even more strongly (cf.

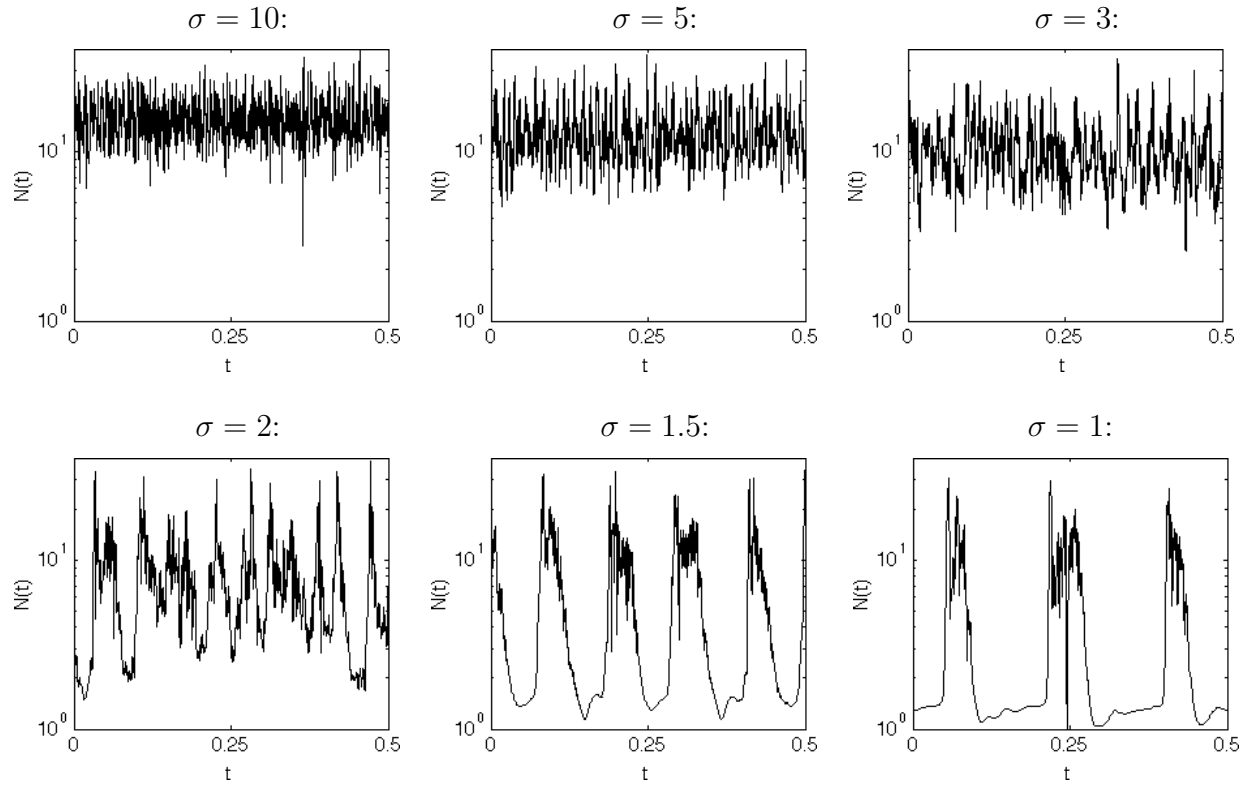


Figure 5.7: Example time series showing instantaneous Nusselt numbers for six Prandtl numbers between 1 and 10, with $Ra = 2 \cdot 10^6$ and $A = 2$.

Figure 5.5). The Prandtl number below which zonal flows are strongly oscillatory, therefore, is scarcely affected by the Rayleigh number.

5.3.4 Velocity and temperature profiles

For two of the $\sigma = 1$ flows whose partial time series appear in Figure 5.6 (the $Ra = 2 \cdot 10^6$ and $2 \cdot 10^8$ flows), mean vertical profiles of (normalized) zonal flow, $\bar{u}(z)/\bar{u}_{max}$, and temperature, $\bar{T}(z)$, are shown in Figure 5.8. The zonal flow profiles, like their $\sigma = 10$ counterparts in Figure 5.4, are roughly linear outside of the kinetic boundary layers. The temperature profiles, meanwhile, are much closer than their $\sigma = 10$ counterparts are to the linear temperature profile of the static state; outside the inner boundary layers, conduction carries heat upward

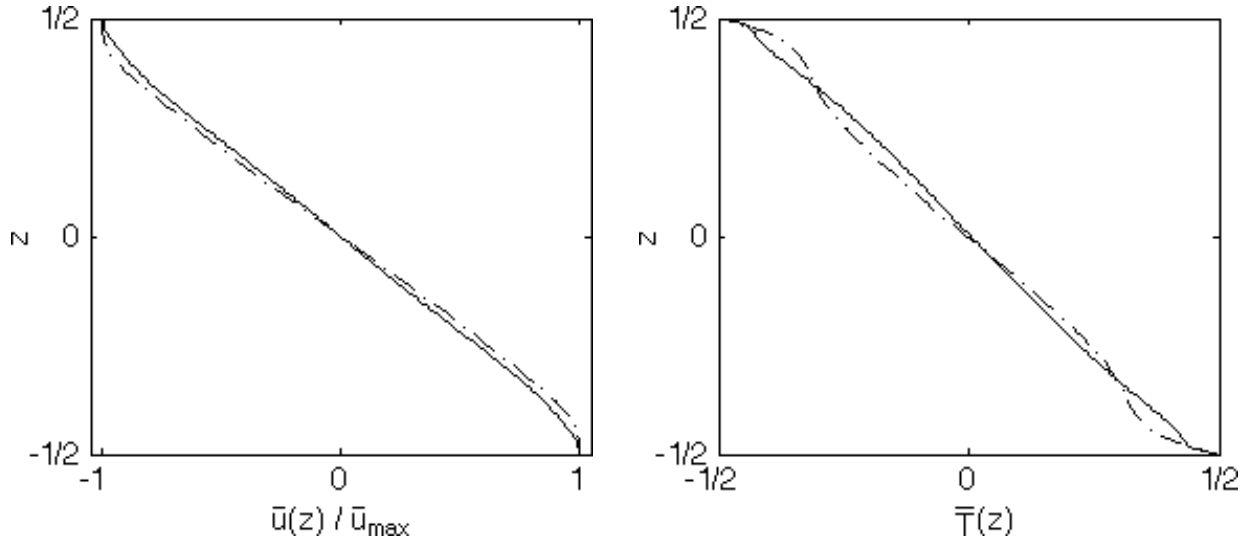


Figure 5.8: Vertical profiles of horizontally averaged horizontal velocities (left) and temperatures (right) for Rayleigh numbers of $2 \cdot 10^6$ (---) and $2 \cdot 10^8$ (—) with $\sigma = 1$ and $A = 2$. To allow comparison of the three velocity profiles, each is normalized by its maximum value. The velocity profiles represent fluid moving leftward along the top boundary and rightward along the bottom boundary, as in Figure 5.3; negating $\bar{u}(z)$ yields the profile that arises when zonal flow breaks symmetry in the opposite way. Other data for these same parameters are given in Figures 5.6, 5.9, and 5.5, and analogous vertical profiles for $\sigma = 1$ are shown in Figure 5.4.

only slightly more slowly than it does in the static state, though it is now accompanied by convection.

We saw in section 5.2.3 that, in convection with sustained zonal flow, the interior region of the flow is clearly distinguished from the mixing layers. This is because *convective* transport is much stronger in the mixing layers, where the thermal plumes are strong, than in the interior, where the plumes have been dispersed by the sheared zonal flow. On the other hand, the interior and the mixing layers are scarcely distinguished in a time-averaged temperature profile of convection with oscillating zonal flow. This is because, when the zonal flow oscillates strongly, the thermal plumes either penetrate the entire layer (during a burst) or scarcely exist at all (during the quiescent phase). The time-averaged slope of $\bar{T}(z)$ thus changes little across the layer.

5.3.5 Reduced models of oscillating zonal flow

In the plasma physics literature, several reduced models have been proposed that capture the sort of relaxation oscillations of zonal flow that we and others ([Garcia and Bian, 2003](#); [Garcia et al., 2006a](#)) have seen in convection with $\sigma = 1$. The resemblance these oscillations bear to the behavior of simple predator-prey population models, especially the Lotka-Volterra equations ([Lotka, 1925](#)), has been pointed out many times, perhaps first by [Leboeuf and Charlton \(1993\)](#). In this analogy, the place of the predator population is taken by a quantity undergoing relaxation oscillations, such as the zonal flow energy, $U(t)$, and the place of the prey population is taken by a bursting quantity, such as the fluctuation energy, $K(t)$. Such an ODE model may help in understanding the zonal flow's oscillations conceptually, though it cannot capture their full complexity.

Strongly nonlinear relaxation oscillations of the zonal flow have *not*, to our knowledge, been reported for any ODE derived from the Boussinesq equations solely by Galerkin truncation, nor have we found such oscillations in the HK8 model. A small number of modes is apparently insufficient to capture the great separation between fast and slow timescales found in oscillations of the full PDE. Low-order models that display predator-prey-type oscillations *have* been derived from the Boussinesq equations, but they have all made closure assumptions. In some cases, these closure assumptions have been applied after Galerkin truncation ([Horton et al., 1996](#); [Garcia and Bian, 2003](#)). In other cases, assumptions are used to close a set of integral relations governing the evolution of several of the PDE's volume integrals, such as $U(t)$ and $K(t)$ ([Leboeuf and Charlton, 1993](#); [Malkov et al., 2001](#); [Bian and Garcia, 2003](#)). Ultimately, however, the full Boussinesq equations must be solved to obtain quantitatively accurate results at large Rayleigh numbers regarding, say, how the zonal flow strength and Nusselt number scale with the control parameters.

5.4 Nusselt numbers in convection with zonal flow

We now turn to the dependence of the Nusselt number on Ra and σ in convection with zonal flow. In typical RB convection, where $N(Ra, \sigma)$ is not significantly altered by mean flows, this dependence has been the subject of many physical and computational experiments, and of many scaling arguments meant to explain these experiments (see the review by Ahlers et al., 2009). For convection with oscillating zonal flow in a system similar to our own, Garcia et al. (2003) report the slow growth rate of $N \propto Ra^{0.08}$ with $\sigma = 1$ and $A = 1$. Beyond this result, $N(Ra, \sigma)$ in shearing convection has not, to our knowledge, been systematically studied.

For chaotic shearing flows with Prandtl numbers of 1, 3, and 10, mean Nusselt numbers are shown for various Rayleigh numbers in Figure 5.9. For the *sustained* shearing convection that occurs with $\sigma = 3$ and $\sigma = 10$, the Nusselt number grows roughly algebraically with the Rayleigh number — as $Ra^{0.077}$ and $Ra^{0.19}$, respectively. These growth rates fall below those expected in non-shearing RB convection, which fall between $Ra^{1/5}$ and $Ra^{1/2}$ (see the scaling arguments of Grossmann and Lohse, 2000, and the experimental results summarized therein). We are thus outside the purview of the Grossmann-Lohse scaling theory.

Since $N(Ra)$ grows more slowly when $\sigma = 3$ than when $\sigma = 10$, one expects the zonal flow to be more dominant when $\sigma = 3$ since it is the zonal flow that suppresses the growth of $N(Ra)$. This is indeed the case, as can be gleaned from Figure 5.9, where smaller vertical fraction of kinetic energy, f_w , indicate relatively stronger zonal flows. The increasing dominance of the zonal flow as Ra is raised is likewise evident from the decay of f_w . This decay is approximately algebraic in Ra , with similar decay rates at both Prandtl numbers.

For the *oscillating* shearing convection that occurs when $\sigma = 1$, the Nusselt number does not grow algebraically with Ra , as it does when σ is larger (cf. Figure 5.9). At Ra values smaller than those included in Figure 5.9, there exist periodic and quasiperiodic shearing

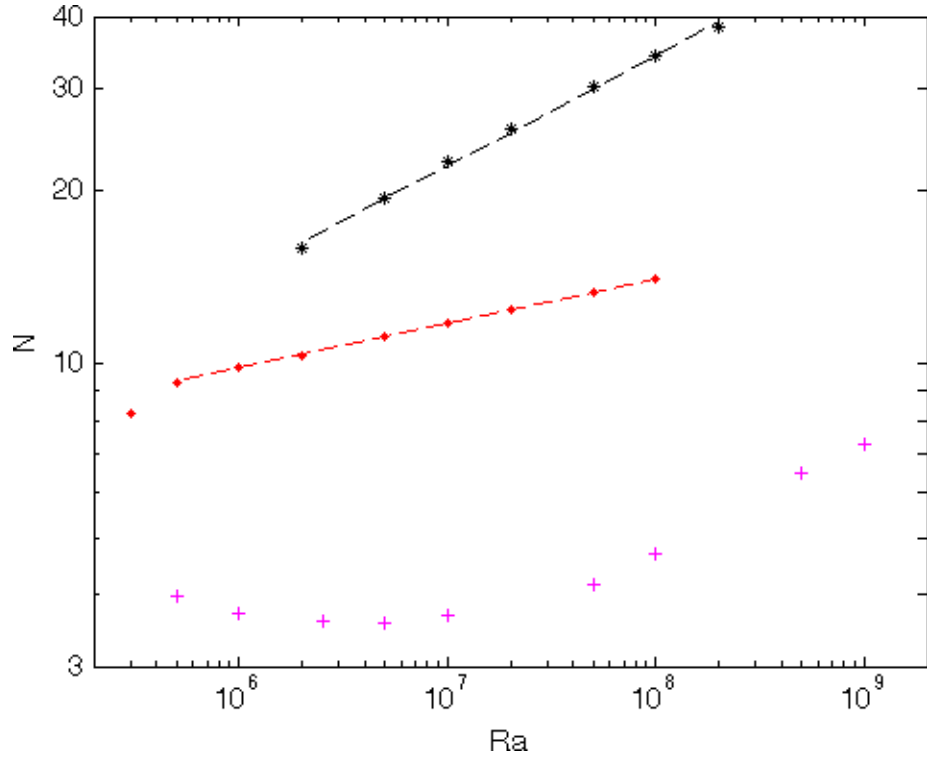


Figure 5.9: Mean Nusselt numbers, N , of convection with zonal flow at various Rayleigh numbers for $A = 2$ and three different Prandtl numbers: $\sigma = 1$ (+), $\sigma = 3$ (●), and $\sigma = 10$ (*). All solutions are chaotic. Dashed lines show algebraic fits for $\sigma = 3$ and $\sigma = 10$, which are $N \sim 3.4 Ra^{0.077}$ and $N \sim 1.0 Ra^{0.19}$, respectively. The same $\sigma = 10$ data appear in Figure 5.1 alongside analogous results for solutions without zonal flow. The last four $\sigma = 1$ data points are unpublished results of H. Johnston (see Appendix C). Corresponding values of f_w for the two larger Prandtl numbers appear in Figure 5.10.

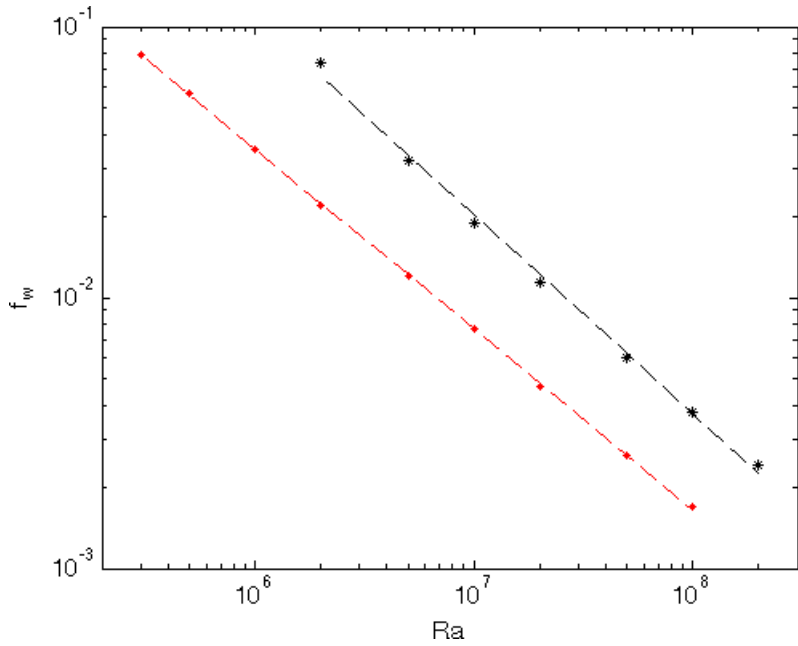


Figure 5.10: Mean fractions of kinetic energy due to vertical motion, f_w , for chaotic convection with zonal flow at various Rayleigh numbers for $A = 2$ and two different Prandtl numbers: $\sigma = 3$ (•) and $\sigma = 10$ (*). Dashed lines show algebraic fits, which are $f_w \sim 341 Ra^{-0.66}$ and $f_w \sim 2721 Ra^{-0.73}$, respectively. Values of N for these same flows appear in Figure 5.9. Values of f_w for $\sigma = 1$ are not given because we lack these data at large Ra .

flows for which N increases as Ra is raised. When chaos sets in, however, raising Ra initially causes N to *decrease*, as in the first four $\sigma = 1$ data points of Figure 5.9. In this range of Ra , the static state is more linearly unstable when Ra is larger, yet less heat is transported when this instability saturates. Such behavior is very unusual in convection, and we know of no precedent. The Nusselt number begins to increase with the Rayleigh number once Ra exceeds roughly $5 \cdot 10^6$, but N is still relatively small. When $Ra = 10^9$, for instance, the Nusselt number is only 7.3, whereas changing the boundary conditions to no-slip causes the mean zonal flow to vanish and raises the Nusselt number to nearly 50 (Johnston and Doering, 2009). (Zonal flow can, however, be sustained with no-slip boundaries at other parameter values, such as when we keep $R = 10^9$ and $\sigma = 1$ but decrease A to 1.4.)

Many arguments have been constructed to explain the observed scalings of $N(Ra, \sigma)$ in ordinary (non-shearing) RB convection at large Rayleigh numbers ([Grossmann and Lohse, 2000](#)). Naively applied to shearing convection, none of these arguments predicts growth of N with Ra as slow as we observe. The arguments fail because they do not address the statistical equilibrium between buoyancy-driven fluctuations and the zonal flow. The basic physics of this equilibrium is clear: when the zonal flow is too strong, it suppresses the fluctuations that drive it and then weakens; when the zonal flow is too weak, the fluctuations grow and strengthen it. The arguments we seek — so far without success — must address the equilibrium strengths of the zonal flow and the fluctuations and predict how this equilibrium is affected by the control parameters.

5.5 Conclusions

This Chapter and the two before it have explored shearing convection (that is, convection with zonal flow). In the two-dimensional configuration we study, the onset of zonal flow appears to be inevitable as the Rayleigh number is raised, and we have examined how this onset is affected by the Prandtl number and horizontal period of the flow. Our exploration of fairly wide horizontal periods differs from prior studies (such as [Howard and Krishnamurti, 1986](#); [Rucklidge and Matthews, 1996](#); [Garcia et al., 2006a](#)), whose results apply to narrower periods than RB convection dynamically selects. At small Prandtl numbers, zonal flow initially sets in steadily, and we have studied this transition by computing steady states in Chapters 3 and 4. We have seen in this Chapter that zonal flow sets in unsteadily at larger Prandtl numbers. In either case, the onset is subcritical, which is not captured by studies that impose artificially narrow periodicity.

Beyond the onset of zonal flow, we have examined how changing the Rayleigh and Prandtl numbers affects such shearing convection. The simulations described in this Chapter reveal

shearing convection to be highly oscillator at moderate σ (such as 1) but much less so at larger σ (such as 10). Vertical profiles of the mean zonal flow vary nearly linearly with height at large Rayleigh numbers, resembling laminar Couette flow. Vertical profiles of mean temperature differ significantly from their counterparts in non-shearing convection, primarily in that the interior temperature remains unstably stratified at large Ra , indicating that conduction, as well as convection, contributes to the net heat transport across the interior. The dispersion of thermal plumes by sheared zonal flow is responsible for the relatively weak convective transport across the interior.

Zonal flows suppress heat transport for all parameters we have explored, both in the steady convection of Chapter 3 and the unsteady convection of the present Chapter. When shearing and non-shearing flows coexist at the same parameters, the Nusselt number of the shearing flow is invariably smaller. At large Rayleigh numbers where only shearing convection is possible, the growth rates of $N(Ra)$ that we have found for σ between 1 and 10 are slower than the slowest rates expected in non-shearing RB convection ([Grossmann and Lohse, 2000](#)). In the oscillatory shearing convection that occurs when $\sigma = 1$, there is even a decade of Ra over which raising Ra makes N smaller. The greater suppression of heat transport at smaller σ is accomplished by zonal flows that make up an even larger fraction of the flow's kinetic energy.

The suppression of convective heat transport by zonal flow is well known, but there has not been much work on quantitatively predicting the extent of this suppression, at least in the context of our two-dimensional RB system. Much as the quest to understand the parameter-dependence of N in typical RB convection has led to a better general understanding of boundary-driven convection, we anticipate that the quest to understand N in strongly shearing convection will lead to a better understanding of how convective structures can interact with mean flows that they themselves drive. We have taken a step in this direction by computing the Nusselt number systematically in a portion of parameter space.

Constructing scaling arguments that explain, or are at least consistent with, our findings remains an open challenge.

Part II

Convection driven by internal heating

Chapter 6

Penetrative convection driven by uniform internal heating¹

6.1 Introduction

Convection can be driven in a horizontal layer of fluid by the thermal boundary conditions, by internal heat sources, or by a combination of both. Standard RB convection, which we studied in Part I, is sustained by keeping the bottom boundary fixed at a higher temperature than the top boundary. In this Part, we focus on convection driven solely by internal heating. Such flows have received much less attention than RB convection, though they play a fundamental role in several geophysical, astrophysical, and industrial processes.

Two simple configurations stand out in the literature on internally heated layers. The heating is constant and uniform in both configurations, but one is insulated below with the top boundary temperature fixed, while in the other the top and bottom boundary temperatures are fixed and equal to one another. We present 2D numerical findings for the latter case, which is the more challenging one due to the presence of a stably stratified bottom boundary layer. The convection in this case is penetrative, in the sense that the unstable

¹An account of the work in this Chapter is published in [Goluskin and Spiegel \(2012\)](#).

stratification near the top boundary drives fluid motion that penetrates into the stably stratified region near the bottom boundary. We focus on both the qualitative nature of the flow and on certain significant integral quantities at large rates of internal heating (that is, at high Rayleigh numbers). The 1985 review of [Kulacki and Richards \(1985\)](#) discusses theoretical, experimental, and numerical efforts on both configurations, and the 1987 review of [Cheung and Chawla \(1987\)](#) contains some general discussion of internally heated convection, though it deals primarily with the insulating-bottom case. We mention below some more recent works of relevance to our present equal-boundary-temperature configuration.

In several physical experiments during the nineteen-seventies ([Kulacki and Goldstein, 1972, 1974; Jahn and Reineke, 1974](#)), convection was studied in fluid layers heated internally by electric currents and with the top and bottom boundary temperatures kept as close to equal as possible. A more recent experiment used periodically distributed heaters in air ([Lee et al., 2007](#)), and 2D ([Jahn and Reineke, 1974](#)) and 3D ([Wörner et al., 1997](#)) simulations have been performed. Some related configurations have also been simulated to study accident scenarios in nuclear reactor engineering ([Nougaliev et al., 1997; Grötzbach and Wörner, 1999; Horvat et al., 2001; Liu et al., 2006; Chen and Krafczyk, 2009](#)). However, such studies often employ geometries and boundary conditions that are motivated by particular applications and from which it is hard to draw conclusions about the basic plane layer problem. They also often resort to turbulence models to simulate the highly turbulent flows that can occur in a nuclear melt. Herein, we return to the plane layer setup and attack it with direct numerical simulations.

Geophysics offers natural occurrences of convection driven by a combination of internal heating and boundary effects. In the Earth's mantle, convection is sustained both by radiogenic heating throughout the mantle itself and by conduction from the underlying hot outer core ([Sotin and Labrosse, 1999; Travis and Olson, 1994; Houseman, 1988](#)). In the upper atmosphere, convection is driven by radiative cooling throughout and by heating from the

lower atmosphere and the surface of the earth ([Ber lengiero et al., 2012](#)). (With a change of variables, this is identical to fluid heated internally and cooled from above.) We anticipate that further results on internally driven convection will supplement the abundant prior results on boundary-driven convection in helping to understand the essential features of such dually driven flows.

Astrophysics provides instances of internally driven convection that is both compressible and nonuniformly heated. In the cores of stars on the main sequence, heat is produced by thermonuclear reactions. In the most massive of such stars, the heating rate is very sensitive to temperature, and this sensitivity creates steep thermal gradients that drive powerful convection in the cores ([Kippenhahn and Weigert, 1994](#)). Clearly, this and many other instances of internally driven convection contain more complications than we confront here. Nonetheless, our findings on uniform heating allow comparison with laboratory experiments, and they may help elucidate the physics of the more involved applications.

The diverse instances of internally heated convection display a great range of Prandtl numbers, from the extremely low effective Prandtl numbers of astrophysical plasmas to the essentially infinite values in the mantle. Prandtl numbers at the lower end of this range are prohibitively expensive to simulate at large Rayleigh numbers, but we have made some effort to study the role of Prandtl number by simulating values between 0.01 and 100. Values near the bottom of this range arise in reactor engineering ([Arcidiacono and Ciofalo, 2001](#)), and the top of this range is, by most measures, near the infinite-Prandtl number limit that mantle studies invariably adopt.

The next section introduces the model to be studied. Section 6.3 describes the qualitative results of our 2D simulations. In section 6.4 we discuss key integral quantities, while in section 6.5 we present our simulation results on these quantities, along with phenomenological scaling arguments. Concluding remarks are given in section 6.6.

6.2 Governing equations

Our nondimensionalization is typical for internally heated convection and goes back at least to Roberts (1967). As is standard in the study of RB convection (Chandrasekhar, 1981), we nondimensionalize length by the domain height, d , and time by the characteristic thermal time, d^2/κ , where κ is thermal diffusivity. The dimensionless spatial domain is thus bounded horizontally by $0 \leq x \leq A$ and vertically by $-1/2 \leq z \leq 1/2$, where A is the aspect ratio. In boundary-driven convective flows, such as RB convection, the boundary conditions provide a temperature scale. Our boundary conditions provide no such scale, so we instead make use of H , the product of the volumetric heating rate and the heat capacity. We nondimensionalize temperature by d^2H/κ , which is the increase in temperature that an insulated parcel of fluid would undergo in one unit of conductive time. The dimensionless equations of motion in the Boussinesq approximation² are then

$$\nabla \cdot \mathbf{u} = 0 \quad (6.1)$$

$$\partial_t \mathbf{u} + \mathbf{u} \cdot \nabla \mathbf{u} = -\nabla p + \sigma \nabla^2 \mathbf{u} + \sigma R T \hat{\mathbf{z}} \quad (6.2)$$

$$\partial_t T + \mathbf{u} \cdot \nabla T = \nabla^2 T + 1. \quad (6.3)$$

The two dimensionless parameters are a Rayleigh number, R , that differs from the usual RB definition given in (1.11), and the standard Prandtl number, σ ,

$$R = \frac{g \alpha d^5 H}{\kappa^2 \nu} \quad (6.4)$$

$$\sigma = \frac{\nu}{\kappa}, \quad (6.5)$$

²Strictly speaking, this is not the standard Boussinesq approximation discussed in Chapter 1 because the symmetry $(z, T) \mapsto (-z, -T)$ is absent.

where ν is kinematic viscosity, g is gravitational acceleration in the $-\hat{\mathbf{z}}$ direction, and α is the linear coefficient of thermal expansion. The parameter R is a *control* Rayleigh number, as defined in section 1.2.2, since it can be defined in terms of the temperature of the static state. A *diagnostic* Rayleigh number, $Ra := \langle T \rangle R$, will be useful in the analysis of section 6.5.4.

6.2.1 Boundary conditions

We impose no-slip and fixed-temperature conditions at the top and bottom boundaries,

$$\mathbf{u} = T = 0 \text{ at } z = \pm\frac{1}{2}, \quad (6.6)$$

where the governing equations' invariance under a uniform shift in temperature allows us to choose boundary temperatures of zero for convenience. These same boundary conditions have been employed in several experiments (as summarized by [Kulacki and Richards, 1985](#)) and in the variational computation of a lower bound on the mean temperature ([Lu et al., 2004](#)). The equality of the top and bottom boundary temperatures ensures that the volume-averaged vertical heat transport by conduction is zero at all times, though, as we shall see, convection transports heat upward on average.

Our simulations employ periodic side boundaries. However, the integral relations of section 6.4 below hold also for boundaries that are stress-free and insulating, as well as on 3D domains with analogous boundary conditions. The choice of side boundaries should not affect mean quantities in the infinite-aspect-ratio limit that we strive to approximate in our simulations.

6.2.2 Conductive solution

The simplest solution to the governing equations is the conductive solution, which is defined by motionless fluid and a horizontally uniform, vertically parabolic temperature profile that we denote by \tilde{T} ,

$$\tilde{T}(z) = \frac{1}{2} \left(\frac{1}{4} - z^2 \right). \quad (6.7)$$

In the conductive state, heat flows outward across the top and bottom boundaries at equal rates. Analyzing \tilde{T} by standard energy stability methods (Joseph, 1976), we find that $R < 26,927$ suffices to guarantee that \tilde{T} is the unique stable solution on a horizontally infinite domain, and any perturbations decay exponentially. Otherwise, the conductive solution is unstable to infinitesimal perturbations of horizontal wavenumber 4.00 when $R > R_L = 37,325$ and the domain admits the wavenumber (Sparrow et al., 1963; Kulacki and Goldstein, 1975). This value of R_L is corroborated by our simulations of (6.1)-(6.3). Transient growth likely occurs between R_E and R_L . We have not observed sustained convection in simulations at any subcritical Rayleigh numbers, but this possibility could be better explored by performing amplitude expansions near R_L .

6.3 Qualitative results

The equations of motion were simulated in 2D using the nek5000 spectral element code (Fisher et al., 2013) on computational domains wide enough to approximate certain bulk properties of a horizontally infinite domain. Details on convergence criteria for meshes, time-averages, and aspect ratios appear in D.2. Visualizations were created using VisIt (Childs et al., 2011).

6.3.1 Steady rolls

Once R exceeds R_L , the critical value for linear instability, pairs of steady rolls form, as illustrated in Figure 6.1. These rolls lack the up-down symmetry of RB rolls. This asymmetry has been noted in previous studies, such as [Kulacki and Goldstein \(1972\)](#), and its origin is clear: the unstable temperature gradient near the upper boundary drives the flow, while stably stratified fluid near the lower boundary inhibits it. As a result, fluid flows across the top and downward faster than it flows across the bottom and upward. Conservation of mass thus dictates that the down-flow regions are narrower than the up-flow regions, and that the roll centers lie above the midline. The cold top boundary layer thickens in the down-flow regions to form nascent thermal plumes, while the cold bottom boundary layer is much more horizontally uniform. Correspondingly, at larger R , we shall see that numerous well-defined plumes descend from the top boundary layer, while cold fluid leaves the bottom boundary layer only when it is stirred up by the interior flow. Such up-down asymmetry is typical of penetrative convection (as in [Zahn, 1991](#), for instance).

6.3.2 Near-periodicity in time

As the Rayleigh number is raised, the steady roll pairs become increasingly asymmetric until they lose stability. In 2D, time is the only dimension available for the rolls to break symmetry, and indeed the flow begins to oscillate in time for large enough R . At moderate σ and large A , steady rolls are replaced by oscillatory ones well before R reaches $2R_L$, in contrast to 2D RB flow, which remains steady for R hundreds of times larger than R_L . Correspondingly, time-dependence was observed in internally heated experiments for R not much larger than R_L ([Kulacki and Goldstein, 1972](#)).

Every oscillating solution we have observed is of the same type – highly nonlinear relaxation oscillations that are nearly periodic in both time and in the horizontal, but never

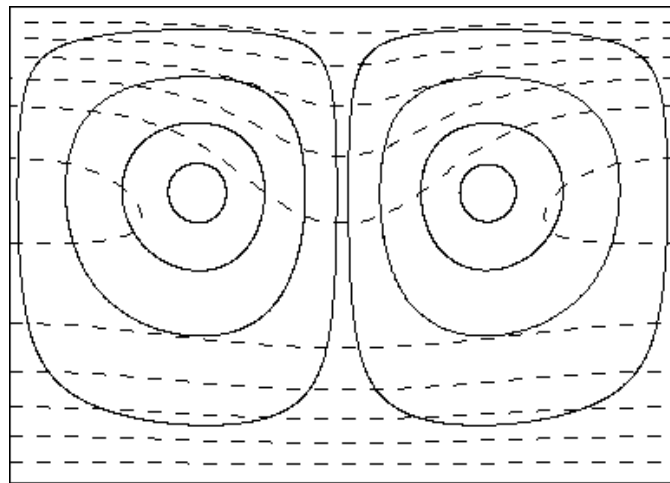


Figure 6.1: Streamlines (solid) and isotherms (dashed) for a pair of stable steady rolls at $R = 50,000$ and $\sigma = 1$. The aspect ratio of $A = 1.4$ is approximately equal to the wavelength that arises naturally in a large 2D domain. The left-hand roll rotates clockwise, while its mirror image rotates counterclockwise. The temperature changes by 0.02 between isotherms, increasing from the zero at the boundaries to 0.12 on the innermost isotherm.

exactly so. At the start of the slow phase, the cold plumes are spaced nearly uniformly. The spacing becomes less uniform as each plume becomes a member of a pair, drifting toward its mate at a gradually accelerating rate. When the two plumes are sufficiently close together, the flow enters the fast phase, which is depicted in Figure 6.2. In this phase, plumes quickly collide and merge. But even as the number of plumes is being halved, new plumes are already forming in each gap, restoring the original number and restarting the slow phase. Qualitatively similar merging and genesis of plumes has been seen in 3D simulations ([Wörner et al., 1997](#)) and laboratory experiments ([Kulacki and Goldstein, 1972](#)), though the nearly periodic and spatially synchronized relaxation oscillations we observe have not been reported previously.

The deviation from exact periodicity may or may not be due to numerical inaccuracies. It is possible that the underlying solutions are in fact stable, exactly periodic relaxation oscillations, but that numerical noise always significantly perturbs the oscillations when time derivatives are very small during the slow phase. Alternately, we may be observing chaotic

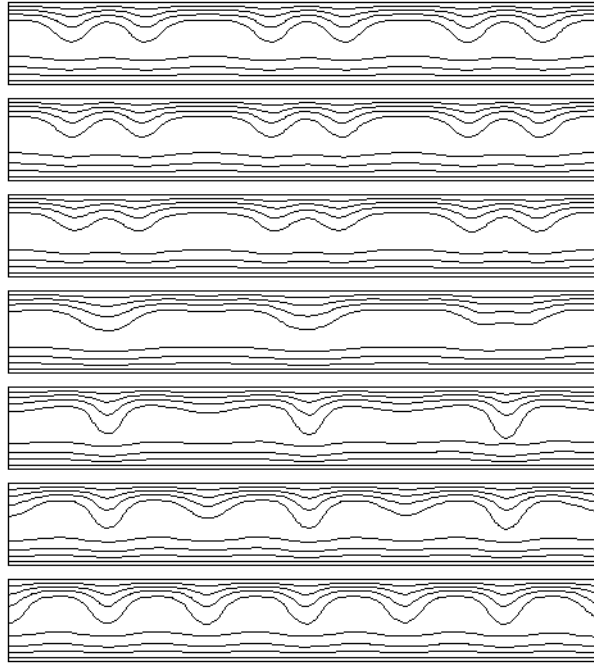


Figure 6.2: Temperature isotherms for a series of time slices depicting the fast phase of an oscillation at $R = 65,000$ and $\sigma = 1$, cropped to an aspect ratio of 8 from simulations with $A = 12$. The temperature changes by 0.025 between isotherms, increasing from zero at the boundaries to 0.1 on the two central isotherms. The merging and genesis of cold thermal plumes is evident, going forward in time from top to bottom with time steps of 0.15. By contrast, the slow phases of the oscillations have periods on the order of 100.

oscillations. These possibilities invite a more detailed study of the system's bifurcation structure.

6.3.3 Toward turbulence

The Rayleigh number ranges over which spatially synchronized oscillations have been observed are all rather narrow, the change in R over such ranges being always much smaller than R_L . When R is above these ranges, plumes continue to grow from the top boundary layer and merge with others, but these events are no longer synchronized across the spatial domain, and the flow is no longer nearly periodic in time. The flow becomes visibly more irregular as the Rayleigh number is raised further, but because the flow is constrained to 2D,

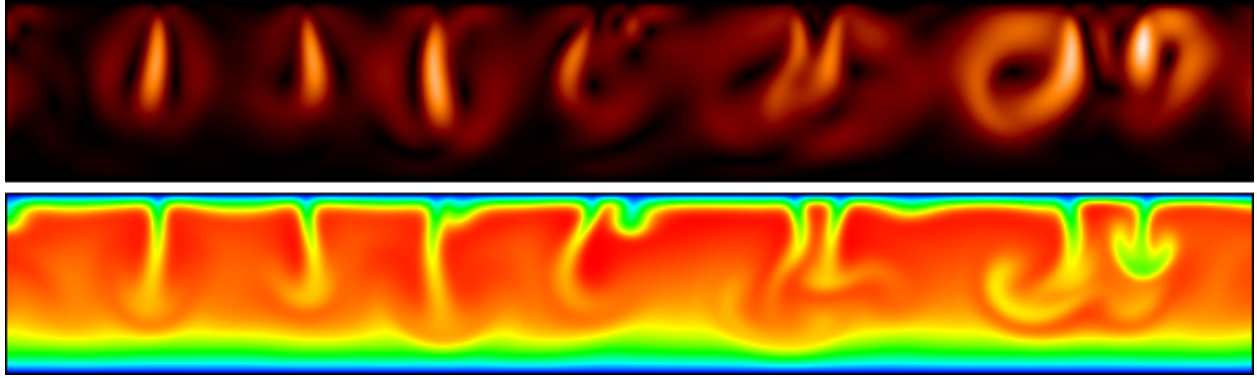


Figure 6.3: Instantaneous fluid speed (top) and temperature (bottom) at $R = 10^7$ and $\sigma = 5$. The faster-moving fluid is lighter in the speed field. The hottest fluid is red in the temperature field, and the coldest is blue.

solutions always exhibit some roll-like coherence. In 3D, on the other hand, rolls will quickly lose stability to three-dimensional structures ([Kulacki and Goldstein, 1972](#)). Nonetheless, we regard the 2D system as interesting in its own right, and for moderate-to-high σ , the 2D version is apparently a good predictor of the 3D system’s integral quantities ([Schmalzl et al., 2004](#)).

As R is increased into the millions, flows at moderate-to-high σ exhibit mushroom-like cold plumes descending from the top boundary layer. (Such structures are familiar from the study of RB convection, along with their hot counterparts that rise from the bottom boundary layer. See [Zocchi et al., 1990](#), for example). For $\sigma = 5$, Figure 6.3 shows typical fluid speed and temperature fields at $R = 10^7$, and Figure 6.4 shows temperature fields up to $R = 10^{10}$, by which point we are beginning to see the eddies and filaments characteristic of 2D turbulence. (These and subsequent visualizations have aspect ratios of 7 but are cropped from simulations of larger A .) In the fluid speed and temperature fields of Figure 6.3, strong down-flow evidently aligns with thermal plumes, while weaker recirculation occurs in between plumes. Though not shown, circulation is similarly aligned with clusters of plumes in the higher- R cases of Figure 6.4.

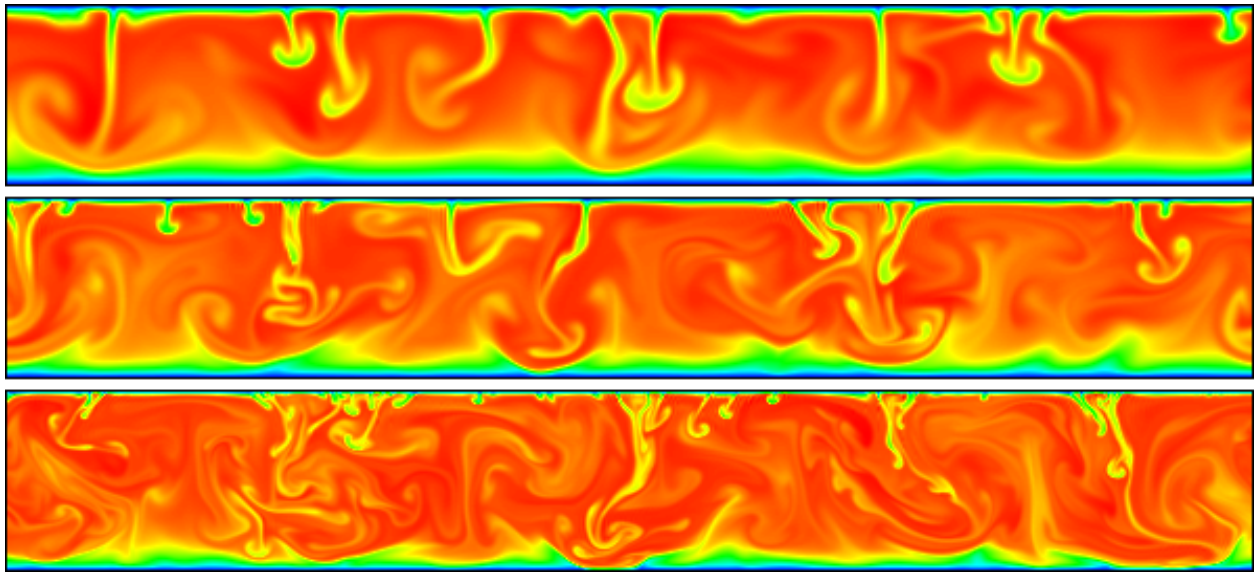


Figure 6.4: Instantaneous temperature fields for Rayleigh numbers of 10^8 (top), 10^9 , and 10^{10} with $\sigma = 5$. The hottest fluid in each image is red, and the coldest is blue, though the color scales are normalized differently in each image.

The thermal plumes change in several ways as R is increased. Individual plumes become smaller because they scale with the upper thermal boundary layer, which thins as R is raised. Meanwhile, they also become more numerous, and they show an increasing tendency to merge with nearby plumes. At large R , most individual plumes merge with others to become part of larger composite plumes, as in the $R = 10^9$ and $R = 10^{10}$ fields of Figure 6.4. Unlike the small individual plumes, these composite plumes are able to penetrate to the bottom thermal boundary layer, driving roll-like structures whose heights and widths are comparable to the height of the domain. The scale of the composite plumes is maintained because the number of their constituent plumes increases as the constituent plumes themselves shrink. In 3D RB simulations, plumes similarly cluster to form larger structures whose horizontal scale varies only weakly with the Rayleigh number (von Hardenberg et al., 2008). The increasingly strong composite plumes visible in Figure 6.4 also drive increasingly powerful and disordered interior flow, which at large R begins to stir up cold fluid from the bottom boundary layer.

Cold ejections from the bottom boundary layer are evident at $R = 10^9$ and quite pronounced at $R = 10^{10}$.

6.3.4 Low Prandtl numbers

Flows of low Prandtl number differ significantly from those of moderate-to-high Prandtl number, most notably in the decrease of up-down asymmetry at a given R and in the appearance of so-called flywheels, which have been studied in low- σ RB convection ([Moore and Weiss, 1973](#); [Proctor, 1977](#); [Clever and Busse, 1981](#)). Figure 6.5 shows typical low- σ fluid speed and temperature fields at two Rayleigh numbers. In the $R = 2 \cdot 10^5$ speed field, two flywheels are evident in the right half of the domain. Each flywheel was part of a pair of rolls until it subsumed its mate and became more axisymmetric. Eventually, such a flywheel loses momentum and becomes part of a pair again, but new ones come into existence repeatedly. In the $R = 10^7$ field, flywheels dominate the flow, and the hottest fluid is found solely in their centers, rather than being distributed throughout the interior, as it is in the $\sigma = 5$ field for the same R that is shown in Figure 6.3. We simulated Prandtl numbers only as low as 0.01 since computation becomes increasingly expensive as σ is lowered beyond unity. This is because the thinning kinetic boundary layers require finer spatial meshes, and the slower advective dynamics require longer dimensionless times for spatiotemporal averages to converge. To access very small σ at large R , one might instead simulate the small- σ limit of the Boussinesq equations ([Spiegel, 1962](#); [Thual, 1992](#)).

6.4 Integral quantities

We shall focus on the volume averages of temperature, $\langle T \rangle$, and vertical convective heat flux, $\langle wT \rangle$, where $\mathbf{u} = (u, w)$. We will see that $\langle T \rangle$ behaves like the inverse Nusselt number, while

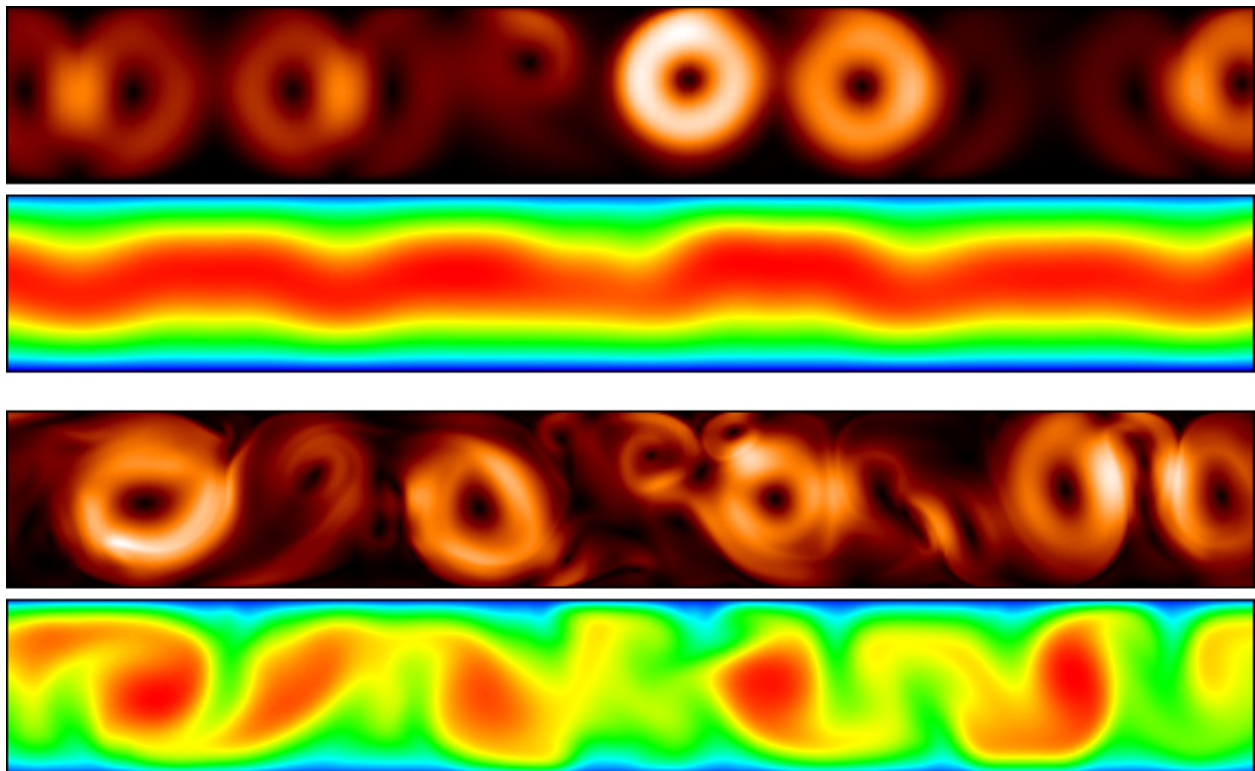


Figure 6.5: Instantaneous fluid speeds (above) and temperatures (below) at $\sigma = 0.01$ with $R = 2 \cdot 10^5$ (top pair) and $R = 10^7$ (bottom pair). The faster-moving fluid is lighter in the speed fields. The hottest fluid is red in the temperature fields, and the coldest is blue.

$\langle wT \rangle$ is without analogue in RB convection. To gain some understanding of the vertical structure of the flow, we will also consider horizontally averaged temperature profiles, $\bar{T}(z)$.

6.4.1 Vertical heat fluxes

The volume-averaged vertical conductive heat transport vanishes at all times. (Recall from section 1.2.4 that this quantity is proportional to the temperature difference between the boundaries.) Thus, any difference between the outward heat fluxes across the top and bottom boundaries is due solely to the mean convective transport, $\langle wT \rangle$, which may be thought of as the up-down asymmetry in vertical heat transport induced by fluid motion. Of course, convective and conductive processes are entwined in the details of the flow, and sustained fluid motion requires nonzero temperature gradients, so although vertical conduction vanishes in the mean, it is locally essential.

To quantitatively relate $\langle wT \rangle$ to the boundary fluxes, we first note that the mean outward heat flux across the top boundary is $-\bar{T}'_T$, and that across the bottom boundary is \bar{T}'_B , where the primes denote d/dz , and the subscripts denote evaluation at the top and bottom boundaries, respectively. These fluxes must always combine to equal the rate of heat production, which is normalized to unity, as is verified by integrating (6.3) to yield³

$$\bar{T}'_B - \bar{T}'_T = 1. \quad (6.8)$$

In the conductive solution, both of the mean outward heat fluxes across the boundaries, $-\bar{T}'_T$ and \bar{T}'_B , have a value of $1/2$, but a nonzero $\langle wT \rangle$ breaks this symmetry. Integrating $z \cdot (6.3)$ reveals that $\langle wT \rangle$ is equal to half of the difference between the heat flowing out the

³Spatiotemporal averages of time derivatives over infinite time vanish from all integral relations we give here because, as follows from the analysis of Lu et al. (2004), the volume averages of $|\mathbf{u}|$ and $|T|$ are bounded uniformly in time.

top boundary and the heat flowing out the bottom one,

$$\langle wT \rangle = -\frac{1}{2}(\bar{T}'_T + \bar{T}'_B). \quad (6.9)$$

Combining (6.8) and (6.9), we see that the (dimensionless) mean outward heat flux across the top boundary is $1/2 + \langle wT \rangle$, while the outward flux across the bottom boundary is $1/2 - \langle wT \rangle$. Since their sum is normalized to unity, these dimensionless fluxes also equal the fractions of the total produced heat that leave the domain via the top and bottom boundaries.

The mean vertical heat flux is bounded according to

$$0 \leq \langle wT \rangle \leq 1/2, \quad (6.10)$$

as proven in Appendix D.1.3. The lower bound, which corresponds to equal heat fluxes out of the top and bottom boundaries, is fulfilled only by the conductive solution. The upper bound corresponds to the maximally asymmetric case in which all heat flows out the top (that is, $-\bar{T}'_T = 1$ and $\bar{T}'_B = 0$). The nonnegativity of $\langle wT \rangle$ means that the onset of fluid motion can only increase heat flux across the top boundary and decrease heat flux across the bottom boundary. Physically, this is because fluid near the upper boundary has an adverse (negative) temperature gradient and drives the flow by sending relatively dense, cold fluid downward, while fluid near the lower boundary has a stabilizing (positive) temperature gradient and less readily sends cold fluid upward into the interior. Although $\langle wT \rangle$ is the quantity that arises naturally in integral relations, one may prefer to think in terms of the mean fraction of heat flowing out the top boundary, $1/2 + \langle wT \rangle$, which lies between $1/2$ and 1 .

The horizontally averaged convective and conductive fluxes can be related by averaging (6.3) over $(0, A) \times (-1/2, z)$ and time to find (Lu et al., 2004)

$$\overline{wT}(z) = \overline{T}'(z) - \overline{T}'_B + 1/2 + z, \quad (6.11)$$

which is why we need not examine $\overline{wT}(z)$ profiles in addition to $\overline{T}(z)$. Averaging the vertical heat current, $-\partial_z T + wT$, over the horizontal and time, and applying (6.11), (6.8), and (6.9), yields $\langle wT \rangle + z$. That is, the mean heat flux across a horizontal surface increases linearly with height (because of the uniform volumetric heating) and is fully determined by the volume-integrated heat flux.

6.4.2 Mean temperature

While $\langle wT \rangle$ conveys the difference in outward heat transport across the top and bottom boundaries, the mean fluid temperature, $\langle T \rangle$, conveys the relative amounts of convective and conductive transport responsible for carrying heat outward to the boundaries. To see this, we imagine the layer is divided along a plane where $\overline{T}(z) = \overline{T}_{max}$. A sensible value for the outward conductive heat flux is obtained by adding the magnitudes of (volume-averaged) upward conduction in the upper layer and downward conduction in the lower layer, which yields $2\overline{T}_{max}$. When R becomes large, powerful fluid motion homogenizes the interior temperature, so that $\overline{T}_{max} \sim \langle T \rangle$. Thus, at a given large R , a lower value of $\langle T \rangle$ means that a higher fraction of the outward heat transport is achieved by convection, as opposed to conduction.

The dimensionless temperature is bounded according to

$$0 < \langle T \rangle \leq 1/12, \quad (6.12)$$

as proven in Appendix D.1.2, though tighter R -dependent lower bounds exist (Lu et al., 2004; Whitehead and Doering, 2011) and are stated in section 6.5.3 below. The upper bound is saturated by the conductive solution, and $\langle T \rangle$ typically decreases with increasing R . This decrease may seem counter-intuitive until one recalls that the dimensionless T is normalized by the rate of heat production. If the rate of heat production is doubled, which doubles R , the dimensionful temperature of the layer will indeed increase, though it will not quite double. These diminishing returns are evinced by the decrease in dimensionless temperature.

6.4.3 Power integrals

Integrating $T \cdot (6.3)$ and $\mathbf{u} \cdot (6.2)$, respectively, yields (Catton and Suo-Anttila, 1974)

$$\langle T \rangle = \langle |\nabla T|^2 \rangle \quad (6.13)$$

$$R\langle wT \rangle = \langle |\nabla \mathbf{u}|^2 \rangle. \quad (6.14)$$

These relations correspond to the power integrals of RB convection (Malkus, 1954; Howard, 1963). The RB power integrals serve as constraints for variational proofs of upper bounds on the Nusselt number (Howard, 1972; Constantin and Doering, 1996), as well as forming a basis for scaling arguments (Grossmann and Lohse, 2000). As we argue in the next section, $\langle T \rangle$ behaves like an inverse Nusselt number, and indeed (6.13) and (6.14) enable both scaling arguments (*cf.* section 6.5.4) and variational lower bounds (Lu et al., 2004; Whitehead and Doering, 2011) for $\langle T \rangle$.

6.4.4 Dimensionless numbers

The dimensionless quantities $\langle T \rangle$ and $\langle wT \rangle$ are natural choices for characterizing the mean vertical heat flux, in part because they arise in the power integrals (6.13) and (6.14), yet

neither of these quantities behaves like the Nusselt number of RB convection. The RB Nusselt number is bounded below and grows unboundedly with increasing Rayleigh number, whereas $\langle T \rangle$ and $\langle wT \rangle$ are bounded above and below. However, it is possible in the present case to define dimensionless quantities in place of $\langle T \rangle$ and $\langle wT \rangle$ that behave more like Nusselt numbers, and prior studies have done just that.

At large R , $\langle T \rangle$ is a sort of inverse Nusselt number, for the following reason. We have defined the RB Nusselt number in section 1.2.5 as the total vertical heat flux, divided by the conductive vertical heat flux, both averaged over the entire flow. This quantity would not be finite in our present configuration since the conductive flux over the full layer vanishes. However, a useful volume-integrated conductive flux is recovered by considering only *outward* flux. As discussed in section 6.4.2, the outward conductive flux scales like $\langle T \rangle$ at large R . The total outward flux is unity, so an outward N can be defined proportionally to $1/\langle T \rangle$. We simply focus on $\langle T \rangle$, but some intuition can be borrowed from the RB case by realizing that $1/\langle T \rangle$ behaves like a Nusselt number. On the other hand, it seems impossible to define a Nusselt number-like quantity in terms of $\langle wT \rangle$ alone.

Instead of using $\langle T \rangle$ and $\langle wT \rangle$, most previous studies of our configuration have characterized the bulk heat flow by two dimensionless quantities that are often called top and bottom Nusselt numbers (such studies are summarized in Figure 18 and Table 5 of [Kulacki and Richards, 1985](#)). These quantities, which we denote by N_T and N_B , use boundary fluxes for their numerators instead of volume averages. The respective numerators of N_T and N_B are the outward heat fluxes across the top and bottom boundaries, $1/2 + \langle wT \rangle$ and $1/2 - \langle wT \rangle$, while the denominator of each is \bar{T}_{max} . Since $\bar{T}_{max} \sim \langle T \rangle$ for large R , we can say

$$N_T \sim \frac{1/2 + \langle wT \rangle}{\langle T \rangle} \quad (6.15)$$

$$N_B \sim \frac{1/2 - \langle wT \rangle}{\langle T \rangle}. \quad (6.16)$$

In prior studies, both N_T and N_B have typically been fit to algebraic laws of the form cR^α , as summarized in Table 5 of [Kulacki and Richards \(1985\)](#). However, our numerical results suggest that this is not an appropriate representation at large R , for the following reason. The fraction of heat flowing out the top, $1/2 + \langle wT \rangle$, is between $1/2$ and 1 , so the scaling of N_T with increasing R is simply that of $1/\langle T \rangle$. The expectation that N_B will have a different algebraic scaling implicitly assumes that $1/2 - \langle wT \rangle$ decays toward zero, and at moderate R this seems to be the case. In our large- R numerical results, however, $\langle wT \rangle$ plateaus before reaching $1/2$, so the scaling of N_B becomes that of $1/\langle T \rangle$ as well. Thus, concentrating on the scalings of N_T and N_B becomes rather redundant at large R . Furthermore, the asymmetry between upward and downward heat flux is more clearly conveyed by $\langle wT \rangle$. We therefore prefer to focus on $\langle T \rangle$ and $\langle wT \rangle$ instead of N_T and N_B , though either pair of values may be approximately computed from the other according to (6.15) and (6.16).

6.5 Quantitative results

6.5.1 Temperature profiles

Examples of mean vertical temperature profiles, $\bar{T}(z)$, are plotted in Figure 6.6. The onset of fluid motion is accompanied by an upward skewing of $\bar{T}(z)$, an increasingly isothermal interior, and an overall decrease in mean (dimensionless) temperature. By the time R reaches 10^7 , the interior profile is very nearly linear, though a bit sub-isothermal (that is, stably stratified). As in RB convection, if the interior were completely isothermal, plumes would dissipate more slowly and overshoot further, and so restore the sub-isothermal conditions. Since the temperature profiles of Figure 6.6 become visibly more asymmetric as R increases, (6.9) dictates that $\langle wT \rangle$ increases as well, at least for $\sigma = 5$ and this range of R . Our computed values of $\langle wT \rangle$ indeed rise with R in this regime, though not in all regimes.

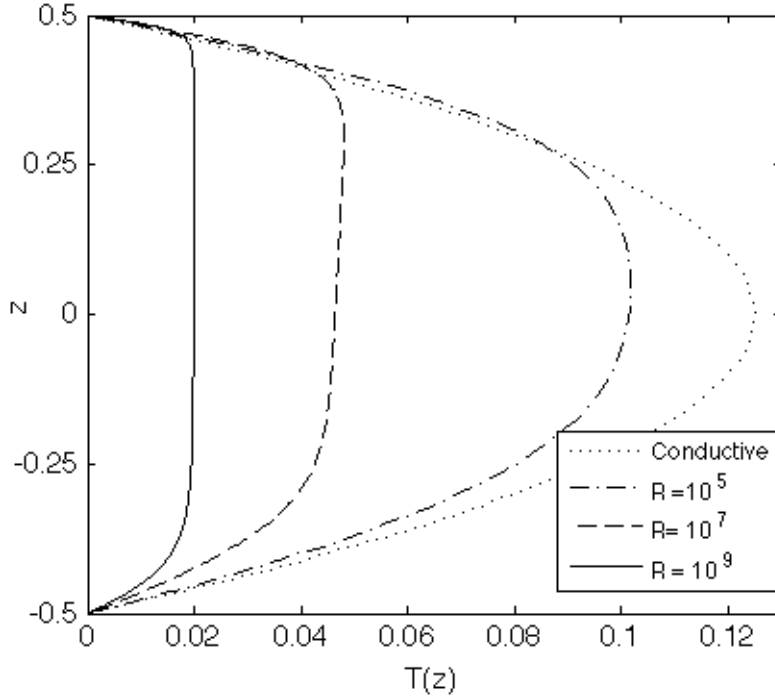


Figure 6.6: Mean temperature profiles, $\bar{T}(z)$, for several R with $\sigma = 5$.

6.5.2 Convective heat flux

Mean convective heat fluxes, $\langle wT \rangle$, are plotted in Figure 6.7 for various R and σ , along with a fit proposed by Kulacki and Goldstein for their experimental data (Kulacki and Goldstein, 1972). Over the R range of their experiments, which employed an aqueous solution with $\sigma \approx 6$, we find reasonable agreement between their fit and our $\sigma = 5$ simulation results. This supports the claim of Schmalzl et al. (2004) that the 2D system can be a good predictor of the 3D system's integral quantities for large enough σ .

While accurate over the range of R in their experiments, the fit of Kulacki and Goldstein, like similar ones proposed for other moderate- R data (Jahn and Reineke, 1974; Wörner et al., 1997), does not capture the behavior of $\langle wT \rangle$ that we observe at higher R . Such fits have

typically been computed in terms of fits to N_T and N_B by

$$\langle wT \rangle + \frac{1}{2} = \frac{N_T}{N_T + N_B} \sim \frac{aR^\alpha}{aR^\alpha + bR^\beta}. \quad (6.17)$$

When applied to moderate- R data, this ansatz will yield a larger growth rate with R for N_T than for N_B (that is, $\alpha > \beta$), resulting in a fit for $\langle wT \rangle$ that asymptotes to 1/2 as $R \rightarrow \infty$. Such fits invariably exceed our computed values of $\langle wT \rangle$ at large R . This arrested growth of $\langle wT \rangle$ is visible in Figure 6.7 at the upper end of our $\sigma = 5$ data, but it occurs at still lower R for smaller σ . To explore the phenomenon further, we have carried the $\sigma = 1$ and $\sigma = 0.5$ simulations to $R = 2 \cdot 10^{10}$ and $R = 2 \cdot 10^9$, respectively.

Once R exceeds roughly 10^9 in our $\sigma = 1$ and $\sigma = 0.5$ simulations, $\langle wT \rangle$ not only stops growing but decreases with increasing R , as seen in Figure 6.7. [This cannot be attributed to spatial under-resolution, which inflates $\langle wT \rangle$ due to under-resolved cold plumes descending farther before being warmed by thermal diffusion. This same effect inflates the Nusselt number in under-resolved simulations of 3D RB convection (Stevens et al., 2010).] The uncertainty in the data of Figure 6.7 is small, but it is still too large to determine whether $\langle wT \rangle$ starts decreasing first for $\sigma = 1$ or for $\sigma = 0.5$. The fact that $\langle wT \rangle$ does not asymptote to 1/2 is also suggested by the superlinearity of $\log N_B$, plotted versus $\log R$, in the 3D simulation results of Wörner et al. (1997), which go up to $R = 10^9$ for $\sigma = 7$.

Competing physical mechanisms seem to be responsible for the initial increase and subsequent decrease of $\langle wT \rangle$ with increasing R . Initially, the cold down-flow from the unstable top boundary layer becomes stronger, as does the upward recirculation of warmer fluid, and this causes $\langle wT \rangle$ to grow. As noted in section 6.3.3, however, the increasingly strong down-flow begins to stir up cold fluid from the bottom boundary layer, which slows and subsequently reverses the growth of $\langle wT \rangle$. Still, since this cold up-flow is ultimately driven by the cold down-flow, it is surprising that the up-flow can strengthen with increasing R faster than the

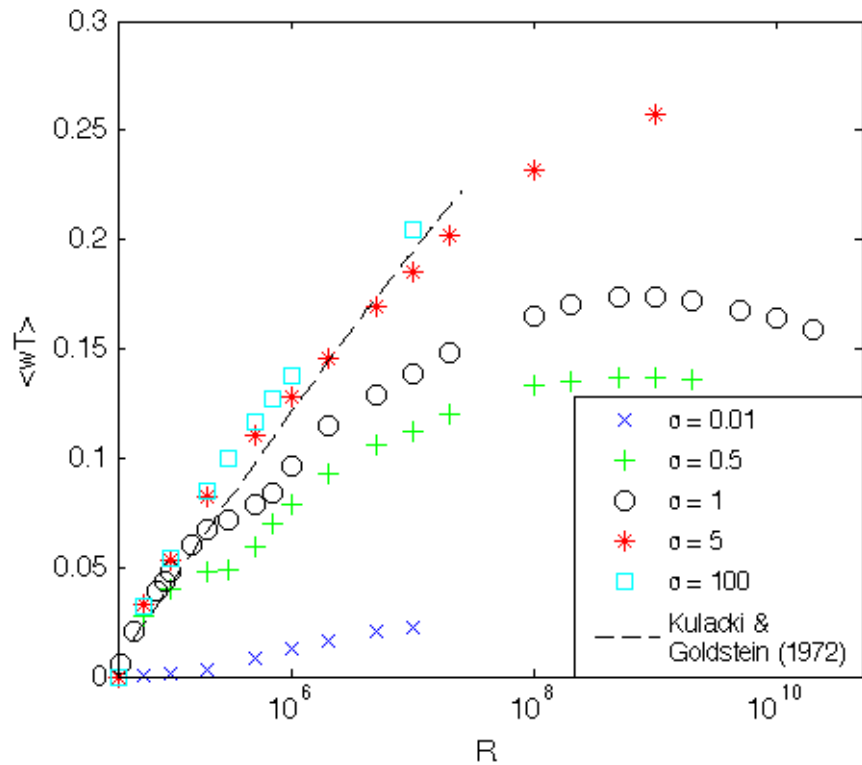


Figure 6.7: Simulation results for mean vertical convective heat flux, $\langle wT \rangle$, beginning with a value of 0 at $R_L = 37,325$. (Adding 1/2 yields the fraction of produced heat flowing outward across the top boundary.) Also shown is the fit given by [Kulacki and Goldstein \(1972\)](#) for their experimental data with $\sigma \approx 6$.

down-flow does, which is necessary to explain the decrease in $\langle wT \rangle$ that we observe at large R .

The ultimate fate of $\langle wT \rangle$ as $R \rightarrow \infty$ remains uncertain. If $\langle wT \rangle \rightarrow 0$ in the limit, meaning that heat ultimately flows equally out of both boundaries, this might be proven by a variational upper bound on $\langle wT \rangle$ that approaches zero in the limit. Such a result has eluded us, however. Whatever the fate of $\langle wT \rangle$, more experimental data would be useful. Our $R = 2 \cdot 10^{10}$ simulation required two days on 256 BG/P processors for $\langle wT \rangle$ to converge. Such 2D numerics could be pushed to somewhat higher R , but perhaps not high enough, and the analogous computations in 3D would be extremely expensive. A physical experiment may be the best option.

6.5.3 Temperature

Mean temperatures, $\langle T \rangle$, are plotted in Figure 6.8 for various R and σ . Evidently, σ has a weaker effect on $\langle T \rangle$ than on $\langle wT \rangle$. The $\sigma = 1$ simulations were carried to high enough R to reveal a nearly algebraic scaling of $\langle T \rangle$ with R , as reflected by a nearly straight line in the log-log plot of Figure 6.8. The data for Prandtl numbers of 0.5 and 5 fall nearly on the same line. The last eight $\sigma = 1$ points are fit well by the law

$$\langle T \rangle = 1.13 R^{-0.200}. \quad (6.18)$$

To three significant figures, the exponent of the fit is $-1/5$, which is one of the values predicted by our scaling arguments in the next section. (Performing the fit with one or two data points removed yields a range of exponents between -0.196 and -0.204 .)

Also shown in Figure 6.8 are the best known variational lower bounds on $\langle T \rangle$, which are consistent with our simulation results, if not tight. At leading order for large R , these bounds are $\langle T \rangle \geq 1.09R^{-1/3}$ for all σ (Lu et al., 2004) and $\langle T \rangle \geq 0.419(R \log R)^{-1/4}$ in the

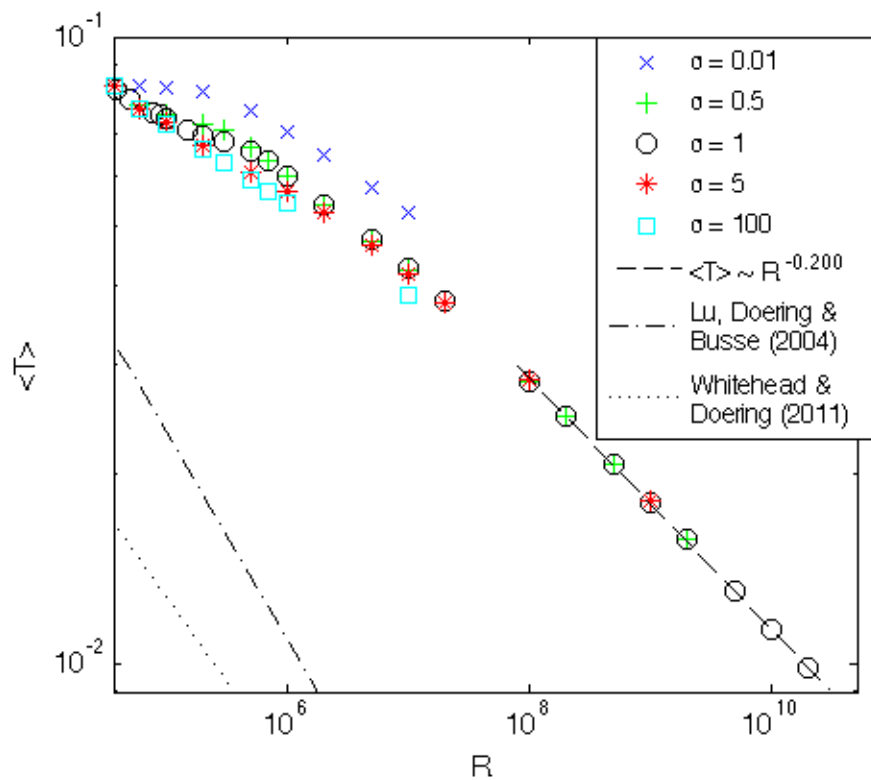


Figure 6.8: Simulation results for mean dimensionless temperature, $\langle T \rangle$, beginning with a value of $1/12$ at $R_L = 37,325$. The algebraic fit (6.18) to the last eight $\sigma = 1$ data points is shown (dashed line), along with the lower bound of Lu et al. (2004) for arbitrary σ (dash-dotted line) and the lower bound of Whitehead and Doering (2011) for infinite σ (dotted line).

infinite- σ limit (Whitehead and Doering, 2011). The bounds were proven by Doering and collaborators using the integral constraints (6.13) and (6.14) in application of the background method. The infinite- σ bound has a smaller prefactor, but it decays more slowly as $R \rightarrow \infty$, so it will ultimately be the tighter bound. This is consistent with the next section's scaling arguments, which suggest that $\langle T \rangle$ decays more slowly in R for larger σ .

All evidence indicates that, for stable, statistically steady solutions, $\langle T \rangle \rightarrow 0$ as $R \rightarrow \infty$. Certainly that is not true for all solutions: the conductive state has a mean temperature of $1/12$ and solves the governing equations for all R , though it is unstable when R is large.⁴ If indeed $\langle T \rangle \rightarrow 0$ for all stable solutions, proving as much may require new analytic machinery for restricting to stable solutions when constructing bounds.

6.5.4 Scaling arguments

Over the past half century, several scaling arguments have been proposed to predict the dependence of Nusselt number on Rayleigh number in RB convection. The approach of Grossmann and Lohse, put forth in Grossmann and Lohse (2000) and subsequent extensions (Grossmann and Lohse, 2001, 2004, 2011), is the most systematic among them, predicting the existence of numerous scaling regimes in the R - σ parameter plane. As discussed in section 6.4.4, our $\langle T \rangle$ is a kind of inverse Nusselt number, so we can apply the Grossmann-Lohse approach of Grossmann and Lohse (2000) in the search for scalings of $\langle T \rangle$. However, since the bulk heat flux in our problem is characterized by two numbers rather than one, the Grossman-Lohse arguments do not yield fully determined scalings; in general we cannot eliminate the unknown quantity $\langle wT \rangle$ from the scalings of $\langle T \rangle$. Obtaining scalings for both $\langle T \rangle$ and $\langle wT \rangle$ in terms of only R and σ would require a theory that addresses both boundary

⁴Similarly, the Nusselt number of RB convection seems to grow unboundedly as $R \rightarrow \infty$ for stable, statistically steady states, while the conductive solution, for which $N = 1$, reminds one that this need not be so for unstable solutions.

Dominant term	Thicker BL	Scaling relation
$\langle \nabla \mathbf{u} ^2 \rangle_{BL}$	either	$R\langle wT \rangle \sim \sigma^2 Re^{5/2}$
$\langle \nabla \mathbf{u} ^2 \rangle_{bulk}$	either	$R\langle wT \rangle \sim \sigma^2 Re^3$
$\langle \nabla T ^2 \rangle_{BL}$	T	$\langle T \rangle \sim \sigma^{-1/2} Re^{-1/2}$
$\langle \nabla T ^2 \rangle_{BL}$	u	$\langle T \rangle \sim \sigma^{-1/3} Re^{-1/2}$
$\langle \nabla T ^2 \rangle_{bulk}$	T	$\langle T \rangle \sim \sigma^{-1} Re^{-1}$
$\langle \nabla T ^2 \rangle_{bulk}$	u	$\langle T \rangle \sim \sigma^{-1/2} Re^{-3/4}$

Table 6.1: Intermediate relations in the Grossmann-Lohse approach, depending on whether dissipations are dominated by the boundary layers or the bulk, and on whether the viscous (u) or thermal (T) upper boundary layer is thicker.

layers, whereas the Grossman-Lohse arguments adapted to the present problem involve only the top one. Nonetheless, we obtain some useful partial results.

As was done in [Grossmann and Lohse \(2000\)](#), we assume that the interior flow is characterized by a single large-scale velocity, given in dimensionless terms by a Reynolds number, Re , interpretations of which are discussed in [Ahlers et al. \(2009\)](#), and we assume that the viscous boundary layer is a laminar one of Blasius type whose thickness scales as $\lambda_u \sim Re^{-1/2}$. (This and subsequent relations are dimensionless.) In our configuration, the temperature gradient of the top thermal boundary layer must remain of order unity since (6.8)-(6.10) imply $1/2 \leq -\bar{T}'_T \leq 1$. Thus, the top thermal boundary layer's thickness must scale as $\lambda_T \sim \langle T \rangle$. The remainder of the argument consists of replacing the thermal dissipation, $\langle |\nabla T|^2 \rangle$, in (6.13) and the viscous dissipation, $\langle |\nabla \mathbf{u}|^2 \rangle$, in (6.14) with scaling approximations. The approximations used depend on whether the dissipations are dominated by contributions from the boundary layers or the bulk, and on whether the viscous or thermal upper boundary layer is thicker. We omit the details of this procedure, as they are analogous to the RB case handled in [Grossmann and Lohse \(2000\)](#), but the six intermediate relations that result are given in Table 6.1. From these six relations one obtains eight scalings of $\langle T \rangle$ and Re in terms of σ and \mathcal{R} , where $\mathcal{R} := R\langle wT \rangle$. (This quantity is unrelated to \mathcal{R} of Chapter 4.) The scalings of $\langle T \rangle$ are reported in Table 6.2.

Dominant $\langle \nabla T ^2 \rangle$	Dominant $\langle \nabla \mathbf{u} ^2 \rangle$	Thicker BL	$\langle T \rangle$ Scaling
BL	BL	T	$\mathcal{R}^{-1/5} \sigma^{-1/10}$
BL	BL	u	$\mathcal{R}^{-1/5} \sigma^{1/15}$
BL	bulk	T	$\mathcal{R}^{-1/6} \sigma^{-1/6}$
BL	bulk	u	$\mathcal{R}^{-1/6}$
bulk	BL	T	$\mathcal{R}^{-2/5} \sigma^{-1/5}$
bulk	BL	u	$\mathcal{R}^{-3/10} \sigma^{1/10}$
bulk	bulk	T	$\mathcal{R}^{-1/3} \sigma^{-1/3}$
bulk	bulk	u	$\mathcal{R}^{-1/4}$

Table 6.2: Scalings of $\langle T \rangle$ with $\mathcal{R} := R\langle wT \rangle$ and σ in eight different regimes, as predicted by arguments of Grossmann-Lohse type.

The simplest way to eliminate $\langle wT \rangle$ from the scaling laws of Table 6.2 is to assume that it remains $O(1)$, so that $\mathcal{R} \sim R$. We cannot justify this in general, but it is visibly true at the upper end of our $\sigma = 1$ simulations, whose $\langle T \rangle$ scaling we would like to explain. In light of this, Table 6.2 suggests that our observed scaling of $\langle T \rangle \sim R^{-1/5}$ should occur when viscous and thermal dissipations are both dominated by their boundary layer contributions. In our high- R simulations, $\langle |\nabla T|^2 \rangle$ is indeed boundary layer-dominated, but the bulk contribution to $\langle |\nabla \mathbf{u}|^2 \rangle$ is several times larger than the boundary layer contribution. In this regime, the scaling arguments instead predict $\langle T \rangle \sim R^{-1/6}$. This discrepancy is not caused by taking $\langle wT \rangle$ as constant; fitting $\langle T \rangle$ to a power of \mathcal{R} rather than of R merely changes the exponent from 0.200 to 0.201, and the fit is worse. One possible explanation of the discrepancy is that the apparent $R^{-1/5}$ scaling might be a mixture of the $R^{-1/6}$ regime with a sub-dominant $R^{-1/4}$ or $R^{-1/3}$ regime, which are the scalings expected when both dissipations are bulk-dominated.⁵ To determine whether this explanation is viable, one must locate the approximate boundaries in the R - σ parameter plane that separate the various scaling regimes. This could be done using our data if one could unify the predicted scalings of $\langle T \rangle$ into a single function of R

⁵Similarly, it is argued in Grossmann and Lohse (2000) that the apparent $N \sim Ra^{2/7}$ scaling sometimes seen in RB experiments (Johnston and Doering, 2009; Castaing et al., 1989) may be interpreted as a superposition of $Ra^{1/3}$ and $Ra^{1/4}$ terms.

and σ , in analogy to the way the scalings of Grossmann and Lohse (2000) are unified in Grossmann and Lohse (2001). We have not attempted this because the lack of a theory for $\langle wT \rangle$ should be resolved before extending the scaling analysis in the manner of Grossmann and Lohse (2001, 2011).

The scaling predictions of Table 6.2 are based on the assumption of a laminar viscous boundary layer, so they do not strictly apply when $R \rightarrow \infty$. Instead, we can employ a different scaling argument for this ultimate regime. When R is very large, nearly all transport is achieved by convective turbulence, and this turbulence creates effective diffusivities different from the actual molecular parameters, κ and ν . Thus, we can argue that the mean dimensionful temperature should ultimately scale independently of the molecular parameters. The only scaling of dimensionless temperature with R and σ that satisfies this requirement is $\langle T \rangle \sim R^{-1/3} \sigma^{-1/3}$. This result suggests that $\langle T \rangle$ ultimately realizes the fastest rate of decay with R that is permitted by the variational bound of Lu et al. (2004).⁶

Our scaling arguments for $\langle T \rangle$ and the variational bounds on $\langle T \rangle$ computed in Lu et al. (2004); Whitehead and Doering (2011) have both employed methods used previously to study the Nusselt number in RB convection. The success of these methods in the present case makes sense if we recall that $\langle T \rangle$ is roughly controlled by the top thermal boundary layer, and that the top half of our internally heated layer looks quite similar to the top half of a layer undergoing RB convection. To make quantitative the parallels between $1/\langle T \rangle$ and the RB Nusselt number, we must consider a *diagnostic* Rayleigh number, $Ra := \langle T \rangle R$ (cf. section 1.2.2). This quantity is useful for analysis, though it cannot replace R as a control parameter because it requires knowledge of $\langle T \rangle$. In terms of Ra , our predicted ultimate scaling is $1/\langle T \rangle \sim Ra^{1/2} \sigma^{1/2}$, and the variational bound of Lu et al. (2004) is $1/\langle T \rangle \leq cRa^{1/2}$. These

⁶In the analogous ultimate regime of RB convection, arguing that the dimensionful heat flux should scale independently of the molecular parameters leads to the Nusselt number scaling of $N \sim Ra^{1/2} \sigma^{1/2}$ (Spiegel, 1971a). This same scaling was derived by Kraichnan (1962) using arguments based on shear layer turbulence, and it is implicit in treatments of convection zones in stars (Spiegel, 1971b).

expressions become identical to the corresponding RB results ([Spiegel, 1971a](#); [Constantin and Doering, 1996](#)) when we replace $1/\langle T \rangle$. If $\langle wT \rangle$ is furthermore taken as constant (which is not always accurate), then the scalings of Table 6.2 become identical to the scalings computed for the RB problem by [Grossmann and Lohse \(2000\)](#). All of these parallels reinforce the interpretation of $\langle T \rangle$ as an inverse Nusselt number.

6.6 Conclusions

We have conducted direct numerical simulations of 2D internally heated convection for wide ranges of σ and R , and we have presented both qualitative features and integral quantities. Qualitatively, the clearest differences from 2D RB convection are the frequent merging and genesis of downward-moving thermal plumes at moderate R and the absence of upward-moving buoyant plumes. Quantitatively, we have focused on spatiotemporal averages of temperature, $\langle T \rangle$, and vertical convective heat flux, $\langle wT \rangle$, especially at large R . With $\sigma = 1$, we obtained well-converged means for R up to $2 \cdot 10^{10}$, higher than previously reported for direct simulation ([Jahn and Reineke, 1974](#); [Wörner et al., 1997](#)). In this high- R regime we observed unanticipated R -dependencies of both integral quantities.

Firstly, $\langle wT \rangle$ stops rising and begins decreasing with increasing R in our high- R simulations, meaning that the fraction of the total emergent heat that comes out the top is decreasing. In light of this, we have made the case that $\langle T \rangle$ and $\langle wT \rangle$ are more useful than the two quantities, called top and bottom Nusselt numbers, on which most previous studies have focused. Our reasons for this preference are that once $\langle wT \rangle$ stops increasing, both Nusselt numbers will scale with R in the same way that $1/\langle T \rangle$ does, and that the Nusselt numbers do not convey the fraction of heat flowing out the top boundary as clearly as $\langle wT \rangle$ does. The ultimate fate of $\langle wT \rangle$ as $R \rightarrow \infty$ remains an open question.

Secondly, the dimensionless mean temperature scales as $\langle T \rangle \sim R^{-1/5}$ in our high- R simulations. (This corresponds to the dimensionful mean temperature scaling with the heating rate like $H^{4/5}$.) We have presented Grossman-Lohse-type scaling arguments for $\langle T \rangle$ that predict the existence of up to eight different scalings in terms of $R\langle wT \rangle$ and σ , and which may explain the scaling we observed. We have also argued that $\langle T \rangle \sim R^{-1/3}\sigma^{-1/3}$ in the ultimate regime where $R \rightarrow \infty$ for order one σ . This is the same R -dependence as in the best known variational lower bound on $\langle T \rangle$ (Lu et al., 2004). We have argued that $\langle T \rangle$ is a kind of inverse Nusselt number, and the connection between $1/\langle T \rangle$ and the Nusselt number of RB convection was strengthened by re-expressing the scaling and bounding results for $\langle T \rangle$ in terms of a diagnostic Rayleigh number, $Ra := R\langle T \rangle$ and σ .

The scaling behaviors of integral quantities are of practical as well as theoretical interest. In engineering applications where sustained chemical or nuclear reactions are heating a fluid, the containing vessel must be able to carry heat away as fast as it is created, so that the temperature will not rise indefinitely. The vessel must also be able to withstand localized spikes in temperature due to the inhomogeneity of temperature in the fluid. Such spikes in boundary temperature cannot occur with the isothermal boundaries we have imposed, but in real-world cases where the boundaries are good but imperfect conductors, we can reasonably expect that the maximum instantaneous temperatures to which the boundaries are subjected will scale with R roughly as $\langle T \rangle$ does. Knowing $\langle wT \rangle$, on the other hand, tells us the relative fractions of the produced heat that the top and bottom boundaries must be capable of carrying away. When the boundaries are imperfect conductors but still identical to one another, the larger heat flux out the top will keep the top boundary hotter than the bottom one, which works against upward heat transport and should decrease the difference between upward and downward heat fluxes. Therefore, among all configurations with identical top and bottom boundaries, our results should provide upper bounds on the fraction of heat flowing out the top boundary, an interesting result to try proving analytically.

Several open questions remain, and they invite a multifaceted attack. Further 2D simulations may help identify other scaling regimes of $\langle T \rangle$, testing the scaling arguments we have presented. Meanwhile, a better physical understanding of how the bottom thermal boundary layer interacts with the bulk could lead to predictions for the parameter-dependence of $\langle wT \rangle$ and more complete predictions for the scaling of $\langle T \rangle$. But we expect that the most promising avenue will be physical experiment. Obtaining well-converged integral quantities in 3D direct simulations may be prohibitively computationally intensive for the largest R that we have simulated in 2D. However, laboratory experiments could access such Rayleigh numbers, and they may even illuminate the asymptotic fate of $\langle wT \rangle$.

References

- Ahlers, G., Grossmann, S., and Lohse, D. (2009). Heat transfer and large scale dynamics in turbulent Rayleigh-Bénard convection. *Reviews of Modern Physics*, 81(2):503–537. [19](#), [88](#), [120](#)
- Aoyagi, T., Yagi, M., and Itoh, S.-I. (1997). Comparison analysis of Lorenz model and five components model. *J. Phys. Soc. Japan.* [31](#), [47](#), [143](#)
- Arcidiacono, S. and Ciofalo, M. (2001). Low-Prandtl number natural convection in volumetrically heated rectangular enclosures III. Shallow cavity, AR=0.25. *International Journal of Heat and Mass Transfer*, 44:3053–3065. [97](#)
- Berlengier, M., Emanuel, K. A., von Hardenberg, J., Provenzale, A., and Spiegel, E. A. (2012). Internally cooled convection: A fillip for Philip. *Communications in Nonlinear Science and Numerical Simulation*, 17(5):1998–2007. [97](#)
- Berning, M. and Spatschek, K. H. (2000). Bifurcations and transport barriers in the resistive paradigm. *Physical Review E*, 62:1162–1174. [31](#), [47](#), [61](#), [141](#)
- Bian, N., Benkadda, S., Garcia, O. E., Paulsen, J.-V., and Garbet, X. (2003). The quasilinear behavior of convective turbulence with sheared flows. *Physics of Plasmas*, 10(5):1382. [67](#)
- Bian, N. H. and Garcia, O. E. (2003). Confinement and dynamical regulation in two-dimensional convective turbulence. *Physics of Plasmas*, 10(12):4696–4707. [87](#)
- Busse, F. H. (1983). Generation of mean flows by thermal convection. *Physica D*, 9:287–299. [24](#)
- Busse, F. H. (1994). Convection driven zonal flows and vortices in the major planets. *Chaos (Woodbury, N.Y.)*, 4(2):123–134. [19](#)
- Busse, F. H. and Whitehead, J. A. (1974). Oscillatory and collective instabilities in large Prandtl number convection. *Journal of Fluid Mechanics*, 66(1):67–79. [56](#)
- Castaing, B., Gunaratne, G., Heslot, F., Kadanoff, L., Libchaber, A., Thomae, S., Wu, X.-Z., Zaleski, S., and Zanetti, G. (1989). Scaling of hard thermal turbulence in Rayleigh-Bénard convection. *Journal of Fluid Mechanics*, 204(1):1–30. [121](#)

- Catton, I. and Suo-Anttila, A. J. (1974). Heat transfer from a volumetrically heated horizontal fluid layer. In *Proc. Fifth Int. Heat Transfer Conf.*, pages NC-2.7, Tokyo. Hemisphere. 111
- Chandrasekhar, S. (1981). *Hydrodynamic and Hydromagnetic Stability*. Dover Publications. 32, 52, 98
- Chapman, C. J. and Proctor, M. R. E. (1980). Nonlinear Rayleigh-Bénard convection between poorly conducting boundaries. *Journal of Fluid Mechanics*, 101(04):759–782. 9, 138
- Chen, S. and Krafczyk, M. (2009). Entropy generation in turbulent natural convection due to internal heat generation. *International Journal of Thermal Sciences*, 48(10):1978–1987. 96
- Cheung, F. B. and Chawla, T. C. (1987). Complex heat transfer processes in heat-generating horizontal fluid layers. *Annual Review of Numerical Fluid Mechanics and Heat Transfer*, 1:403–448. 96
- Childs, H., Brugger, E., Whitlock, B., Meredith, J., Ahern, S., Bonnell, K., Miller, M., Weber, G. H., Harrison, C., Pugmire, D., Fogal, T., Garth, C., Sanderson, A., Bethel, E. W., Durant, M., Camp, D., Favre, J. M., Rübel, O., Navrátil, P., Wheeler, M., Selby, P., and Vivodtzev, F. (2011). VisIt: An end-user tool for visualizing and analyzing very large data. In *Proceedings of SciDAC 2011*. 100, 164
- Chini, G. P. and Cox, S. M. (2009). Large Rayleigh number thermal convection: Heat flux predictions and strongly nonlinear solutions. *Physics of Fluids*, 21(8):083603. 45, 57
- Cho, J. and Polvani, L. (1996). The emergence of jets and vortices in freely evolving, shallow-water turbulence on a sphere. *Physics of Fluids*, 8(June):1531–1552. 19
- Clever, R. M. and Busse, F. H. (1981). Low-Prandtl-number convection in a layer heated from below. *Journal of Fluid Mechanics*, 102:61–74. 106
- Constantin, P. and Doering, C. R. (1996). Variational bounds on energy dissipation in incompressible flows. III. Convection. *Physical Review E*, 53(6):5957–5981. 15, 111, 123
- Diamond, P. H., Itoh, S.-I., Itoh, K., and Hahm, T. S. (2005). Zonal flows in plasma — a review. *Plasma Physics and Controlled Fusion*, 47(5):R35–R161. 19, 22, 26, 44
- Doedel, E., Keller, H., and Kernevez, J. (1991). Numerical analysis and control of bifurcation problems (II): Bifurcation in infinite dimensions. *International Journal of Bifurcation and Chaos in Applied Sciences and Engineering*, 1(4):745–772. 137
- Dooge, A., Govaerts, W., and Kuznetsov, Y. A. (2003). MatCont: A MATLAB package for numerical bifurcation analysis of ODEs. *ACM TOMS*, 29:141–164. 55

- Drake, J. F., Finn, J. M., Guzdar, P., Shapiro, V., Shevchenko, V., Waelbroeck, F., Hassam, A. B., Liu, C. S., and Sagdeev, R. (1992). Peeling of convection cells and the generation of sheared flow. *Physics of Fluids B: Plasma Physics*, 4(3):488–491. [53](#)
- Finn, J. M., Drake, J. F., and Guzdar, P. N. (1992). Instability of fluid vortices and generation of sheared flow. *Physics of Fluids B: Plasma Physics*, 4(9):2758. [25](#), [53](#)
- Fisher, P. F., Lottes, J. W., and Kerkemeier, S. G. (2013). nek5000 Web page. [22](#), [100](#), [136](#), [164](#), [168](#)
- Garcia, O. E. and Bian, N. H. (2003). Bursting and large-scale intermittency in turbulent convection with differential rotation. *Physical Review E*, 68(4):1–4. [21](#), [67](#), [87](#)
- Garcia, O. E., Bian, N. H., Naulin, V., Nielsen, A. H., and Rasmussen, J. J. (2006a). Two-dimensional convection and interchange motions in fluids and magnetized plasmas. *Physica Scripta*, T122:104–124. [19](#), [26](#), [67](#), [82](#), [87](#), [91](#)
- Garcia, O. E., Bian, N. H., Paulsen, J.-V., Benkadda, S., and Rypdal, K. (2003). Confinement and bursty transport in a flux-driven convection model with sheared flows. *Plasma Physics and Controlled Fusion*, 45:919–932. [67](#), [88](#)
- Garcia, O. E., Naulin, V., Nielsen, A. H., and Rasmussen, J. J. (2006b). Turbulence simulations of blob formation and radial propagation in toroidally magnetized plasmas. *Physica Scripta*, T122:89–103. [28](#)
- Getling, A. V. (1998). *Rayleigh-Bénard Convection: Structures and Dynamics*. World Scientific Publishing Co. [5](#)
- Gluhovsky, A., Tong, C., and Agee, E. (2002). Selection of modes in convective low-order models. *J. Atmos. Sci.*, 59:1383–1393. [47](#), [50](#), [51](#), [52](#), [143](#)
- Golubitsky, M. and Stewart, I. (2000). *The Symmetry Perspective: From Equilibrium to Chaos in Phase Space and Physical Space*. Birkhäuser Verlag. [10](#)
- Goluskin, D. and Spiegel, E. A. (2012). Convection driven by internal heating. *Physics Letters A*, 377(1-2):83–92. [95](#)
- Grossmann, S. and Lohse, D. (2000). Scaling in thermal convection: a unifying theory. *Journal of Fluid Mechanics*, 407:27–56. [88](#), [91](#), [92](#), [111](#), [119](#), [120](#), [121](#), [122](#), [123](#)
- Grossmann, S. and Lohse, D. (2001). Thermal convection for large Prandtl numbers. *Physical Review Letters*, 86(15):3316–3319. [119](#), [122](#)
- Grossmann, S. and Lohse, D. (2004). Fluctuations in turbulent Rayleigh-Bénard convection: The role of plumes. *Physics of Fluids*, 16(12):4462–4472. [119](#)

- Grossmann, S. and Lohse, D. (2011). Multiple scaling in the ultimate regime of thermal convection. *Physics of Fluids*, 23(4):045108. [119](#), [122](#)
- Grötzsch, G. and Wörner, M. (1999). Direct numerical and large eddy simulations in nuclear applications. *International Journal of Heat and Fluid Flow*, 20(3):222–240. [96](#)
- Hartlep, T., Tilgner, A., and Busse, F. H. (2003). Large scale structures in Rayleigh-Bénard convection at high Rayleigh numbers. *Physical Review Letters*, 91(6):8–11. [19](#)
- Hartlep, T., Tilgner, A., and Busse, F. H. (2005). Transition to turbulent convection in a fluid layer heated from below at moderate aspect ratio. *Journal of Fluid Mechanics*, 544:309–322. [19](#)
- Heimpel, M. and Aurnou, J. (2007). Turbulent convection in rapidly rotating spherical shells: A model for equatorial and high latitude jets on Jupiter and Saturn. *Icarus*, 187:540–557. [19](#)
- Hermiz, K. B., Guzdar, P. N., and Finn, J. M. (1995). Improved low-order model for shear flow driven by Rayleigh-Benard convection. *Physical Review E*, 51(1):325–331. [31](#), [47](#), [58](#), [61](#), [141](#)
- Horton, W., Hu, G., and Laval, G. (1996). Turbulent transport in mixed states of convective cells and sheared flows. *Physics of Plasmas*, 3(8):2912. [31](#), [87](#)
- Horvat, A., Kljenak, I., and Marn, J. (2001). Two-dimensional large-eddy simulation of turbulent natural convection due to internal heat generation. *International Journal of Heat and Mass Transfer*, 44(21):3985–3995. [96](#)
- Houseman, G. (1988). The dependence of convection planform on mode of heating. *Nature*, 332:346–349. [96](#)
- Howard, L. N. (1963). Heat transport by turbulent convection. *Journal of Fluid Mechanics*, 17(3):405–432. [111](#)
- Howard, L. N. (1972). Bounds on flow quantities. *Annual Review of Fluid Mechanics*, 4:473–494. [15](#), [111](#)
- Howard, L. N. and Krishnamurti, R. (1986). Large-scale flow in turbulent convection: a mathematical model. *Journal of Fluid Mechanics*, 170(1):385–410. [21](#), [24](#), [25](#), [31](#), [32](#), [33](#), [47](#), [54](#), [61](#), [62](#), [65](#), [66](#), [91](#), [142](#), [145](#), [146](#), [160](#)
- Hughes, D. W. and Proctor, M. R. E. (1990). A low-order model of the shear instability of convection: chaos and the effect of noise. *Nonlinearity*, 3:127–153. [47](#), [142](#), [158](#), [159](#), [160](#), [163](#)

- Hurle, D. T. J., Jakeman, E., and Pike, E. R. (1967). On the solution of the Bénard problem with boundaries of finite conductivity. *Proceedings of the Royal Society of London. Series A. Mathematical and Physical Sciences*, 296(1447):469–475. [8](#)
- Jahn, M. and Reineke, H. H. (1974). Free convection heat transfer with internal heat sources, calculations and measurements. In *Proceedings of the Fifth International Heat Transfer Conference*, pages 74–78. [96](#), [114](#), [123](#)
- Johnston, H. and Doering, C. R. (2009). Comparison of turbulent thermal convection between conditions of constant temperature and constant flux. *Physical Review Letters*, 102(6):064501. [9](#), [14](#), [15](#), [90](#), [121](#), [138](#), [165](#)
- Joseph, D. D. (1976). *Stability of Fluid Motions*. Springer-Verlag. [100](#)
- Kelley, C. T. (2003). *Solving Nonlinear Equations with Newton's Method*. Society for Industrial and Applied Mathematics. [136](#)
- Kelley, C. T. and Keyes, D. E. (1998). Convergence analysis of pseudo-transient continuation. *SIAM Journal on Numerical Analysis*, 35(2):508–523. [136](#)
- Kippenhahn, R. and Weigert, A. (1994). *Stellar Structure and Evolution*. Springer. [97](#)
- Koschmieder, E. L. (1993). *Bénard Cells and Taylor Vortices*. Cambridge University Press. [36](#)
- Kraichnan, R. H. (1962). Turbulent thermal convection at arbitrary Prandtl number. *Physics of Fluids*, 5(11):1374–1389. [122](#)
- Krishnamurti, R. and Howard, L. N. (1981). Large-scale flow generation in turbulent convection. *Proceedings of the National Academy of Sciences of the United States of America*, 78(4):1981–5. [18](#), [19](#), [21](#), [22](#), [26](#)
- Kulacki, F. A. and Goldstein, R. J. (1972). Thermal convection in a horizontal fluid layer with uniform volumetric energy sources. *Journal of Fluid Mechanics*, 55(02):271–287. [96](#), [101](#), [102](#), [104](#), [114](#), [116](#)
- Kulacki, F. A. and Goldstein, R. J. (1974). Eddy heat transport in thermal convection with volumetric energy sources. In *Proc. Fifth Int. Heat Transfer Conf.*, pages NC–2.6, Tokyo. Hemisphere. [96](#)
- Kulacki, F. A. and Goldstein, R. J. (1975). Hydrodynamic instability in fluid layers with uniform volumetric energy sources. *Applied Scientific Research*, 31(2):81–109. [100](#)
- Kulacki, F. A. and Richards, D. E. (1985). Natural convection in plane layers and cavities with volumetric energy sources. In *Natural Convection: Fundamentals and Applications*, pages 179–254. Hemisphere, New York. [96](#), [99](#), [112](#), [113](#)

- Leboeuf, J. N. and Charlton, L. A. (1993). Shear flow effects on the nonlinear evolution of thermal instabilities. *Physics of Fluids B: Plasma Physics*, 5(8):2959–2966. [82](#), [87](#)
- Lee, S. D., Lee, J. K., and Suh, K. Y. (2007). Boundary condition dependent natural convection in a rectangular pool with internal heat sources. *Journal of Heat Transfer*, 129(5):679–682. [96](#)
- Liu, H., Zou, C., Shi, B., Tian, Z., Zhang, L., and Zheng, C. (2006). Thermal lattice-BGK model based on large-eddy simulation of turbulent natural convection due to internal heat generation. *International Journal of Heat and Mass Transfer*, 49(23-24):4672–4680. [96](#)
- Lorenz, E. N. (1963). Deterministic nonperiodic flow. *Journal of the Atmospheric Sciences*, 20:130–141. [47](#), [50](#), [51](#), [62](#)
- Lotka, A. J. (1925). *Elements of Physical Biology*. Williams and Wilkins. [87](#)
- Lu, L., Doering, C. R., and Busse, F. H. (2004). Bounds on convection driven by internal heating. *Journal of Mathematical Physics*, 45(7):2967–2986. [99](#), [108](#), [110](#), [111](#), [117](#), [118](#), [122](#), [124](#), [167](#)
- Malkov, M. A., Diamond, P. H., and Rosenbluth, M. N. (2001). On the nature of bursting in transport and turbulence in drift wavezonal flow systems. *Physics of Plasmas*, 8(12):5073. [87](#)
- Malkus, W. V. R. (1954). The heat transport and spectrum of thermal turbulence. *Proceedings of the Royal Society of London. Series A. Mathematical and Physical Sciences*, 225(1161):196–212. [111](#)
- Manning, M., Bamieh, B., and Carlson, J. (2008). Descriptor approach for eliminating spurious eigenvalues in hydrodynamic equations. *arXiv preprint arXiv:0705.1542*. [138](#)
- Matthews, P. C., Rucklidge, A. M., Weiss, N. O., and Proctor, M. R. E. (1996). The three-dimensional development of the shearing instability of convection. *Physics of Fluids*, 51(6):325. [20](#), [143](#)
- Moore, D. R. and Weiss, N. O. (1973). Two-dimensional Rayleigh-Bénard convection. *Journal of Fluid Mechanics*, 58(2):289–312. [106](#)
- Nourgaliev, R. R., Dinh, T. N., and Sehgal, B. R. (1997). Effect of fluid Prandtl number on heat transfer characteristics in internally heated liquid pools with Rayleigh numbers up to 10^{12} . *Nuclear Engineering and Design*, 169:165–184. [96](#)
- Otero, J., Wittenberg, R. W., Worthing, R. A., and Doering, C. R. (2002). Bounds on Rayleigh-Bénard convection with an imposed heat flux. *Journal of Fluid Mechanics*, 473:191–199. [14](#), [15](#), [139](#)
- Peyret, R. (2002). *Spectral Methods for Incompressible Viscous Flow*. Springer-Verlag. [135](#)

- Prat, J., Mercader, I., and Knobloch, E. (1998). Resonant mode interactions in Rayleigh-Bénard convection. *Physical Review E*, 58(3):3145–3156. [141](#)
- Proctor, M. R. E. (1977). Inertial convection at low Prandtl number. *Journal of Fluid Mechanics*, 82(01):97–114. [106](#)
- Rayleigh, L. (1916). On convection currents in a horizontal layer of fluid, when the higher temperature is on the under side. *Philosophical Magazine*, 32(192). [7](#), [32](#), [52](#), [69](#)
- Roberts, P. H. (1967). Convection in horizontal layers with internal heat generation. Theory. *Journal of Fluid Mechanics*, 30(01):33–49. [98](#)
- Rucklidge, A. M. and Matthews, P. C. (1996). Analysis of the shearing instability in nonlinear convection and magnetoconvection. *Nonlinearity*, 9(311-351). [21](#), [25](#), [30](#), [31](#), [37](#), [38](#), [45](#), [47](#), [55](#), [61](#), [65](#), [66](#), [68](#), [91](#), [142](#), [151](#), [157](#), [158](#), [159](#), [160](#), [161](#), [162](#)
- Saltzman, B. (1962). Finite amplitude free convection as an initial value problem-I. *Journal of the Atmospheric Sciences*, 19:329–341. [47](#)
- Schmalzl, J., Breuer, M., and Hansen, U. (2004). On the validity of two-dimensional numerical approaches to time-dependent thermal convection. *Europhysics Letters*, 67(3):390–396. [104](#), [114](#)
- Siggia, E. (1994). High Rayleigh number convection. *Annual Review of Fluid Mechanics*, 26:137–168. [5](#)
- Sotin, C. and Labrosse, S. (1999). Three-dimensional thermal convection in an iso-viscous, infinite Prandtl number fluid heated from within and from below: applications to the transfer of heat through planetary mantles. *Physics of the Earth and Planetary Interiors*, 112(3-4):171–190. [96](#)
- Sparrow, E. M., Goldstein, R. J., and Jonsson, V. K. (1963). Thermal instability in a horizontal fluid layer: effect of boundary conditions and non-linear temperature profile. *Journal of Fluid Mechanics*, 18(04):513–528. [8](#), [9](#), [100](#)
- Spiegel, E. A. (1962). Thermal turbulence at very small Prandtl number. *Journal of Geophysical Research*, 67(8):3063–3070. [106](#)
- Spiegel, E. A. (1971a). Convection in stars I. Basic Boussinesq convection. *Annual Review of Astronomy and Astrophysics*, 9:323–352. [122](#), [123](#)
- Spiegel, E. A. (1971b). Turbulence in stellar convection zones. *Comments on Astrophysics and Space Physics*, 3(2). [122](#)
- Spiegel, E. A. and Veronis, G. (1960). On the Boussinesq approximation for a compressible fluid. *The Astrophysical Journal*, pages 442–447. [3](#), [4](#)

- Stevens, R. J. A. M., Verzicco, R., and Lohse, D. (2010). Radial boundary layer structure and Nusselt number in Rayleigh-Bénard convection. *Journal of Fluid Mechanics*, 643(2010):495–507. [115](#)
- Taylor, G. (1953). Dispersion of soluble matter in solvent flowing slowly through a tube. *Proceedings of the Royal Society of London. Series A. Mathematical and Physical Sciences*, 219(1137):186–203. [72](#)
- Terry, P. (2000). Suppression of turbulence and transport by sheared flow. *Reviews of Modern Physics*, 72(1):109–165. [26](#), [44](#)
- Thiffeault, J.-L. (1995). *Modeling shear flow in Rayleigh-Bénard convection (Master's thesis)*. Universit of Texas at Austin. [52](#), [53](#)
- Thiffeault, J.-L. and Horton, W. (1996). Energy-conserving truncations for convection with shear flow. *Physics of Fluids*, 8(7):1715. [47](#), [52](#), [53](#)
- Thompson, R. (1970). Venus's general circulation is a merry-go-round. *Journal of Atmospheric Sciences*, 27(8):1107–1116. [21](#), [24](#)
- Thual, O. (1992). Zero-Prandtl-number convection. *Journal of Fluid Mechanics*, 240:229–258. [106](#)
- Travis, B. and Olson, P. (1994). Convection with internal heat sources and thermal turbulence in the Earth's mantle. *Geophysical Journal International*, 118(1):1–19. [96](#)
- Trefethen, L. N. (2000). *Spectral Methods in MATLAB*. Society for Industrial and Applied Mathematics. [136](#)
- Tuckerman, L. S. and Barkley, D. (1990). Bifurcation analysis of the Eckhaus instability. *Physica A*, 46:57–86. [40](#), [141](#)
- von Hardenberg, J., Parodi, A., Passoni, G., Provenzale, A., and Spiegel, E. A. (2008). Large-scale patterns in Rayleigh-Bénard convection. *Physics Letters A*, 372(13):2223–2229. [105](#)
- Wagner, F. (2007). A quarter-century of H-mode studies. *Plasma Physics and Controlled Fusion*, 49(12B):B1–B33. [19](#), [29](#), [68](#)
- Wesson, J. (2011). *Tokamaks*. Oxford University Press, 4th edition. [19](#), [26](#)
- Whitehead, J. P. and Doering, C. R. (2011). Internal heating driven convection at infinite Prandtl number. *Journal of Mathematical Physics*, 52(9):093101. [111](#), [118](#), [119](#), [122](#)
- Wittenberg, R. W. (2010). Bounds on Rayleigh-Bénard convection with imperfectly conducting plates. *Journal of Fluid Mechanics*, 665:158–198. [14](#), [15](#)

- Wörner, M., Schmidt, M., and Grötzbach, G. (1997). Direct numerical simulation of turbulence in an internally heated convective fluid layer and implications for statistical modeling. *Journal of Hydraulic Research*, 35(6):773–797. [96](#), [102](#), [114](#), [115](#), [123](#)
- Zahn, J.-P. (1991). Convective penetration in stellar interiors. *Astronomy and Astrophysics*, 252(11):179–188. [101](#)
- Zebib, A. (1987). Removal of spurious modes encountered in solving stability problems by spectral methods. *Journal of Computational Physics*, 70:521–525. [138](#)
- Zocchi, G., Moses, E., and Libchaber, A. (1990). Coherent structures in turbulent convection, an experimental study. *Physica A*, 166:387–407. [104](#)

Appendix A

Appendix to Chapter 3

A.1 Numerical methods

The computations reported in this Chapter were performed with a MATLAB code written to solve the 2D Boussinesq equations in their stream function formulation. For the purpose of numerics we employ a somewhat different scaling ([Peyret, 2002](#)) than is used to derive the HK8 model in Chapter 4. The dimensionless domain is bounded by $0 \leq x \leq 2\pi$ and $-1 \leq z \leq 1$. This is ideal for numerical computation because the geometry no longer depends on A , and the ranges of x and z are convenient for the chosen bases. The scaled PDE governing the dimensionless temperature perturbation and stream function are

$$\partial_t \nabla^2 \psi - \{\psi, \nabla^2 \psi\} = \sigma \nabla^4 \psi - k \sigma \partial_x \theta \quad (\text{A.1})$$

$$\partial_t \theta - \{\psi, \theta\} = \nabla^2 \theta - \frac{k}{8} Ra \partial_x \psi, \quad (\text{A.2})$$

where $\{f, g\} := k \partial_x f \partial_z g - \partial_z f \partial_x g$, $\nabla = (k \partial_x, \partial_z)$, and $(u, v) = (\partial_z \psi, -k \partial_x \psi)$. We employed a spectral method with a Fourier basis in the (periodic) horizontal direction and a Chebyshev

basis in the vertical. Numerical differentiation was performed in physical space using roughly the methods described by [Trefethen \(2000\)](#).

Switched evolution relaxation Time integration of the Boussinesq equations at high Rayleigh numbers, on which we report in Chapters [5](#) and [6](#), was performed in parallel with the `nek5000` code ([Fisher et al., 2013](#)). Time-stepping was implemented in our own code only to find stable steady states from arbitrary initial guesses. (Solving the steady equations directly by Newton iteration is efficient only for close initial guesses.) To this end, we implemented a fully implicit Euler method with switched evolution relaxation ([Kelley and Keyes, 1998](#)). That is, the implicit time step was varied in inverse proportion to the norm of the approximated time derivatives. Since time derivatives decrease as the solution approaches a steady state, successively longer time steps will be taken. Eventually one switches to solving the steady equations iteratively, which is equivalent to taking an infinite implicit time step. We found integrating the equations in spectral space to be no faster than integrating them in physical space because of the large proportion of terms that are nonlinear.

Steady states Solving the steady Boussinesq equations requires solving nonlinear algebraic equations (as does computing an implicit time step). For this purpose we used the `nsold` routine described in [Kelley \(2003\)](#), which implements a Newton-Armijo method. Given a close initial guess, this method will converge to a steady state whether or not the state is stable, whereas switched evolution relaxation finds only stable states. Thus, having found a stable steady state, one can continue it in parameter space using a steady solver, thereby obtaining a branch of steady states that may or may not be stable. To continue a known solution to a nearby parameter value, we simply changed the parameter value and used the known solution as an initial guess in the steady solver. This minimal implementa-

tion sufficed for our needs, though it could be accelerated by using a parameter continuation method that extrapolates from multiple known solutions to obtain a better initial guess for the steady solver, as described by Doedel et al. (1991). Our simplistic method fails only when approaching a turning point in the continuation parameter (say, Ra), as occurs at a saddle-node bifurcation. To round such a turning point, we identify a mesh point at which the value of the stream function changes rapidly as Ra nears its turning point. We then temporarily use the value of the stream function at this point as the continuation parameter, resuming continuation in Ra after the turning point has been passed. At the largest Rayleigh numbers on which we report, as many as 32 vertical modes were needed for the Nusselt number of a steady state to converge to four significant figures, while the number of horizontal modes needed was as large as 64, depending on the aspect ratio. Linear stability calculations required higher resolution.

Linear stability Having computed branches of steady states, we wish to determine their linear stabilities. This amounts to linearizing the perturbation operator about the steady state of interest and computing the eigenvalues in the operator’s spectrum that have the largest real parts. In practice, we compute the spectrum of a matrix that is a discretization of the differential linear operator. A steady state is stable only if all eigenvalues of the linearized perturbation operator have negative real parts. If a state is unstable, the number of eigenvalues with positive real parts gives the local dimension of its unstable manifold. At bifurcation points, one or more eigenvalues will have a real part equal to zero.

The spectra of matrices were computed using MATLAB’s `eig` routine. This routine implements QZ factorization, which yields the complete spectrum of a matrix, whether or not the matrix is singular. For large problems, it is more common to compute eigenvalues by Arnoldi iteration, which is much faster when one needs only a few leading eigenvalues. (Strictly speaking, the leading eigenvalues of a matrix A are the ones of largest amplitude.

In stability computations one seeks the eigenvalues with the largest real parts, which are the leading eigenvalues of e^A . Arnoldi methods are well developed for either case.) We did not use Arnoldi iteration because it sometimes produced spurious unphysical eigenvalues. These eigenvalues arise because the Dirichlet boundary conditions on the vorticity, ω , at the top and bottom boundaries are not explicitly enforced in our implementation; the zero boundary values of ψ are automatically satisfied by the Chebyshev basis, but the zero boundary values of ω are only approximately satisfied when we compute ω by inverting the Laplacian in the relation $\omega + \Delta\psi = 0$ ([Zebib, 1987](#)). The simplest way to remove the spurious eigenvalues, if not the most computationally efficient, is to augment the linear stability matrix with equations that explicitly enforce the boundary conditions on ω , as in [Manning et al. \(2008\)](#). The resulting matrix is singular, so Arnoldi iteration in its most basic form can no longer be used, but since our problem size is moderate, we can simply find the spectra of the singular stability matrix by QZ factorization. Even with this inefficiency, such linear stability calculations are an order of magnitude faster than the computation of the steady states themselves. Computing leading eigenvalues to a given accuracy required nearly double the resolution in both directions as computing the Nusselt number of a steady state to the same accuracy.

A.2 *L_1 and TC states with fixed-flux thermal boundary conditions*

Branches of TC states also exist if convection is driven by fixed thermal fluxes at the top and bottom boundaries, rather than a fixed temperature difference. Fixed-flux convection differs significantly from fixed-temperature convection near onset ([Chapman and Proctor, 1980](#)), but the two cases are scarcely distinguishable at very large Rayleigh numbers ([Johnston and](#)

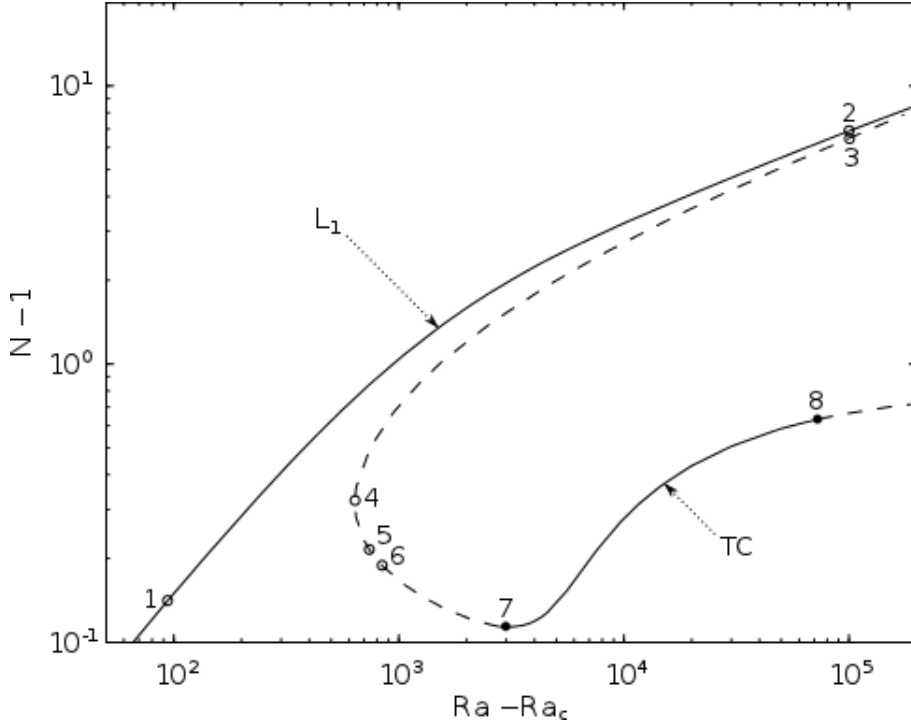


Figure A.1: Bifurcation diagram depicting the gravest L_1 and TC steady states with $\sigma = 0.1$, $A = 2$ and fixed-flux thermal boundary conditions — the fixed-flux analog of Figure 3.1. Stable (—) and unstable (---) states are shown. Marginally stable states are indicated by dots (.), while certain generic states are indicated by circles (o). The states numbered 1 through 8 are shown in Figure A.2.

(Doering, 2009; Otero et al., 2002). For our base case of $A = 2$ and $\sigma = 0.1$, we have computed L_1 and TC solution branches with fixed-flux boundary conditions. The resulting bifurcation diagram is shown in Figure A.1, and some representative steady states are shown in Figure A.2. Both the bifurcation diagram and the representative solutions bear strong resemblance to their fixed-temperature analogs in Figures 3.1 and 3.2. We have also found TC states in preliminary calculations on convection driven by uniform internal heat production, rather than by the thermal boundary conditions. Indeed, since the basic mechanism that diverts kinetic energy to the mean shear is purely fluid mechanical and relies on convection only to drive roll-like motion, we expect that TC states will exist in nearly any sort of 2D convection when the domain is laterally periodic with free-slip top and bottom boundaries.

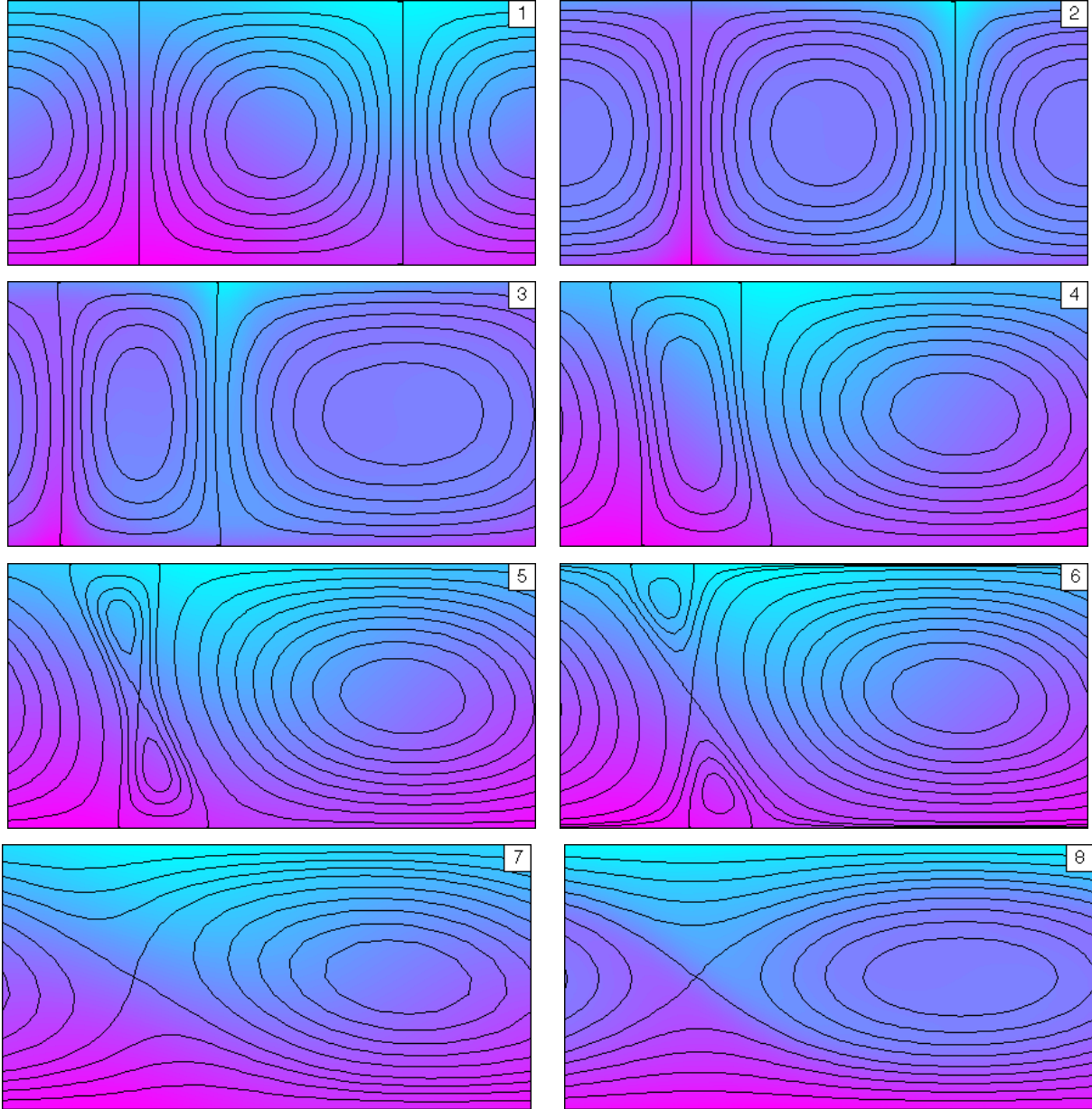


Figure A.2: Example L_1 and TC steady states of the 2D Boussinesq equations with $\sigma = 0.1$, $A = 2$, and fixed-flux thermal boundary conditions. The numbers 1 through 8 correspond to points labeled on the bifurcation diagram of Figure A.1. Solid lines are streamlines, and color represents temperature. To qualitatively represent the various flows as well as possible, the stream function intervals between streamlines differ within and between the different images. The temperature scales are identical, with the hottest fluid (purple) being one dimensionless degree warmer than the coldest fluid (blue). The central rolls in states 1 and 2 rotate clockwise; the dominant rolls in states 3 through 8 rotate counter-clockwise. Similarities to the example fixed-temperature solutions of Figure 3.2 are evident.

Appendix B

Appendix to Chapter 4

B.1 Other truncated models

Larger models The effects of adding higher horizontal wavenumbers to the HK6 system were explored by [Berning and Spatschek \(2000\)](#), where significant dynamical changes resulted from adding ψ_{21} , the mode corresponding to a 4-by-1 array of rolls. The authors attribute these changes to the $(2, 1)$ roll branch bifurcating at a lower \mathcal{R} than the $(1, 2)$ roll branch for their chosen aspect ratio. Indeed, the width of the domain strongly affects which modes are most significant since Rayleigh numbers at which various (m, n) roll branches bifurcate are non-monotonic in m . In the HK+ ψ_{21} model, as in the HK+ ψ_{03} model of [Hermiz et al. \(1995\)](#), the TC bifurcation can vanish from the L_1 branch as the aspect ratio of the domain increases ([Berning and Spatschek, 2000](#)). Once the HK8 model's bifurcation structure is more completely understood, one might turn to models that contain multiple horizontal wavenumbers. For instance, a coupling of the $(1, 1)$, $(1, 2)$, $(2, 1)$, and $(2, 2)$ Lorenz triplets through shear modes would yield a twelve-dimensional ODE. Such a model could shed light on features of the PDE such as horizontal resonances and mixed states (as described, for instance, by [Tuckerman and Barkley, 1990; Prat et al., 1998](#)).

Smaller models Although the HK8 model is the smallest conservative truncation that supports zonal flow and is asymptotically accurate at onset, many prior studies have employed smaller truncations. In some cases, such as the seminal study of [Howard and Krishnamurti \(1986\)](#), lower-order models are possible because conservation of energy and vorticity are not enforced. In other studies, modes have been eliminated by taking the limit of small aspect ratio or Prandtl number — small A or σ — or by using closure assumptions to slave certain modes to others.

In the limit of narrow rolls, the leading-order dynamics of the HK6 system takes place on a four-dimensional slow manifold ([Hughes and Proctor, 1990](#); [Rucklidge and Matthews, 1996](#)). The system can thus be reduced to a fourth-order ODE that we call the narrow-HK6 model. Since the HK6 model is only faithful to the full PDE in fairly narrow domains, the narrow-HK6 model captures the behavior of the PDE nearly as well and with reduced complexity. [Rucklidge and Matthews \(1996\)](#) studied the bifurcation structure of the narrow-HK6 model in considerable detail. In addition to finding steady, periodic, and chaotic solutions with zonal flow, they identified a number of global bifurcations, including the partial restoration of broken symmetries by gluing bifurcations in which symmetry-related periodic orbits merge. The narrow-HK6 model captures the L_1 and TC steady states of the PDE very well in the limit of a narrow domain and small σ , but it has the same shortcomings as the full HK6 model. The conserved quantities are restored if one instead takes the narrow-roll limit of the HK8 system, yielding a sixth-order system that we call the narrow-HK8 model. We discuss the narrow-HK8 model in [Appendix B.6](#), though we have not studied it nearly as thoroughly as [Rucklidge and Matthews \(1996\)](#) studied its narrow-HK6 counterpart.

Taking the small- σ limit of the narrow-HK6 model results in a three-dimensional system studied by [Hughes and Proctor \(1990\)](#). Although minimal, their model demonstrates how the interaction of the ψ_{11} and ψ_{12} modes can sustain the ψ_{01} mode, and it displays rich behaviors, such as period doubling, chaos, and sensitivity to additive random noise. The

analog of the narrow-HK6 model for 3D convection is a seventh-order ODE studied briefly by [Matthews et al. \(1996\)](#).

Omitting the θ_{12} mode from the HK6 model leaves a fifth-order model for which regimes of period doubling and chaos have been seen ([Aoyagi et al., 1997](#)). This omission renders L_2 even less realistic, but it also restores conservation of truncated energy in the dissipationless limit, so the model's dynamical behavior is not necessarily less physical than that of the HK6 model. Adding the ψ_{03} mode would restore conservation of vorticity as well. The resulting sixth-order model is the minimal conservative truncation that supports zonal flow, but, unlike the HK8 model, it does not represent L_1 and L_2 accurately in the weakly supercritical limit ([Gluhovsky et al., 2002](#)).

B.2 Linear stability matrices of HK8

Linear perturbations of L_1 steady states within the L_1 subspace are governed by the matrix operator

$$\begin{bmatrix} -\sigma(k^2 + 1) & \frac{\sigma k}{k^2 + 1} & 0 \\ \mathcal{R}_c k & -(k^2 + 1) & -k\psi_{11} \\ \frac{1}{2}k\theta_{11} & \frac{1}{2}k\psi_{11} & -4 \end{bmatrix}, \quad (\text{B.1})$$

where the values of ψ_{11} and θ_{11} are given by [\(4.9\)](#), the L_1 state about which the perturbation operator is linearized. The characteristic equation of this matrix is

$$\lambda^3 + [(\sigma + 1)(k^2 + 1) + 4] \lambda^2 + 4(k^2 + 1)(\mathcal{R}/\mathcal{R}_c + \sigma)\lambda + 8\sigma(k^2 + 1)^2(\mathcal{R}/\mathcal{R}_c - 1) = 0. \quad (\text{B.2})$$

Only even powers of k enter [\(B.2\)](#), as is also true for the characteristic equations of the other three stability matrices considered below. The L_1 branch undergoes an in-subspace Hopf

bifurcation when equation (B.2) has a pair of imaginary roots. This occurs at a Rayleigh number of \mathcal{R}_H , as defined by expression (4.13).

There are five modes orthogonal to the L_1 subspace, but the θ_{04} mode is linearly uncoupled from the others and always stable. The linear stability of the remaining four modes, $\{\psi_{01}, \psi_{12}, \theta_{12}, \psi_{03}\}$, is governed by the matrix operator

$$\begin{bmatrix} -\sigma & -\frac{3}{4}k\psi_{11} & 0 & 0 \\ -\frac{1}{2}\frac{k^3}{k^2+4}\psi_{11} & -\sigma(k^2 + 4) & -\frac{\sigma k}{k^2+4} & \frac{3}{2}k\frac{k^2-8}{k^2+4}\psi_{11} \\ \frac{1}{2}k\theta_{11} & -\mathcal{R}k & -(k^2 + 4) & -\frac{3}{2}k\theta_{11} \\ 0 & \frac{1}{4}k\psi_{11} & 0 & -9\sigma \end{bmatrix}, \quad (\text{B.3})$$

where the values of ψ_{11} and θ_{11} are given by (4.9). This matrix does not have purely imaginary eigenvalues for any admissible parameter values, so L_1 never undergoes an out-of-subspace Hopf bifurcation. The out-of-subspace pitchfork bifurcation at a Rayleigh number of \mathcal{R}_* , as defined by expression (4.11), occurs when a single eigenvalue vanishes.

The linear stability of L_2 within its own subspace is entirely analogous to the in-subspace stability of L_1 since the second Lorenz triplets is simply a rescaled version of the first. In-subspace the L_2 subspace are governed by the matrix operator

$$\begin{bmatrix} -\sigma(k^2 + 4) & -\frac{\sigma k}{k^2+4} & 0 \\ -\mathcal{R}_{c2}k & -(k^2 + 4) & 2k\psi_{12} \\ -k\theta_{12} & -k\psi_{12} & -16 \end{bmatrix}, \quad (\text{B.4})$$

where the values of ψ_{12} and θ_{12} are given by (4.10). Its characteristic equation is

$$\lambda^3 + [\sigma(k^2 + 4) + (k^2 + 20)]\lambda^2 + 16(k^2 + 4)(\mathcal{R}/\mathcal{R}_{c2} + \sigma)\lambda + 32\sigma(k^2 + 4)^2(\mathcal{R}/\mathcal{R}_{c2} - 1) = 0. \quad (\text{B.5})$$

The L_2 branch undergoes an in-subspace Hopf bifurcation at a Rayleigh number of \mathcal{R}_{H2} , as defined by expression (4.14).

The out-of-subspace stabilities of L_1 and L_2 are similar but not identical. There are five modes orthogonal to the L_2 subspace, but the θ_{02} mode is linearly uncoupled from the others and always stable. The linear stability of the remaining four modes, $\{\psi_{11}, \psi_{01}, \theta_{11}, \psi_{03}\}$, is governed by the matrix operator

$$\begin{bmatrix} -\sigma(k^2 + 1) & \frac{1}{2}k\frac{k^2+3}{k^2+1}\psi_{12} & \frac{\sigma k}{k^2+1} & -\frac{3}{2}k\frac{k^2-5}{k^2+1}\psi_{12} \\ -\frac{3}{4}k\psi_{12} & -\sigma & 0 & 0 \\ \mathcal{R}k & -\frac{1}{2}k\theta_{12} & -(k^2 + 1) & \frac{3}{2}k\theta_{12} \\ \frac{1}{4}k\psi_{12} & 0 & 0 & -9\sigma \end{bmatrix}. \quad (\text{B.6})$$

where the values of ψ_{12} and θ_{12} are given by (4.10). Like the L_1 branch, the L_2 branch never undergoes an out-of-subspace Hopf bifurcation, and it can undergo a pitchfork bifurcation at the Rayleigh number \mathcal{R}_{*2} defined by expression (4.12).

B.3 Degenerate L_2 branch of HK6

In the HK6 model, as in the HK8 model, the ψ_{12} and θ_{12} modes occur in the same ratio for all L_2 states: $\theta_{12}/\psi_{12} = -[k^2 + 4]^2/k$. However, their amplitudes are arbitrary, and the entire degenerate L_2 branch lies at a single Rayleigh number, \mathcal{R}_{c2} . One can still compute the linear stability of these degenerate states, but a mode amplitude must be used as a control parameter in place of \mathcal{R} .

The TC branch of HK6 emerges from L_1 at \mathcal{R}'_* , where (Howard and Krishnamurti, 1986)

$$\frac{\mathcal{R}'_*}{\mathcal{R}_c} - 1 = \frac{9\sigma^2}{k^2 + 1} \frac{k^4 + 5k^2 + 7}{(\sigma^2 + 3\sigma)(k^2 + 1)^2 + 3k^2(k^2 + 4)}. \quad (\text{B.7})$$

The starker difference between \mathcal{R}'_* in HK6 and \mathcal{R}_* is that the former exists for all σ and k , while the latter does not exist when both parameters are small. In Appendix B.6, we consider limiting behavior and see that \mathcal{R}'_* and \mathcal{R}_* are very similar in the large- k , small- σ limit, though still not identical. On the degenerate L_2 branch of the HK6 model, the pitchfork occurs when $\psi_{12} = \psi'_*$, where

$$\psi'^2_* = \frac{24\sigma^2}{1 + \sigma}. \quad (\text{B.8})$$

Like the L_1 pitchfork, this bifurcation occurs in the HK6 model for all parameters.

For given signs of ψ_{01} and ψ_{11} , the other four mode amplitudes are uniquely determined by the implicit expressions for the TC coordinates given by [Howard and Krishnamurti \(1986\)](#). The TC states thus must not undergo saddle-node bifurcations; there are no separate upper and lower branches. Since TC has no saddle-node and always connects to L_1 and L_2 , the HK6 model is always in regime 4 of Figure 4.3.

B.4 Hopf bifurcations

B.4.1 HK8

Just as we divided the σ - k^2 plane into five regimes according to the HK8 system's pitchfork bifurcations, so can we divide it based on the structure of Hopf bifurcations. In particular, we can ask whether or not Hopf bifurcations exist, and, if so, where they lie relative to the pitchfork bifurcations. The regimes in which the L_1 and L_2 Hopf bifurcations exist or do not exist are divided by the parameter curves along which the denominators of (4.13) and (4.14) vanish, respectively. However, these transitions are initially only relevant at very large \mathcal{R} , so they do not effect the TC states, which are our primary interest. More relevant to the TC states are the regime boundaries defined by $\mathcal{R}_* = \mathcal{R}_H$ and $\mathcal{R}_{*2} = \mathcal{R}_{H2}$. On these

two parameter curves, the in-subspace Hopf bifurcations of L_1 and L_2 , respectively, cross the out-of-subspace pitchfork bifurcations. Such collisions also coincide with the creation or destruction of a Hopf bifurcation on the TC branch. When the TC branch has a saddle-node, a Hopf bifurcation may emerge from it in a Bogdanov-Takens bifurcation, which defines still another regime boundary. And finally, when one end of the TC branch extends to infinity, Hopf bifurcations may appear or disappear on TC at infinity, further dividing parameter space. The result of all these distinctions is the division of the σ - k^2 parameter plane into six regimes, lettered A through F in the left-hand diagram of Figure B.1. These regimes correspond to the six possible configurations of Hopf bifurcations on the TC branch. In most regimes, the structure of Hopf bifurcations on TC uniquely determines the structure of Hopf bifurcations on L_1 and L_2 also. In regime D, however, there are three possibilities, defined by whether or not L_1 or L_2 undergo Hopf bifurcations beyond the TC connection points. Regime D is thus further divided into sub-regimes i, ii, and iii.

We can understand the transitions between different structures of Hopf bifurcations on TC by examining the left-hand diagram of Figure B.1 together with Figure B.2. In regime A, where σ is small and k^2 intermediate, the TC branch undergoes no Hopf bifurcations and is always unstable. As σ increases, a Hopf bifurcation appears on the TC branch, moving inward from infinite \mathcal{R} (regime B). A second Hopf bifurcation then appears on the lower TC branch, emerging from the saddle-node (regime C). The portion of the lower branch between the saddle-node and this new Hopf bifurcation is stable. Increasing σ or k^2 further, the Hopf bifurcation on the upper branch moves outward and vanishes, escaping either to L_1 or to infinity (regime D). (The upper branch depicted in regime D of Figure B.1 may or may not be present.) As σ increases into regime E, a second Hopf bifurcation appears on TC , emerging from the intersection with L_2 , if that intersection exists, or otherwise from infinity. As σ increases further (or k^2 decreases), the system may move from regime E to

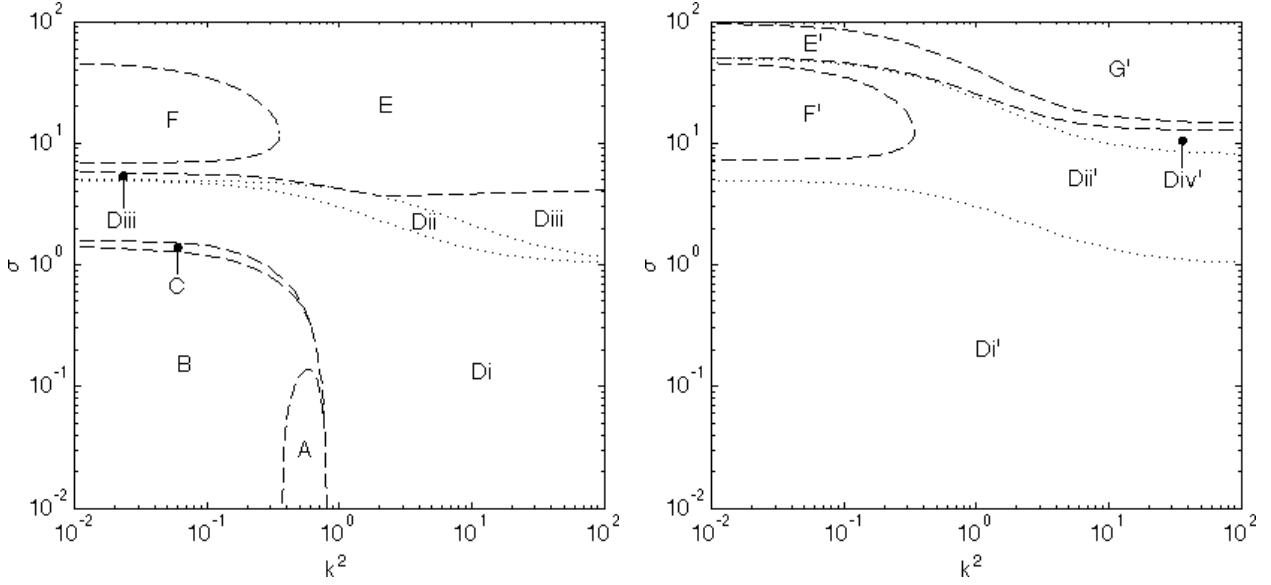


Figure B.1: Parameter regimes characterized by the structures of Hopf bifurcations in the HK8 (left) and HK6 (right) models. Dashed lines (---) separate regimes in which TC has different Hopf bifurcations. (The Hopf bifurcations on L_1 and L_2 may also differ between these regimes.) Dotted lines (----) separate sub-regimes differentiated only by the existence or non-existence of Hopf bifurcations on L_1 or L_2 beyond the TC connection points. The six possible structures of Hopf bifurcations on TC in the HK8 model are depicted schematically in Figure B.2, while all possible structures of Hopf bifurcations in the HK6 model are depicted in Figure B.3. Boundaries between subcritical and supercritical Hopf bifurcations are not shown.

regime F. In this transition, the left-hand Hopf bifurcation leaves TC by colliding with L_1 , resulting in an entirely unstable TC branch.

The subdivisions of regime D are as follows. In regime Di, neither L_1 nor L_2 undergo Hopf bifurcations. Entering regime Dii, a Hopf bifurcation appears on L_1 , coming in from infinite \mathcal{R} and thus falling beyond the intersection with TC . Entering regime Diii, a Hopf bifurcation appears on L_2 at infinity, so both L_1 and L_2 undergo Hopf bifurcations after their intersections with TC . These transitions are not crucial to the study of states with zonal flow, but they elucidate the origins of Hopf bifurcations that, in other transitions, affect TC when they cross the pitchforks at \mathcal{R}_* and \mathcal{R}_{*2} .

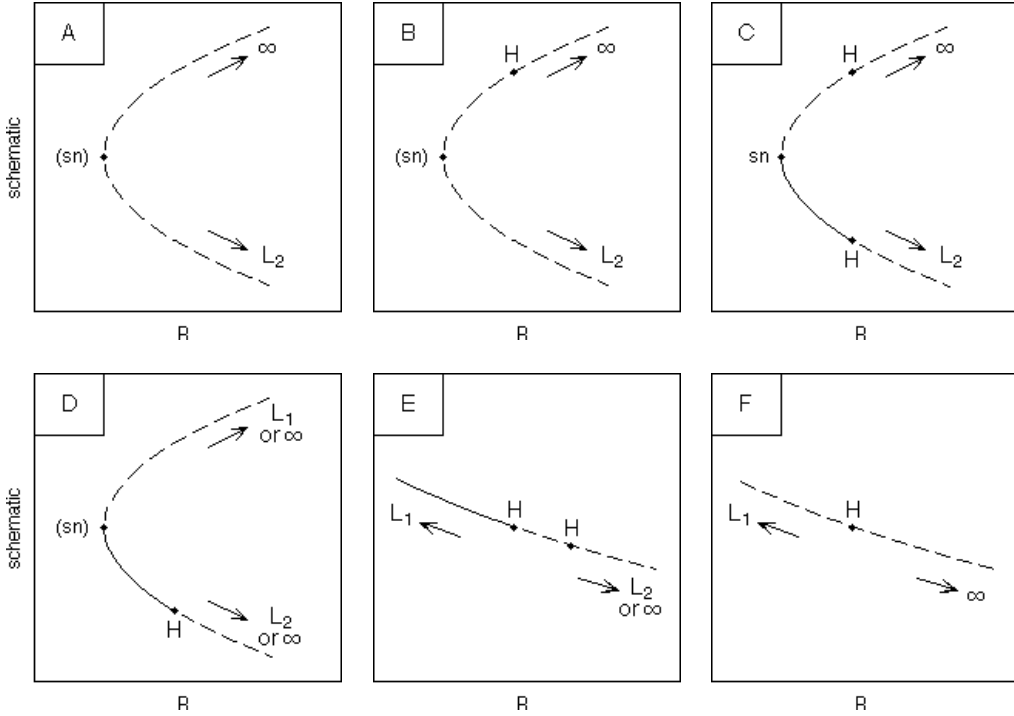


Figure B.2: Schematic bifurcation diagrams showing the six possible structures of Hopf bifurcations on TC in the HK8 model. The lettering of the different structures corresponds to the lettered σ - k^2 parameter regimes in the left-hand diagram of Figure B.1. Stable (—) and unstable (---) states are shown. Pitchfork, saddle-node, and Hopf bifurcations are labeled by pf, sn, and H, respectively. Parentheses around the saddle-node indicate that it may or may not be present, depending on the pitchfork regime in which the system falls (cf. Figure 4.3). When the saddle-node is present, Hopf bifurcations lie on the upper or lower TC branches as drawn. In each regime, it is indicated whether the ends of the TC branch may terminate (at L_1 or L_2) or extend to infinity.

B.4.2 HK6

We have mentioned that the HK6 model displays only one structure of pitchfork bifurcations (regime 4), as opposed to five possible structures in the HK8 model. The structures of Hopf bifurcations in the HK6 model are not quite so minimal. In the right-hand diagram of Figure B.1, the σ - k^2 plane is divided into four main regimes, defined according to the Hopf bifurcations of TC in the HK6 model. Schematic bifurcation diagrams representing each regime (and sub-regime) are shown in Figure B.3. Regimes D, E, and F in the HK8 model

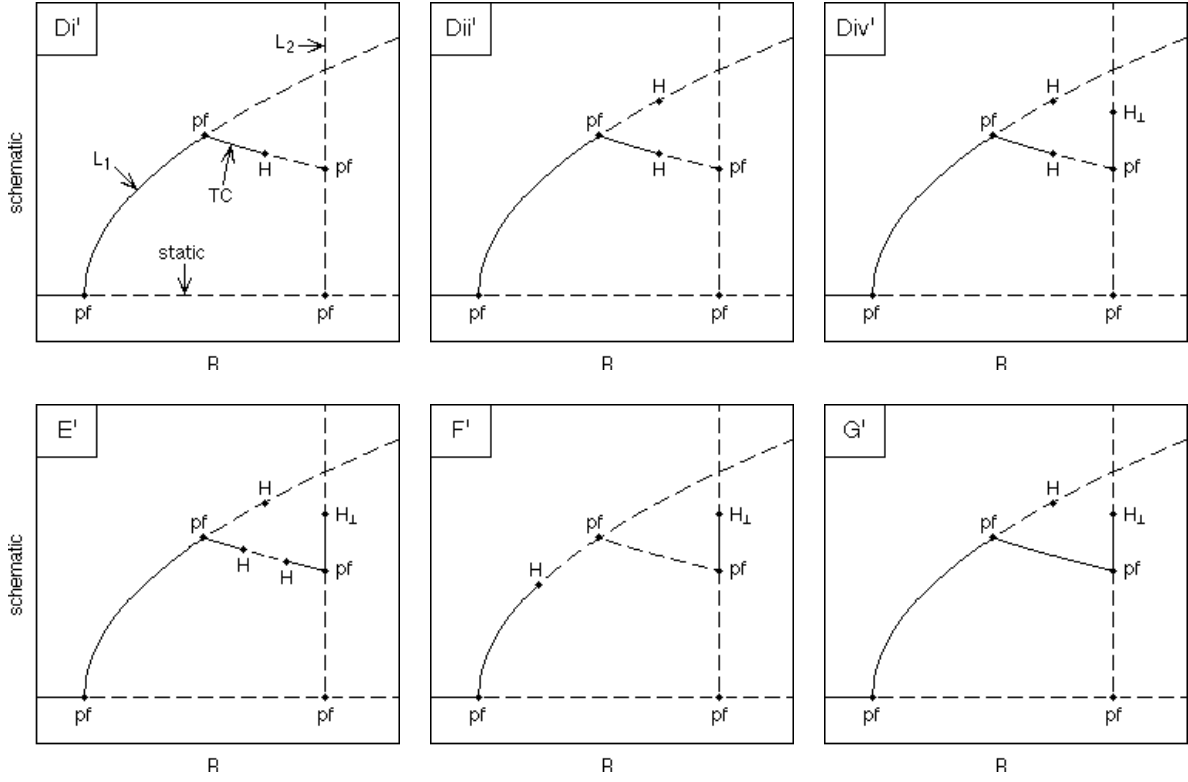


Figure B.3: Schematic bifurcation diagrams showing the six possible structures of Hopf bifurcations in the HK6 model. The lettering of the different structures corresponds to the lettered σ - k^2 parameter regimes in the right-hand diagram of Figure B.1. Stable (—) and unstable (---) states are shown. Pitchfork, saddle-node, and Hopf bifurcations are labeled by pf, sn, and H, respectively. The out-of-subspace Hopf bifurcation of L_2 , which we argue is unphysical (see text), is labelled as H_\perp .

have analogues in the HK6 model, labelled in Figure B.1 as D', E', and F'. Regimes A, B and C have no analogues in the HK6 model, this portion of parameter space all being occupied by regime D'. The boundary of the HK6 regime F' is only slightly different than the boundary of the HK8 regime F; this boundary is defined by $\mathcal{R}_* = \mathcal{R}_H$, and the value of \mathcal{R}_H is the same in the two models, while the inclusion of ψ_{03} affects \mathcal{R}_* only weakly at the large values of σ where \mathcal{R}_* and \mathcal{R}_H coincide. In the limit of small Prandtl number and large wavenumber, where the reduced models are most faithful to the PDE, the HK8 and HK6 models both display the same structures of local bifurcations — regimes 4Di and 4Di', respectively.

Two intriguing behaviors of the HK6 model are absent from the HK8 model, suggesting that they are artifacts of the non-conservative truncation and do not reflect real behaviors of the PDE. Firstly, at large σ , the TC branch of the HK6 model enters the regime G' depicted in Figure B.3. The entire *TC* branch is stable in this regime, bifurcating supercritically from the stable L_1 branch and undergoing no local bifurcations until it intersects L_2 . There is no analogous regime in the HK8 system (cf. Figure B.1), where at most a part of the *TC* branch can be stable. Secondly, the L_2 branch of the HK6 model may undergo a Hopf bifurcation in the *out-of-subspace* direction, denoted by H_\perp in the bifurcation diagrams of Figure B.3, that stabilizes a section of L_2 . The H_\perp bifurcation emerges from the L_2 pitchfork as the system transitions from regime Dii' to regime Div', which has no analog in the HK8 system. This structure is unexpected not only because the L_2 solutions gain stability, but also because the out-of-subspace Hopf bifurcations at H_\perp beget branches of limit cycles whose direction of zonal flow reverses over a period. Such zonal-flow-reversing oscillations have previously been found only as a result of global gluing bifurcations (Rucklidge and Matthews, 1996), rather than bifurcating directly from a steady state without zonal flow. As the domain becomes asymptotically narrow, the H_\perp bifurcation moves unboundedly up the degenerate L_2 branch, so it does not appear in the narrow-HK6 system at leading order. Rucklidge and Matthews (1996) are thus correct in stating that zonal-flow-reversing limit cycles do not emerge from steady symmetric rolls in the narrow-HK6 system, but this is no longer true when the horizontal period is finite. Not only can the HK6 system's L_2 branch undergo the out-of-subspace Hopf bifurcation that is likely unphysical, but it also lacks the *in-subspace* Hopf bifurcation that *is* physical.

B.5 Complete classification of local bifurcations of steady states

We have identified the five basic ways in which TC may connect to L_1 or L_2 in the HK8 system (regimes 1 through 5), and we have identified the six possible structures of Hopf bifurcations on the TC branch (regimes A through F). Considering both together, the possible structures of local bifurcations on the TC branch divide the σ - k^2 parameter plane into twelve regimes, as depicted in Figure B.4. In that Figure we have also included the three sub-regimes of D that correspond to the existence or non-existence of Hopf bifurcations on L_1 and L_2 , bringing the total number of regimes to sixteen. These sixteen regimes constitute a complete classification of the local bifurcations of steady states in the HK8 model, excluding the distinction between subcritical and supercritical Hopf bifurcations. If one added to Figure B.4 the parameter curves defined by generalized Hopf bifurcations, in which Hopf bifurcations transition between sub- and supercriticality, the classification would become significantly more complicated. We have found four such curves for the TC Hopf bifurcations alone (not shown), and there are likely more.

Schematic bifurcation diagrams for each of the twelve possible bifurcation structures of TC (cf. Figure B.4) are shown in Figures B.5 through B.9. Figure B.5 illustrates the possible structures of regime 1 (1A and 1B), Figure B.6 illustrates the possible structures of regime 2 (2A, 2B, 2C, and 2D), and so forth. From these diagrams we can glean a few generalities about the TC branch. Evidently, the TC branch may undergo zero, one, or two Hopf bifurcations. (More precisely, each of the four symmetry-related TC branches will undergo these bifurcations.) The entire TC branch is never stable, but it can have stable sections in regimes 2 through 5, though not in regime 1. When both upper and lower TC branches exist, only the lower branch may have a stable section, and this stable section must overlap, at least partly, with stable L_1 states. Such overlap implies hysteresis between steady states

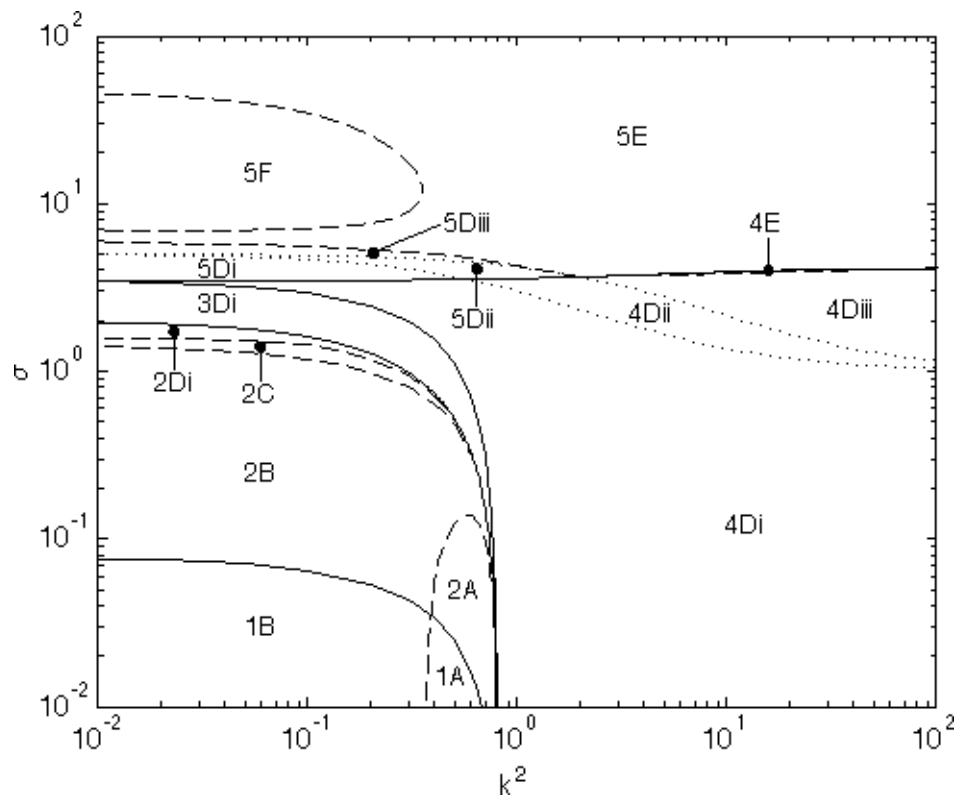


Figure B.4: The sixteen parameter regimes defined by considering together the possible structures of pitchfork bifurcations (regimes 1 through 5) and Hopf bifurcations (regimes A though F, with three sub-regimes of D) along branches of steady states in the HK8 model. Solid lines (—) separate different structures of pitchfork bifurcations, dashed lines (---) separate different structures of Hopf bifurcations on TC , and dotted lines (----) separate sub-regimes defined only by the existence or non-existence of Hopf bifurcations on L_1 and L_2 . Omitting the dotted lines leaves twelve regimes, corresponding to the possible bifurcation structures of the TC branch alone. Bifurcation diagrams depicting these twelve TC structures appear in Figures B.5 through B.9.

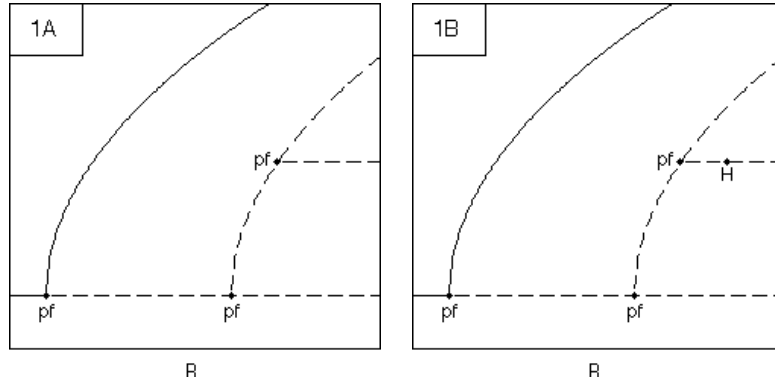


Figure B.5: Schematic bifurcations diagrams showing the two possible structures of Hopf bifurcations on the TC branch in regime 1 of the HK8 model (cf. Figure B.4). Stable (—) and unstable (---) steady states are shown, and pitchfork (pf) and Hopf (H) bifurcations are labeled. In this Figure and the next four, the four steady branches — the static state, L_1 , L_2 , and TC — are as labelled in Figure 4.3.

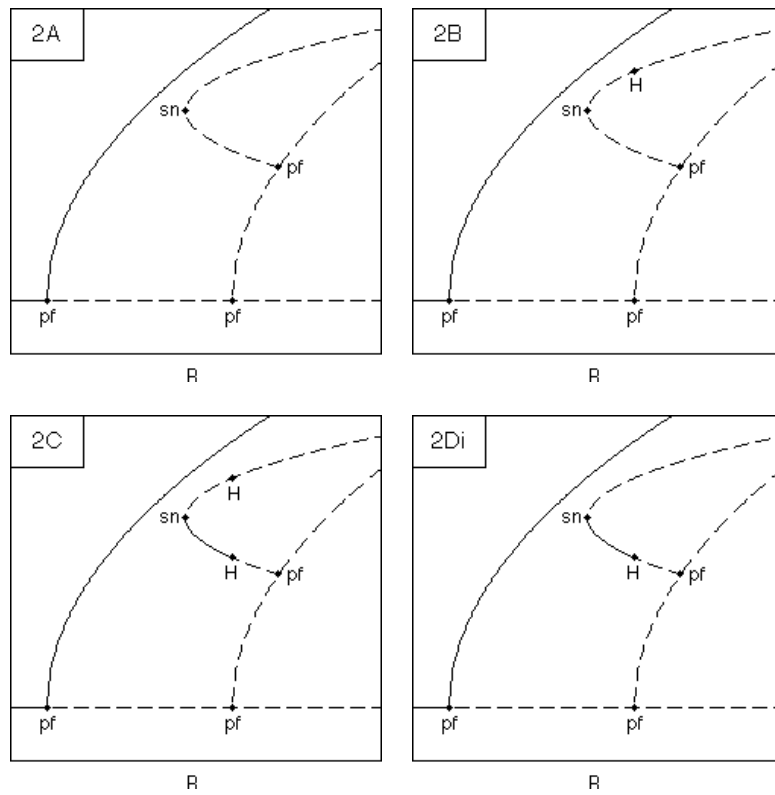


Figure B.6: Schematic bifurcations diagrams showing the four possible structures of Hopf bifurcations on the TC branch in regime 2 of the HK8 model (cf. Figure B.4). Stable (—) and unstable (---) steady states are shown, and pitchfork (pf), Hopf (H), and saddle-node (sn) bifurcations are labeled.

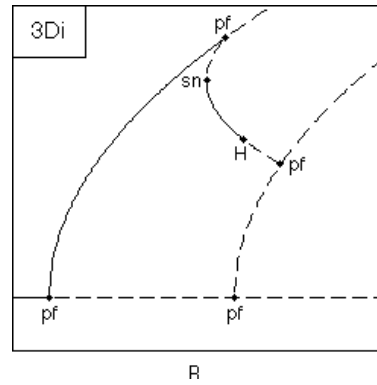


Figure B.7: Schematic bifurcations diagram showing the unique structure of Hopf bifurcations in regime 3 of the HK8 model (cf. Figure B.4). Stable (—) and unstable (---) steady states are shown, and pitchfork (pf), Hopf (H), and saddle-node (sn) bifurcations are labeled.

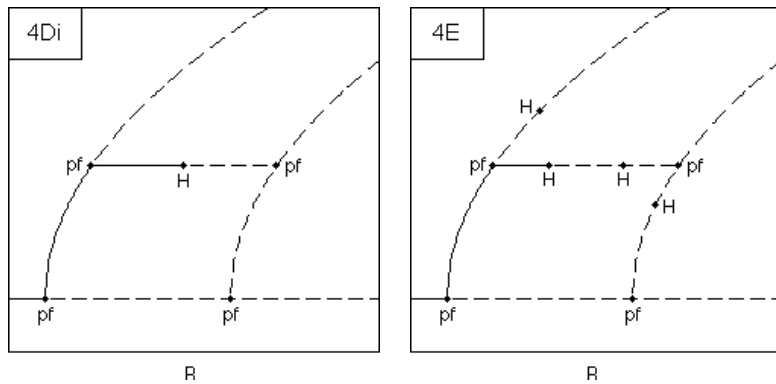


Figure B.8: Schematic bifurcations diagrams showing the two possible structures of Hopf bifurcations on the TC branch in regime 4 of the HK8 model (cf. Figure B.4). Stable (—) and unstable (---) steady states are shown, and pitchfork (pf) and Hopf (H) bifurcations are labeled. In regime 4Dii (not shown), there is an additional Hopf bifurcation on L_1 past its intersection with TC . In regime 4Diii, (not shown), there are additional Hopf bifurcations on both L_1 and L_2 past their intersections with TC .

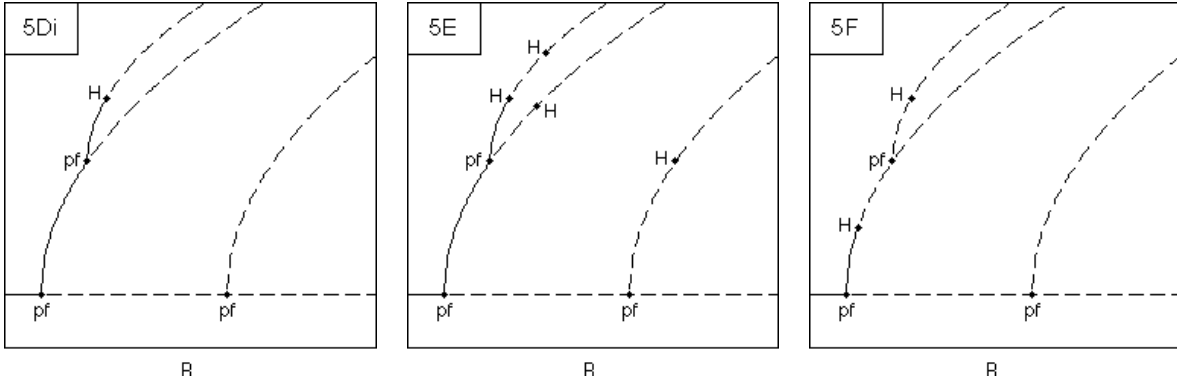


Figure B.9: Schematic bifurcation diagrams showing the three possible structures of Hopf bifurcations on the TC branch in regime 5 of the HK8 model (cf. Figure B.4). Stable (—) and unstable (---) steady states are shown, and pitchfork (pf), Hopf (H), and saddle-node (sn) bifurcations are labeled. In regime 5Dii (not shown), there is an additional Hopf bifurcation on L_1 past its intersection with TC . In regime 5Diii, (not shown), there are additional Hopf bifurcations on both L_1 and L_2 past their intersections with TC .

with and without zonal flow. This is the type of bifurcation structure that produces the bistable PDE solutions of Figure 2.2 in the previous Chapter.

The TC branches depicted in Figures B.5 through B.9 have stable sections in a number of regimes, whereas we saw in the last Chapter that their counterparts in the full PDE are more often completely unstable. This is because TC states of the PDE with a particular horizontal period may be linearly unstable to perturbations by shorter or longer wavelengths, while such modes have been excluded from the HK8 model by design. In particular, the TC states of the PDE we found were always unstable to perturbations by *longer* wavelengths, indicating that wide horizontal periods are dynamically selected.

Given the existence of chaotic flows without zonal flow, it is natural to ask whether they can persist as the Rayleigh number is increased, or whether the onset of zonal flow is inevitable. Even in the context of the HK8 model, this is difficult to answer with certainty — it amounts to determining the stability of the Lorenz attractor to shearing perturbations. However, one might reasonably expect that the latter is similar to the stability of the L_1 fixed point to shearing perturbations, which we know. In regime 5F, the L_1 states lose stability

first to perturbations without zonal flow, but the eigenvalue governing their stability to shearing perturbations increases fastest as $\mathcal{R} \rightarrow \infty$. Thus, the perturbations to which L_1 states are *most unstable* at large \mathcal{R} will contain zonal flow. If the Lorenz attractor behaves at all similarly, states that begin on the Lorenz attractor will ultimately develop zonal flow as \mathcal{R} is increased. This is consistent with our numerical integration of the HK8 model in regime 5F, and, as reported in Chapter 5, PDE solutions appear to also develop zonal flow inevitably as Ra is raised without bound.

Implications for the narrow-HK6 model We have seen that the HK6 and HK8 models assume the same steady bifurcation structure (regime 4Di) for sufficiently small σ and large k . However, as σ increases or k decreases, the HK8 system enters regimes that are not captured by the HK6 system. Even in the narrow-period limit, steady solutions of the HK6 and HK8 systems have different bifurcation structures when σ exceeds 1, and the two systems differ in their global bifurcations at still smaller σ . In light of these differences, we can anticipate that the sixth-order narrow-HK8 model will behave differently from the fourth-order narrow-HK6 model, even when σ is fairly small (but finite). The study of the narrow-HK6 system by [Rucklidge and Matthews \(1996\)](#) is quite thorough and goes much deeper than our present study of the larger HK8 system. Many of their conclusions likely apply to the narrow-HK8 system also, but a few may be artifacts of the HK6 truncation's flaws. Among other results, [Rucklidge and Matthews \(1996\)](#) computed the partial unfolding of \mathcal{R}_* from \mathcal{R}_c as σ increases from zero. Computing the analogous unfolding for the narrow-HK8 system would reveal much about the similarities and differences between the two models.

B.6 Limiting cases

Since the HK8 model is most informative about the full PDE when σ is small or k is large, it is useful to consider these two limits. A naive interpretation of Figure B.4 suggests that the regimes 4Di, 4Diii, and 5E will exist when $k \gg 1$, while the regimes 4Di, 1A, and 1B will exist when $\sigma \ll 1$. In actuality, certain bifurcations escape to infinity at leading order, so we must examine the limiting cases of our various analytical results to determine what regimes will exist.

B.6.1 Short wavelengths ($k \gg 1$)

The limit in which the horizontal period becomes narrow is the most convenient limit mathematically, but its physical relevance is questionable. In a physically realizable domain with a periodic direction, such as an annulus, the periodic direction is by geometric necessity not narrow. The short-wavelength limit is thus relevant only if narrow rolls are dynamically selected before the onset of zonal flow, and we have already seen in the last Chapter that this is not typically the case. [Additional physical effects, such as magnetism (Rucklidge and Matthews, 1996), may narrow the selected rolls, thereby making the $k \gg 1$ limit more relevant.] Furthermore, the HK8 model predicts that the first wavenumbers to become unstable to zonal flow as the Rayleigh number is raised are between $k^2 = 4/5$ and $k^2 = 2$, depending on the Prandtl number. Such wavenumbers are a bit larger than those of typically-selected rolls, but they are still not in the $k \gg 1$ regime. These facts cast doubt on the physical relevance of the narrow-HK6 and narrow-HK8 models. Still, considering the $k \gg 1$ limit lets us make contact with past studies (Hughes and Proctor, 1990; Rucklidge and Matthews, 1996) and helps us understand the HK8 model.

In the $k \gg 1$ limit, the L_1 and L_2 branches bifurcate, respectively, at $\mathcal{R}_c \sim k^4 + 3k^2$ and $\mathcal{R}_{c2} \sim k^4 + 64k^2$. The distance between \mathcal{R}_c and \mathcal{R}_{c2} increases with k^2 , but it decreases

relative to their own magnitudes:

$$\frac{\mathcal{R}_{c2}}{\mathcal{R}_c} - 1 \sim 61k^{-2}. \quad (\text{B.9})$$

That is to say, \mathcal{R}_c and \mathcal{R}_{c2} do not converge, but they are asymptotic. The TC branch bifurcates supercritically from L_1 (at \mathcal{R}_*) for all values of σ . The value of \mathcal{R}_* is also asymptotic, and not generally convergent, to \mathcal{R}_c :

$$\frac{\mathcal{R}_*}{\mathcal{R}_c} - 1 \sim \frac{27\sigma^2}{3\sigma^2 + 10\sigma + 10} k^{-2}. \quad (\text{B.10})$$

This pitchfork is farthest from \mathcal{R}_c when $\sigma \gg 1$. Taking this limit in addition to $k \gg 1$ yields $\mathcal{R}_*/\mathcal{R}_c - 1 \sim 9k^{-2}$, which is still below \mathcal{R}_{c2} . The pitchfork bifurcation is closest to the primary instability at \mathcal{R}_c when $\sigma \ll 1$, in which case $\mathcal{R}_*/\mathcal{R}_c - 1 \sim \frac{27}{10}\sigma^2 k^{-2}$. In the distinguished limit where $\sigma k \ll 1$, \mathcal{R}_* is not only asymptotic to \mathcal{R}_c but also converges to \mathcal{R}_c as $k \rightarrow \infty$. The prefactor of 27/10 that appears in the limit of narrow rolls and small Prandtl number is slightly below 3, which is the prefactor that appears in analogous limit of HK6 ([Hughes and Proctor, 1990](#); [Rucklidge and Matthews, 1996](#)). So, even in the limit where both reduced models are expected to be most faithful to the PDE, there are slight quantitative differences. Hence, the unfolding of \mathcal{R}_* from \mathcal{R}_c as σ increases from zero that [Rucklidge and Matthews \(1996\)](#) computed for the narrow-HK6 model would be different if repeated for the narrow-HK8 model, though the qualitative importance of these differences cannot be guessed in advance.

The Rayleigh number at which TC intersects L_2 reduces in the $k \gg 1$ limit to

$$\frac{\mathcal{R}_{*2}}{\mathcal{R}_{c2}} - 1 \sim \frac{27\sigma^2}{-3\sigma^2 + 10\sigma + 10} k^{-2}. \quad (\text{B.11})$$

This intersection exists only when $\sigma < \frac{1}{3}(5 + \sqrt{55}) \approx 4.138$, in which case the system is in regime 4 (cf. Figure 4.3). Otherwise, it is in regime 5. The in-subspace Hopf bifurcations of L_1 and L_2 occur in the $k \gg 1$ limit at

$$\frac{\mathcal{R}_H}{\mathcal{R}_c} - 1 \sim \frac{(\sigma + 1)^2}{\sigma - 1} \quad (\text{B.12})$$

$$\frac{\mathcal{R}_{H2}}{\mathcal{R}_{c2}} - 1 \sim \frac{(\sigma + 1)^2}{\sigma - 1} \quad (\text{B.13})$$

when $\sigma > 1$, and they do not exist otherwise. Unlike \mathcal{R}_* , \mathcal{R}_H is not asymptotic to \mathcal{R}_c in this limit and will not affect the initial development of zonal flow. Indeed, the narrow-HK6 and narrow-HK8 models are scaled to capture behavior asymptotically close to the static state, so, at leading order, the Hopf bifurcations will not enter these models at all. Figure B.4 indicates that when σ is increased and the system moves from regime 4 to 5, it moves from regime D to E concurrently. In this latter transition, a second Hopf bifurcation appears on the TC branch when \mathcal{R}_{*2} increases past \mathcal{R}_{H2} . However, since \mathcal{R}_{H2} is not captured in the narrow-HK8 model (because it is not asymptotically near \mathcal{R}_{c2}), the appearance of this second Hopf bifurcation on TC is also not captured. The narrow-HK8 system is thus always in either regime 4Di or 5Di, in contrast to what Figure B.4 may seem to suggest.

The narrow-HK8 model The dynamics of the HK8 model occur, at leading order, on a six-dimensional slow manifold when $k \gg 1$. The HK8 model can thus be replaced by the sixth-order narrow-HK8 model. We accomplish this with the same scaling that reduces the sixth-order HK6 model to the fourth-order narrow-HK6 model (Hughes and Proctor, 1990; Rucklidge and Matthews, 1996)¹: $\psi \sim k^{-1}$ and $\theta \sim k^2$. This scaling is designed to capture

¹The truncated ODE with which Rucklidge and Matthews (1996) begin their reduction are derived from the more usual nondimensionalization of the Boussinesq equations given in (1.8)-(1.10), so they differ from the usual form of the HK6 equations that we use (Howard and Krishnamurti, 1986; Hughes and Proctor, 1990). The ODE of Rucklidge and Matthews (1996) can be obtained from (4.6) by scaling the θ modes by $1/R$ and reversing the signs of the three L_1 modes, but the resulting reduced system is the same whether or not θ is rescaled first.

the HK8 system near the pithfork at \mathcal{R}_* . The rationale is that $\mathcal{R}_* - \mathcal{R}_c = O(k^2)$, according to (B.10), so one wants to look at Rayleigh numbers for which $\mathcal{R} - \mathcal{R}_c = O(k^2)$. The L_1 and L_2 states defined by (4.9) and (4.9) then have wavenumber modes of order k^{-1} and temperature modes of order k^2 , the chosen scaling.

To obtain the narrow-HK8 model, let us define order-one scaled variables as $\Psi := k\psi$ and $\Theta := k^{-2}\theta$, along with μ , the supercriticality of \mathcal{R} , as $\mathcal{R} - \mathcal{R}_c := \mu k^2$. At $O(k^2)$, the HK8 equations (4.6) require $\Psi_{11} \sim \Theta_{11}$ and $\Psi_{12} \sim -\Theta_{12}$. The $O(k^2)$ terms can then be removed from the evolution equations by taking the linear combinations $\dot{\Psi}_{11} + \sigma\dot{\Theta}_{11}$ and $\dot{\Psi}_{12} - \sigma\dot{\Theta}_{12}$. The resulting relations are $O(1)$ at leading order. Replacing Θ_{11} by Ψ_{11} and Θ_{12} by $-\Psi_{12}$ in these relations yields

$$(1 + \sigma)\dot{\Psi}_{11} = \mu\sigma\Psi_{11} + \frac{1}{2}(1 + \sigma)\Psi_{01}\Psi_{12} - \frac{3}{2}(1 + \sigma)\Psi_{03}\Psi_{12} - \sigma\Psi_{11}\Theta_{02} \quad (\text{B.14})$$

$$(1 + \sigma)\dot{\Psi}_{12} = (\mu - 9)\sigma\Psi_{12} - \frac{1}{2}(1 + \sigma)\Psi_{01}\Psi_{11} + \frac{3}{2}(1 + \sigma)\Psi_{03}\Psi_{11} - 2\sigma\Psi_{12}\Theta_{04}. \quad (\text{B.15})$$

Completing the system with the other four evolution equations at leading order yields the narrow-HK8 model,

$$\begin{array}{lcl} \dot{\Psi}_{11} & = & \mu \frac{\sigma}{1+\sigma} \Psi_{11} + \frac{1}{2} \Psi_{01} \Psi_{12} - \frac{\sigma}{1+\sigma} \Psi_{11} \Theta_{02} \\ \dot{\Psi}_{01} & = & -\sigma \Psi_{01} - \frac{3}{4} \Psi_{11} \Psi_{12} \\ \dot{\Psi}_{12} & = & (\mu - 9) \frac{\sigma}{1+\sigma} \Psi_{12} - \frac{1}{2} \Psi_{01} \Psi_{11} \\ \dot{\theta}_{02} & = & -4\Theta_{02} + \frac{1}{2} \Psi_{11}^2 \\ \dot{\Psi}_{03} & = & -9\sigma \Psi_{03} + \frac{1}{4} \Psi_{11} \Psi_{12} \\ \dot{\Theta}_{04} & = & -16\Theta_{04} + \Psi_{12}^2. \end{array} \quad (\text{B.16})$$

The dashed box contains the narrow-HK6 model studied by Rucklidge and Matthews (1996).

As anticipated, the TC branch of the narrow-HK8 model undergoes a single Hopf bifurcation at all Prandtl numbers. The Hopf bifurcation is subcritical, meaning the emergent

limit cycles are initially unstable, when σ is in the intervals $(0, 0.3827)$ or $(3.753, 104.8)$, and it is supercritical for σ in $(0.3827, 3.753)$ or $(104.8, \infty)$. These intervals are divided by generalized Hopf bifurcations, also called Bautin bifurcations.

B.6.2 Small Prandtl numbers ($\sigma \ll 1$)

We now consider the limit of small Prandtl numbers, $\sigma \ll 1$. It appears that past authors have considered this limit only in conjunction with $k \gg 1$, but the limit is also of interest for finite horizontal periods since the HK8 model captures the connection between L_1 and TC in the PDE at finite wavenumbers when σ is small.

Neither L_1 nor L_2 undergoes a Hopf bifurcation when σ is small. The TC branch always bifurcates from the L_2 branch at a Rayleigh number of

$$\frac{\mathcal{R}_{*2}}{\mathcal{R}_{c2}} - 1 \sim \frac{27}{2} \frac{k^4 + 5k^2 + 7}{(k^2 + 4)(k^2 + 1)(5k^2 + 11)} \sigma^2. \quad (\text{B.17})$$

When $k^2 > 4/5$, meaning the aspect ratio of the domain is smaller than $A \approx 2.24$, the TC branch bifurcates subcritically from L_2 and connects to L_1 in a supercritical pitchfork at

$$\frac{\mathcal{R}_*}{\mathcal{R}_c} - 1 \sim \frac{27}{2} \frac{k^4 + 5k^2 + 7}{(k^2 + 4)(k^2 + 1)(5k^2 - 4)} \sigma^2, \quad (\text{B.18})$$

That is, the system is in regime 4 of Figure 4.3. When $k^2 < 4/5$, on the other hand, the TC branch bifurcates supercritically from L_2 and extends to infinity (regime 1 of Figure 4.3). As σ approaches zero with the wavenumber fixed, \mathcal{R}_{*2} converges to \mathcal{R}_{c2} . When $k^2 > 4/5$, \mathcal{R}_* converges to \mathcal{R}_c also; otherwise, \mathcal{R}_* does not exist. Unlike the large-wavenumber limit, \mathcal{R}_c and \mathcal{R}_{c2} do not converge asymptotically in the small- σ limit.

Because $\mathcal{R}_* \rightarrow \mathcal{R}_c$ when $\sigma \rightarrow 0$ in the narrow-HK6 model, [Rucklidge and Matthews \(1996\)](#) were able to compute the unfolding of \mathcal{R}_* from \mathcal{R}_c in that system. Similar unfolding

diagrams could be computed with the full HK8 model for finite wavenumbers, so long as $k^2 > 4/5$. (At smaller k , \mathcal{R}_* does not exist in the small- σ limit.)

B.6.3 Small- σ limit of the narrow-HK6 model

The small- σ scaling that [Hughes and Proctor \(1990\)](#) used to further reduce the narrow-HK6 model can also be used to reduce the narrow-HK8 model:

$$\Psi \mapsto \sigma\Psi \quad \Theta \mapsto \sigma^2\Theta \quad t \mapsto \sigma^{-1}t. \quad (\text{B.19})$$

The result is a fourth-order model,

$$\begin{aligned} \dot{\Psi}_{01} &= -\Psi_{01} - \frac{3}{4}\Psi_{11}\Psi_{12} \\ \dot{\Psi}_{03} &= -9\Psi_{03} + \frac{1}{4}\Psi_{11}\Psi_{12} \\ \dot{\Psi}_{11} &= \frac{1}{1+\sigma}(\mu - \frac{1}{8}\sigma^2\Psi_{11}^2)\Psi_{11} + \frac{1}{2}\Psi_{01}\Psi_{12} - \frac{3}{2}\Psi_{03}\Psi_{12} \\ \dot{\Psi}_{12} &= \frac{1}{1+\sigma}(\mu - 9 - \frac{1}{8}\sigma^2\Psi_{12}^2)\Psi_{12} - \frac{1}{2}\Psi_{01}\Psi_{11} + \frac{3}{2}\Psi_{03}\Psi_{11}. \end{aligned} \quad (\text{B.20})$$

The $O(\sigma^2)$ terms in the above system must be kept to retain the L_1 and L_2 fixed points and prevent unbounded growth of Ψ_{11} and Ψ_{12} . As a result, the derivation is not formally consistent since other terms beyond zeroth order have been neglected. This four-dimensional model conserves the truncated vorticity in the dissipationless limit, unlike the three-dimensional model of [Hughes and Proctor \(1990\)](#), because the ψ_{03} mode has been added. Not having studied this model in detail, however, we cannot say whether this conservation alters their conclusions.

Appendix C

Appendix to Chapter 5: Computational methods

The Boussinesq equations were integrated using the `nek5000` spectral element code ([Fisher et al., 2013](#)), configured for second-order variable time stepping with a target Courant number of 0.5. Visualizations were created using VisIt ([Childs et al., 2011](#)). Most simulations were run in parallel on 256 processors of an IBM Blue Gene/P computer. Time averages were deemed converged at a time, τ , when they differed by less than 0.5% from their values at $\tau/2$. In the strongly oscillating flows that occur when $\sigma = 1$, averages were taken only over integer numbers of oscillations. This was managed by aligning the start and end times of averages with local maxima of $E(t)$. Spatial meshes were deemed converged when increasing the polynomial order of each element by 2 produced a change of less than than 1% in $\langle wT \rangle$.

Each mesh was composed of square, uniform elements. Most simulations were performed in a domain of aspect ratio $A = 2$ with 64 elements in the vertical and 32 in the horizontal. Elements of polynomial order 8 were needed with $\sigma = 10$ and $Ra = 2 \cdot 10^8$, but elements of order 6 or 4 sufficed at smaller Rayleigh numbers. The resolutions needed for our simulations to converge are coarser than one would need in non-shearing convection at similar Rayleigh

numbers. This is because shear dispersion effectively increases the viscosity and thermal diffusivity of the fluid in the shearing convection, which increases the size of the smallest coherent structures present in the flow.

The four largest- Ra Nusselt numbers given for $\sigma = 1$ in Figure 5.9 were not obtained using `nek5000` but were instead simulated by H. Johnston in collaboration with us, using a spectral collocation method described in [Johnston and Doering \(2009\)](#). The mean Nusselt numbers computed by H. Johnston agree with our own nearly to plotting accuracy at smaller Ra . Disparity arises at $Ra = 5 \cdot 10^7$, which we attribute to our own under-resolution, as the simulations of H. Johnston employ up to 512 modes in the vertical and 1024 in the horizontal. The particular difficulty in obtaining well converged time averages when $\sigma = 1$ is due to the strongly nonlinear oscillations. The period of a single oscillation is much longer than the timescales on which the fast dynamics occur, so many time steps — perhaps hundreds of thousands — are needed to simulate a single oscillation. And since each oscillation is different, as many as one hundred oscillations may be needed for integral quantities to converge.

Appendix D

Appendix to Chapter 6

D.1 Integral bounds

D.1.1 Proof that $T > 0$ on the interior

Let Ω be an open, bounded domain in any number of spatial dimensions. Assume T remains smooth on Ω for all $t \geq 0$, that it vanishes on the boundary of Ω , and that $T > 0$ everywhere on the interior of Ω at the initial time, $t = 0$. To prove the result by contradiction, suppose that $T < 0$ on an interior point at some positive time. There then must exist a minimum time, t_0 , at which T crosses zero and at least one interior point, x_0 , at which this occurs. That is, $T \geq 0$ everywhere when $t \leq t_0$, but $T < 0$ everywhere on some neighborhood of x_0 for some time interval, (t_0, t_1) . However, T attains a spatial minimum at (x_0, t_0) , so $\mathbf{u} \cdot \nabla T = 0$ and $\nabla^2 T \geq 0$, from which (1.10) implies $\partial_t T(x_0, t_0) > 0$. Hence, T will be positive at x_0 as soon as t exceeds t_0 , a contradiction.

D.1.2 Proof that $0 < \langle T \rangle \leq 1/12$

The nonnegativity of $\langle T \rangle$ follows easily from (6.13). If we also assume regularity of T , meaning smooth temperature solutions exist for all time, then the result of Appendix D.1.1 applies to give strict positivity of $\langle T \rangle$. (With much more effort, the background method analysis of Lu et al., 2004, gives a better lower bound for all but the smallest values of R .)

To obtain the upper bound, we integrate $z^2 \cdot$ (1.10) to find

$$\langle T \rangle = \frac{1}{12} - \langle zwT \rangle. \quad (\text{D.1})$$

It thus suffices to show that $\langle zwT \rangle$ is nonnegative. Integrating the continuity equation over the horizontal and using the side boundary conditions gives $\bar{w}(z) \equiv 0$, from which it follows that $\langle zwT \rangle = \langle zw\theta \rangle$, where θ is the deviation of T from the conductive profile, \tilde{T} . The PDE governing θ is

$$\partial_t \theta + \mathbf{u} \cdot \nabla \theta - zw = \Delta \theta,$$

and integrating this equation against θ gives $\langle zw\theta \rangle = \langle |\nabla \theta|^2 \rangle$, which is nonnegative. Thus, $\langle T \rangle \leq 1/12$.

D.1.3 Proof that $0 \leq \langle wT \rangle \leq 1/2$

The nonnegativity of $\langle wT \rangle$ for positive R follows directly from (6.14). To obtain the upper bound, we assume regularity of T . Then, positivity of T on the interior (*c.f.* Appendix D.1.1) implies $\bar{T}'_B \geq 0$ and $\bar{T}'_T \leq 0$. The latter inequality in conjunction with Equation (6.8) requires that $\bar{T}'_T \geq -1$ as well. Applied to Equation (6.9), the lower bounds on \bar{T}'_B and \bar{T}'_T together give $\langle wT \rangle \leq 1/2$.

D.2 Computational methods

The nek5000 code (Fisher et al., 2013) was run largely as described in Appendix C, with a few differences. Spatiotemporal averages were deemed converged at a time, τ , when the cumulative averages $\langle T \rangle$ and $\langle wT \rangle$ each differed by less than 0.2% from their values at $\tau/2$. Spatial meshes were deemed converged when increasing the polynomial order of each element by 2 produced a change of less than than 0.5% in the three spatiotemporal averages.

The element meshes used were tensor products, with n_x equal-width elements in the horizontal and n_z elements in the vertical, but unlike the simulations of Chapter 5, the vertical element spacing followed Gauss-Lobatto-Chebyshev points. Element heights thus scale as $1/n_z^2$ near the boundaries and as $1/n_z$ near the center. This helps avoid under-resolving the boundary layers, which would create larger errors than under-resolving the interior. We fixed $n_x/n_z = 2A/3$, based on resolution studies performed with $R = 10^6$ and $\sigma = 1$. The finest mesh used was for the simulation with $R = 2 \cdot 10^{10}$ and $\sigma = 1$, for which $n_z = 96$ with order-6 elements, yielding about 14 points in the top thermal boundary layer and more in the bottom one.

For sufficiently large A , either insulating or periodic side boundaries would suffice for volume averages to approximate those of an infinite domain, but when R is large enough for the flow to be unsteady, periodic domains were found to converge faster as $A \rightarrow \infty$. (For steady flows, however, averages may converge faster on domains with insulating sides because any integer number of convection rolls is possible, while periodic domains require an even number of rolls, which can force the flow farther from its preferred horizontal scale.) We performed several aspect ratio studies, which together suggested that $A = 3$ with periodic sides approximates the infinite domain sufficiently when $R \gtrsim 10^7$ at moderate-to-large σ . For instance, spatiotemporal averages changed by less than 1% when the aspect ratio was

increased from 3 to 9 with $\sigma = 1$ and $R = 10^7$. We found $A = 9$ sufficient at all smaller R , so long as the flow was aperiodic.